# SEA LEVEL RISE AND FLOOD VULNERABILITY OF COASTAL HERITAGE SITES: AN ASSESSMENT OF RAPID METHODS AND MODELLING TECHNIQUES

A THESIS SUBMITTED TO
THE GRADUATE SCHOOL OF NATURAL AND APPLIED SCIENCES
OF
MIDDLE EAST TECHNICAL UNIVERSITY

BY

ARİF ÇAĞATAY UYSAL

IN PARTIAL FULFILLMENT OF THE REQUIREMENTS
FOR
THE DEGREE OF MASTER OF SCIENCE
IN
CIVIL ENGINEERING

DECEMBER 2024

Approval of the thesis:

**SEA LEVEL RISE AND FLOOD VULNERABILITY OF COASTAL HERITAGE SITES: AN ASSESSMENT OF RAPID METHODS AND MODELLING TECHNIQUES**

submitted by **ARİF ÇAĞATAY UYSAL** in partial fulfillment of the requirements for the degree of **Master of Science** i**n Civil Engineering, Middle East Technical University** by,

Prof. Dr. Naci Emre Altun
Dean, **Graduate School of Natural and Applied Sciences** _____

Prof. Dr. Erdem Canbay
Head of the Department, **Civil Engineering** _____

Assist. Prof. Dr. Gülizar Özyurt Tarakcıoğlu
Supervisor, **Civil Engineering, METU** _____

**Examining Committee Members:**

Assoc. Prof. Dr. Elif Oğuz
Civil Engineering, METU _____

Assist. Prof. Dr. Gülizar Özyurt Tarakcıoğlu
Civil Engineering, METU _____

Assist. Prof. Dr. Cüneyt Baykal
Civil Engineering, METU _____

Assist. Prof. Dr. Hasan Gökhan Güler
Civil Engineering, METU _____

Assist. Prof. Dr. Doğan Kısacık
Civil Engineering, İYTE _____

Date: 02.12.2024

**I hereby declare that all information in this document has been obtained and presented in accordance with academic rules and ethical conduct. I also declare that, as required by these rules and conduct, I have fully cited and referenced all material and results that are not original to this work.**

Name Last name : Arif Çağatay Uysal

Signature :

# ABSTRACT

## SEA LEVEL RISE AND FLOOD VULNERABILITY OF COASTAL HERITAGE SITES: AN ASSESSMENT OF RAPID METHODS AND MODELING TECHNIQUES

Uysal, Arif Çağatay
Master of Science, Civil Engineering
Supervisor: Assist. Prof. Dr. Gülizar Özyurt Tarakcıoğlu

December 2024, 146 pages

The past civilizations have settled on the water shores to benefit from its advantages. This is evident from the amount of coastal cultural heritage sites present today. However, these heritage sites are experiencing the impacts of climate change. Sea level rise and extreme weather events increase the risk of flooding, inundation, and erosion. Therefore, it is imperative to promptly evaluate the potential loss of these areas and the associated risks to safeguard the natural values and historical artifacts. The objective of this study is to map the flooded and inundated areas of four coastal heritage sites under various climate change scenarios. The aim is to illustrate and compare different flood analysis and vulnerability assessment methods. Three different techniques are used in the flood mapping. simple and enhanced bathtub models (Williams, 2019), and dynamic numerical modeling. For dynamic numerical modeling, Delft3D (developed by Deltares) is used. The maps are compared to the Coastal Vulnerability Index method (Ozyurt, 2007) which is a desk-based assessment method. The method comparison revealed that with low resolution DEMs, eBTM overestimates the flood extents whereas with high resolution, sBTM and eBTM were compatible with a slight overestimation of sBTM. The flood map obtained by Delft3D was smaller than the bathtub ones prepared with extreme water

level databases. The flood maps and CVI revealed that Teos is the most vulnerable site against the inundation due to sea level rise and Soli-Pompeipolis is the most vulnerable one against the future extreme water levels while Anemurium being the least vulnerable one.

Keywords: Coastal Cultural Heritage Areas, Climate Change, Sea Level Rise, Extreme Water Levels, Flooding

# ÖZ

## KIYI MİRAS ALANLARININ DENİZ SEVİYESİ YÜKSELMESİ VE SU BASKININA KARŞI KIRILGANLIĞI: HIZLI YÖNTEMLER VE MODELLEME TEKNİKLERİNİN DEĞERLENDİRİLMESİ

Uysal, Arif Çağatay
Yüksek Lisans, İnşaat Mühendisliği
Tez Yöneticisi: Dr. Öğr. Üye. Gülizar Özyurt Tarakcıoğlu

Aralık 2024, 146 sayfa

Geçmiş medeniyetler tıpkı bugün de olduğu gibi suyun avantajlarından faydalanmak için su kütlelerinin kıyılarına yerleşmeyi tercih etmişlerdir. Bu durum, dünya genelinde kıyı kültür mirası alanlarının sayısından da anlaşılmaktadır. Ancak bu kıyı mirası alanları da iklim değişikliği ve etkilerinin tehditi altındadır. Deniz seviyesinin yükselmesi, şiddeti ve sıklığı artan ekstrem hava olayları sel, su baskını ve erozyon riskini artırmaktadır. Bu nedenle, hem doğal değerleri hem de tarihi eserleri korumak için bu alanların potansiyel kaybını ve ilgili riskleri hızlı bir şekilde değerlendirmek gerekmektedir. Bu çalışmanın amacı, çeşitli iklim senaryoları altında dört kıyı mirası alanının kalıcı ve geçici olarak sular altında kalan alanlarını haritalamaktır. Hedef, etkilenen alanların kapsamını göstermek ve farklı taşkın analizi ve kırılganlık değerlendirme yöntemlerini karşılaştırmaktır. Taşkın haritalamasında üç farklı teknik kullanılmıştır. Bunlar, statik modeller olan basit ve geliştirilmiş CBS temelli modelleme ve dinamik sayısal modellemedir. Dinamik sayısal modelleme için Deltares tarafından geliştirilern Delft3D kullanılmıştır. Elde edilen taşkın haritaları, gösterge temelli bir kırılganlık değerlendirme yöntemi olan Kıyı Kırılganlık İndeksi (CVI-SLR) (Özyurt, 2007) yöntemi ile de karşılaştırılmıştır. Yöntem karşılaştırması,

düşük çözünürlüklü SYM'lerde eBTM'nin taşkın alanlarını olduğundan fazla tahmin ettiğini, yüksek çözünürlükte ise sBTM'in az miktarda fazla tahmin ettiğini, fakat yine de eBTM ile uyumlu olduğunu ortaya koymuştur. Delft3D ile elde edilen taşkın alanı, ekstrem su seviyesi veri tabanları ile hazırlanan CBS temelli yöntemlere göre daha küçüktür. Taşkın haritaları ve CVI, Teos'un deniz seviyesinin yükselmesine bağlı su baskınlarına karşı en kırılgan bölge olduğunu ve Soli-Pompeipolis'in gelecekteki ekstrem su seviyelerine karşı en kırılgan bölge olduğunu, Anemurium'un ise en az kırılgan bölge olduğunu ortaya koymuştur.

Anahtar Kelimeler: Kıyı Kültürel Miras Alanı, İklim Değişikliği, Deniz Seviyesi Yükselmesi, Ekstrem Su Seviyeleri, Taşkın

*Dedicated to the Ancient Gods of Anatolia…*

## ACKNOWLEDGMENTS

Above all else, I would like to extend my most sincere thanks to Mustafa Kemal Atatürk, who has inspired millions with his vision, leadership and tireless devotion to education and science. His commitment to critical thinking, advancement, and knowledge is the touchstone for both this thesis and my journey as a scholar. Without his visionary reforms, my opportunities to perform the academic studies could not have taken place.

My parents and my sister, thank you from the bottom of my heart for your love, your support, and most of all, your faith in me and my abilities. Their sacrifices and encouragement, as well as their constant presence, have given me the confidence and the determination to challenge myself and chase my goals. This accomplishment belongs as much to them as it does to me. I owe them a deep debt of gratitude for being my most reliable sounding board, constant cheerleader, and steady companion during the ups and downs of this process. They were always aware of how much I can self-sabotage and have made efforts to lift me up. Their belief in me is a reminder of the beauty of family and has allowed me to stay tough through this arduous and teaching journey.

I would like to express my sincere gratitude to my supervisor Dr. Gülizar Özyurt Tarakcıoğlu for her knowledge, guidance, and support throughout this process, not only academically but also with the personal struggles of life. Her insightful feedback, patient mentorship and relentless dedication ultimately shaped this thesis and me as a researcher. I feel truly privileged to have been and will be able to work with her, and her example of dedication motivates me to continue my work.

I am deeply grateful to Prof. Dr. Ayşen Ergin for her invaluable contributions at the very beginning of my academic journey and sparking up my interest in this field at a time of doubt. Her in-depth knowledge, thoughtful advice, dedication to her field, humour, and unique style of human interaction inspired me and provided a continuous learning experience. Her encouragement and key questions enriched the

development of the thesis. I am deeply honored to be her assistant and to have benefited from her guidance and expertise.

I would like to express my sincere thanks to my esteemed professors in our laboratory: Prof. Dr. Ahmet Cevdet Yalçıner, Assist. Dr. Cüneyt Baykal, Assist. Dr. Hasan Gökhan Güler and Dr. Işıkhan Güler. Their knowledge, guidance and feedbacks have been an additional fuel for my graduate course and thesis studies. I would like to extend my heartfelt gratitude to them for consistently making me feel assured of their support whenever I needed it and constantly checking up on me.

I would like to extend my sincere gratitude to Assoc. Dr. Onur Pekcan for his invaluable guidance during challenging moments and for his unwavering support in both material and moral matters. Additionally, I wish to express my heartfelt thanks to the SiteEye team and all the assistants for their contributions to the elevation model shots utilized in this thesis.

I would like to thank my dearest friends Senemhan Yılmaz, Tevfik Özalp, Deniz Narman and Nil Yörük for their endless support and for always being there whenever I needed help. I am deeply grateful for everything they did to help me navigate this challenging process with greater ease. I feel incredibly fortunate to have them in my life.

I would like to thank Iremnaz Kösem, my dear friend and confidante, who has been my companion since the beginning of my undergraduate education, and Elif Ayşe Öztürk Çambal, whom I only regret not being able to meet sooner before the graduate school. Their friendship and support took my graduate education and thesis studies to another level.

I would like to express my sincere gratitude to my friends Furkan Demir, Bilge Karakütük, Barış Ufuk Şentürk, Akdeniz İnce, and Cem Sevindik who have been my company since the very beginning of my master's journey. Their companionship and the enjoyable working environment they fostered amidst the challenges was priceless.

I would like to thank and express my gratitude to Alperen Korkmaz, Ayşenur Gökdağ, and Görkem Kılıç who tried to help me emotionally, psychologically, and materially in my thesis preparation process. Besides their valuable friendship and constant joyful environment they created, they helped me to stay on track all the time. I will always cherish the sacrifices they made to help me, and this work would not have been the same without them.

I would like to thank Nuray Emre, who boosted my mood with her pleasant conversation every time, and Fatoş Şahin, Çiğdem and Haydar Asil, who helped me distract from the intensity of work and kept me fit with their delicious meals.

I would like to also acknowledge the help of Prof. Dr. Mehmet Tekocak (Head of Anemurium Archaeology Team), Prof. Dr. Musa Kadıoğlu (Head of Teos Archaeology Team) and Prof. Dr. Deniz Kaplan (Head of Soli-Pompeipolis Archaeology Team) during the site investigations.

Finally, I would like to thank the BİDEB-2210 National MSc/MA Scholarship Program for their endorsement of my graduate studies. This thesis is also partially funded by TÜBİTAK ARDEB Project 122M613.

## TABLE OF CONTENTS

ABSTRACT ..... v

ÖZ ..... vii

ACKNOWLEDGMENTS ..... x

TABLE OF CONTENTS ..... xiii

LIST OF TABLES ..... xvi

LIST OF FIGURES ..... xviii

LIST OF ABBREVIATIONS ..... xxiv

CHAPTERS

1 INTRODUCTION ..... 1

2 LITERATURE REVIEW ..... 5

2.1 Global Climate Change, Sea Level Rise and Future Extreme Water Levels ..... 5

2.1.1 Global Climate Change ..... 5

2.1.2 Sea Level Rise and Projections ..... 8

2.1.3 Extreme Water Level (EWL) Projections ..... 9

2.2 Flood Mapping ..... 10

2.3 Coastal Vulnerability Assessment - Index-Based Methods ..... 14

2.4 Flood Vulnerability of Coastal Cultural Heritage Sites ..... 15

3 METHODOLOGY ..... 19

3.1 Datasets ..... 19

3.1.1 Türkiye Coastal Heritage Sites Database ..... 19

3.1.2 Rate of Sea Level Rise ..... 21

3.1.3 Extreme Water Levels ..... 21

3.1.4 Topography and Bathymetry ..... 26
3.1.5 Landcover ..... 28
3.1.6 Coastal Slope ..... 29
3.1.7 Tidal Range ..... 29
3.1.8 Engineered Frontage ..... 30
3.1.9 Natural Protection Degradation ..... 30
3.1.10 Coastal Protection Structures ..... 30
3.2 Site Selection ..... 31
3.2.1 Elevation ..... 31
3.2.2 Shoreline Length ..... 32
3.2.3 Predisposition of the Coast to Experience Storms ..... 33
3.2.4 Level of Conservation ..... 34
3.2.5 Status of the Remains ..... 36
3.3 Flood Modeling Methods ..... 37
3.3.1 Simple Bathtub Model (sBTM) ..... 37
3.3.2 Enhanced Bathtub Model (eBTM) ..... 39
3.3.3 Hydrodynamic Model: Delft3D ..... 43
3.4 Vulnerability Assessment by CVI ..... 55
4 RESULTS ..... 59
4.1 Sea Level Rise and Extreme Water Level Projections at Turkish Coasts … ..... 59
4.2 Study Sites ..... 63
4.3 CVI-SLR Analyses ..... 68
4.4 Flood Maps ..... 69

4.4.1 Ancient City of Aleksandria Troas ..... 70
4.4.2 Ancient City of Anemurium ..... 75
4.4.3 Ancient City of Soli-Pompeipolis ..... 88
4.4.4 Ancient City of Teos ..... 98
5 DISCUSSION ..... 123
5.1 Aleksandria Troas ..... 123
5.2 Anemurium ..... 124
5.3 Soli-Pompeipolis ..... 125
5.4 Teos ..... 126
5.5 sBTM vs eBTM ..... 128
5.6 Bathtub Models vs Delft3D ..... 129
5.7 CVI ..... 129
5.8 Limitations ..... 130
6 CONCLUSION ..... 133
REFERENCES ..... 141

## LIST OF TABLES

TABLES

Table 3.1 Number of Coastal Heritage Sites According to the Criteria and Heritage (Kösem et al., 2023) ..... 21
Table 3.2 Significant Wave Height of Corresponding Return Periods ..... 45
Table 3.3 CVI Parameters of Inundation and Storm Surge Impacts (Özyurt, 2007) ..... 57
Table 3.4 Class Ranges of the Parameters Affecting Inundation and Storm Surge Flood Impacts (Özyurt, 2007) ..... 57
Table 4.1 Extreme Water Level Ranges at Turkish Coasts for 2050 ..... 59
Table 4.2 Extreme Water Level Ranges at Turkish Coasts for 2100 ..... 59
Table 4.3 CVI-SLR Input Parameters for Flooding and Surge Impacts (Blue: Actual value of the parameter, Red: CVI Class of that value) ..... 68
Table 4.4 CVI-SLR Results (Vulnerability Indices out of 5) ..... 69
Table 4.5 Inundated and Flooded sBTM Areas of the Ancient City of Aleksandria Troas ($m^2$) ..... 71
Table 4.6 Inundated and Flooded eBTM Areas of the Ancient City of Aleksandria Troas ($m^2$) ..... 73
Table 4.7 Inundated and Flooded sBTM areas of Anemurium using GLO-30 ..... 76
Table 4.8 Inundated and Flooded sBTM Areas of Anemurium using UAV DSM ..... 78
Table 4.9 Inundated and Flooded eBTM Areas of Anemurium using GLO-30 ..... 82
Table 4.10 Inundated and Flooded eBTM Areas of Anemurium using UAV-DSM ..... 84
Table 4.11 Inundated and Flooded sBTM Areas of the Ancient City of Soli-Pompeipolis using GLO-30 ($m^2$) ..... 88
Table 4.12 Inundated and Flooded sBTM Areas of the Ancient City of Soli-Pompeipolis using UAV DSM ($m^2$) ..... 91
Table 4.13 Inundated and Flooded eBTM Areas of the Ancient City of Soli-Pompeipolis using GLO-30 ($m^2$) ..... 94

Table 4.14 Inundated and Flooded eBTM Areas of the Ancient City of Soli-Pompeipolis using UAV DSM ($m^2$) ..... 96
Table 4.15 Inundated and Flooded sBTM Areas of the Ancient City of Teos using GLO-30 ($m^2$) ..... 98
Table 4.16 Inundated and Flooded sBTM Areas of the Ancient City of Teos using SYM-5 ($m^2$) ..... 101
Table 4.17 Inundated and Flooded sBTM Areas of the Ancient City of Teos using UAV-DSM ($m^2$) ..... 105
Table 4.18 Inundated and Flooded sBTM Areas of the Ancient City of Teos using UAV DTM ($m^2$) ..... 107
Table 4.19 Inundated and Flooded eBTM Areas of the Ancient City of Teos using GLO-30 (m2) ..... 109
Table 4.20 Inundated and Flooded eBTM Areas of the Ancient City of Teos using SYM-5 ($m^2$) ..... 111
Table 4.21 Inundated and Flooded eBTM Areas of the Ancient City of Teos using UAV-DSM ($m^2$) ..... 115
Table 4.22 Inundated and Flooded eBTM Areas of the Ancient City of Teos using UAV-DTM ($m^2$) ..... 119
Table 6.1 The Inundated and Flooded areas of Aleksandria Troas for different scenarios, databases, and years (Areas in $m^2$ and as percentages of the heritage site) ..... 134
Table 6.2 Inundated and Flooded areas of Soli Pompeipolis for different scenarios, databases, and years ..... 135
Table 6.3 Inundated and Flooded areas of Anemurium for different scenarios, databases and years ..... 136
Table 6.4 Inundated and Flooded areas of Teos for different scenarios, databases and years ..... 137

## LIST OF FIGURES

FIGURES

Figure 2.1. Concentration of Three Main Greenhouse Gases Since 1850 (Retrieved from IPCC AR6 Synthesis Report 2023) (IPCC, 2023) ..... 6
Figure 2.2. Observed Global Surface Temperature (Retrieved from IPCC AR6 Synthesis Report 2023) (IPCC, 2023) ..... 6
Figure 2.3 Description of SSP's (IPCC, 2023) ..... 7
Figure 2.4 Global Mean Sea Level Change in centimeters (IPCC, 2023) ..... 8
Figure 2.5 Bathtub approach to flooding (Seenath et al., 2016) ..... 11
Figure 2.6 The Predicted Shoreline of Motya Island for 2100 under RCP8.5 Emission Scenario (Ravanelli et al., 2019) ..... 16
Figure 2.7 Projected Shorelines of Pyrgi for 2100 under different scenarios (Anzidei et al., 2020) ..... 17
Figure 3.1 LISCOAST EWL Data Points Along Turkish Coasts ..... 23
Figure 3.2. Kirezci et al. (2020) EWL Data Points Along Turkish Coasts ..... 25
Figure 3.3 Copernicus GLO-30 DEM data for Ancient City of Knidos, Datça, Muğla ..... 26
Figure 3.4. The 3D SiteEye model of the Ancient City of Teos ..... 27
Figure 3.5 Land Cover Types of Antalya Province (EEA, 2020) ..... 28
Figure 3.6. Satellite view and Coastal Formation of the Ancient City of Knidos, Datça, Türkiye (Google Earth, 2024) ..... 32
Figure 3.7. Anemurium and Adrasan Heritage Sites with Different Shoreline Lengths (Red lines representing heritage site borders) (Google Earth, 2024) ..... 33
Figure 3.8. Two Coastal Heritage Sites with Different Storm Predispositions (Google Earth, 2024) ..... 34
Figure 3.9. Two Archaeological Sites with Different Degrees of Conservation (A: Ancient City of Phaselis, B: Ancient City of Kyme) (Red lines representing heritage site borders) (Google Earth, 2024) ..... 35

Figure 3.10. Totally unearthed and earthed heritage sites ( A: Ancient City of Colorna, B: Ancient City of Anemurium) (Red lines representing heritage site borders) (Google Earth, 2024) ..... 37
Figure 3.11. Land Cover of the Ancient City of Aleksandria Troas retrieved from Copernicus Coastal Zone Land Cover (2021) ..... 40
Figure 3.12. Land Cover of the Ancient City of Teos retrieved from Copernicus Coastal Zone Land Cover (2021)..... 41
Figure 3.13. Land Cover of the Ancient City of Anemurium retrieved from Copernicus Coastal Zone Land Cover (2021) ..... 41
Figure 3.14. Land Cover of the Ancient City of Soli-Pompeipolis retrieved from Copernicus Coastal Zone Cover (2021)..... 42
Figure 3.15 ERA5 Data Points of Hourly Data on Single Levels Database Near Teos..... 44
Figure 3.16 Annual Maxima Significant Wave Heights between 1984-2023 for Teos..... 44
Figure 3.17 Deep-water Wavelength vs Significant Wave Height Graph for the past 40-year data..... 45
Figure 3.18 Wave Time Series of the January 6th, 2012 storm..... 46
Figure 3.19 Wind Speed Time Series of January 6th, 2012 storm ..... 47
Figure 3.20 The Maximum Storms of Every Year with hours of maximum hourly significant wave height aligned ..... 48
Figure 3.21 Time Series of Wave Height and Period of the Synthetic Storm..... 49
Figure 3.22 Wind Time Series obtained from the Synthetic Triangular Wave Time Series..... 50
Figure 3.23 Computational Domain of Wave Module (Google Earth, 2024) ..... 51
Figure 3.24 Computational meshes of Flow Module (Google Earth, 2024) ..... 53
Figure 3.25 ERA5 Data Point for Water and Surge Level (Google Earth, 2024) .. 54
Figure 3.26 Water level increase during January 6th ,2012 storm ..... 54
Figure 3.27 Vulnerability Classification based on CVI(SLR) (Özyurt, 2007)..... 55
Figure 3.28 The CVI (SLR) Vulnerability Matrix (Özyurt, 2007)..... 56

Figure 4.1 EWL (m) ranges for Turkish Coasts ..... 60
Figure 4.2 EWL Prediction Points and Classifications for 2050 from Kirezci ..... 61
Figure 4.3 EWL Prediction Points and Classifications for 2100 from Kirezci ..... 61
Figure 4.4 EWL Prediction Points and Classifications for 2050 from LISCOAST 62
Figure 4.5 EWL Prediction Points and Classifications for 2100 from LISCOAST 63
Figure 4.6 The Ancient City of Aleksandria Troas (A: The heritage site borders, B: Ancient Harbour Ruins, C: The Preserved Pink Lake behind the ancient harbour) (Google Earth, 2024) ..... 64
Figure 4.7 The Ancient City of Teos (A: The heritage site borders and Sığacık, B: The Ancient Breakwater of the South Harbor, C: A Photo from the Breakwater of the South Harbor) (Google Earth, 2024) ..... 65
Figure 4.8 The Ancient City of Anemurium (Google Earth, 2024) ..... 66
Figure 4.9 The Ancient City of Soli-Pompeipolis (A: Remains of the west breakwater, B: Heritage Site Borders, C: Excavations of the breakwater) (Google Earth, 2024) ..... 67
Figure 4.10 Map of the Ancient Harbour and Breakwaters of Soli-Pompeipolis (Great Britain Hydrographic Office, 1885). ..... 67
Figure 4.11 Aleksandria Troas sBTM Inundation and Flood Maps using GLO-30 (A: Inundation in 2100, B: Storm Surge Flooding in 2050, C: Storm Surge Flooding in 2100) ..... 72
Figure 4.12 Aleksandria Troas eBTM Inundation and Flood Maps using UAV DSM (A: Inundation in 2100, B: Storm Surge Flooding in 2050, C: Storm Surge Flooding in 2100) ..... 74
Figure 4.13 Anemurium sBTM Inundation and Flood Maps using GLO-30 (A: Inundation in 2100, B: Storm Surge Flooding in 2050, C: Storm Surge Flooding in 2100) ..... 77
Figure 4.14 Anemurium sBTM Inundation Map using UAV DSM (A: Result near the ruin on the beach, B: Result on the eastern part, C: The whole shoreline, D: Results near the coastal ruins) ..... 79

Figure 4.15 Anemurium sBTM Storm Surge Flood Map for 2050 using UAV DSM (A: The whole shoreline focusing on the portion with ruins, B: Result on the eastern part)..... 80
Figure 4.16 Anemurium sBTM Storm Surge Flood Map for 2100 using UAV DSM (A: The whole shoreline focusing on the portion with ruins, B: Result on the eastern part)..... 81
Figure 4.17 Anemurium eBTM Inundation and Flood Maps using GLO-30 (A: Inundation in 2100, B: Storm Surge Flooding in 2050, C: Storm Surge Flooding in 2100) ..... 83
Figure 4.18 Anemurium eBTM Inundation Map for 2100 using UAV DSM (A: Beach Portion with Ruins, B:Eastern Side of the city, C: Situation around the coastal ruin)..... 85
Figure 4.19 Anemurium eBTM Storm Surge Flood Map for 2050 using UAV DSM (A: The beach with ruins, B: Focusing on the building ruin) ..... 86
Figure 4.20 Anemurium eBTM Storm Surge Flood Map for 2100 using UAV DSM (A: The beach with ruins, B: Focusing on the building ruin) ..... 87
Figure 4.21 Soli-Pompeipolis sBTM Inundation and Flood Maps using GLO-30 (A: Inundation in 2100, B: Storm Surge Flooding in 2050, C: Storm Surge Flooding in 2100)..... 90
Figure 4.22 Soli-Pompeipolis sBTM Inundation and Flood Maps using UAV DSM (A: Inundation in 2100, B: Storm Surge Flooding in 2050, C: Storm Surge Flooding in 2100)..... 92
Figure 4.23 Soli-Pompeipolis eBTM Inundation and Flood Maps using GLO-30 (A: Inundation in 2100, B: Storm Surge Flooding in 2050, C: Storm Surge Flooding in 2100)..... 95
Figure 4.24 Soli-Pompeipolis eBTM Inundation and Flood Maps using UAV DSM (A: Inundation in 2100, B: Storm Surge Flooding in 2050, C: Storm Surge Flooding in 2100)..... 97
Figure 4.25 Teos sBTM Inundation and Flood Maps using GLO-30 (A: Inundation in 2100, B: Storm Surge Flooding in 2050, C: Storm Surge Flooding in 2100) .... 99

Figure 4.26 Teos sBTM Inundation Maps using SYM-5 (A: Inundation from the Teos Marina (Ancient North Harbour), B: Inundation at the South Ancient Harbour) ..... 102
Figure 4.27 Teos sBTM Flooding Maps for 2050 using SYM-5 (A: Flooding from the Teos Marina (Ancient North Harbour), B: Flooding at the South Ancient Harbour) ..... 103
Figure 4.28 Teos sBTM Flooding Maps for 2100 using SYM-5 (A: Flooding from the Teos Marina (Ancient North Harbour), B: Flooding at the South Ancient Harbour) ..... 104
Figure 4.29 Teos sBTM Inundation and Flood Maps using UAV DSM (A: Inundation in 2100, B: Storm Surge Flooding in 2050, C: Storm Surge Flooding in 2100) ..... 106
Figure 4.30 Teos sBTM Inundation and Flood Maps using UAV DTM (A: Inundation in 2100, B: Storm Surge Flooding in 2050, C: Storm Surge Flooding in 2100) ..... 108
Figure 4.31Teos eBTM Inundation and Flood Maps using GLO-30 (A: Inundation in 2100, B: Storm Surge Flooding in 2050, C: Storm Surge Flooding in 2100) ... 110
Figure 4.32 Teos eBTM Inundation Maps for 2100 using SYM-5 (A: Flooding from the Teos Marina (Ancient North Harbour), B: Flooding at the South Ancient Harbour) ..... 112
Figure 4.33 Teos eBTM Flooding Maps for 2050 using SYM-5 (A: Flooding from the Teos Marina (Ancient North Harbour), B: Flooding at the South Ancient Harbour) ..... 113
Figure 4.34 Teos eBTM Flooding Maps for 2100 using SYM-5 (A: Flooding from the Teos Marina (Ancient North Harbour), B: Flooding at the South Ancient Harbour) ..... 114
Figure 4.35 Teos eBTM Inundation Map for 2100 using UAV-DSM ..... 116
Figure 4.36 Teos eBTM Inundation Maps for 2050 using UAV-DSM (A: Kirezci Predictions, B: LISCOAST Predictions) ..... 117
Figure 4.37 Teos eBTM Flooding Map for 2100 using UAV-DSM ..... 118

Figure 4.38 Teos eBTM Inundation and Flood Maps using UAV DTM (A: Inundation in 2100, B: Storm Surge Flooding in 2050, C: Storm Surge Flooding in 2100) ..... 120
Figure 4.39 The Flood Map of January 6th, 2012 Storm with present Shoreline and 2100 shoreline under SSP5 SLR Projections (Light Blue: Under present shoreline, Dark Blue: Under 2100 shoreline) ..... 121
Figure 4.40 The Flood Map given by Delft3D Run for 100 RP synthetic storm with SLR scenario ..... 122

## LIST OF ABBREVIATIONS

ABBREVIATIONS

DEM: Digital Elevation Model

DSM: Digital Surface Model

DTM: Digital Terrain Model

eBTM: Enhanced Bathtub Model

EWL: Extreme Water Level

GCM: Global Climate Model

LISCOAST: Large Scale Integrated Sea-Level and Coastal Assessment Tool

RCP: Representative Concentration Pathway

RP: Return Period

RSLR: Rate of Sea Level Rise

sBTM: Simple Bathtub Model

SLR: Sea Level Rise

SSP: Shared Socio-economic Pathway

UAV: Unmanned Aerial Vehicle

# CHAPTER 1

# INTRODUCTION

Great civilizations throughout history have often flourished near bodies of water, like rivers, seas, and oceans. The economic, logistical, and strategic benefits of water sources have been crucial in this development. Fortunately, evidence of this can be found in the numerous heritage sites along the world's coastlines or in the highly developed coastal cities today. Ongoing archaeological studies at these sites have provided valuable insights into the past's social, material, and cultural aspects. These findings contribute to archaeology, history, and other scientific disciplines while offering tourism opportunities in the host countries. Unfortunately, these valuable heritage sites are facing imminent risk due to the impacts of climate change.

A change in Earth's climate is not unusual and has happened numerous times before. With the climate, the flora and fauna and the total face of the planet have changed multiple times in the long past of Earth. However, the current pace of climate change is believed to be highly affected by human actions (Calvin et al., 2023). The skyrocketed number of industrial developments, deforestation, mining, and industrialized animal husbandry accelerated the change the earth faces by causing a jump in the amount of certain gases in the atmosphere. These gases, mainly carbon dioxide ($CO_2$) and methane ($CH_4$), trap the solar radiation in the atmosphere, causing an overall global temperature increase. This is described as the greenhouse effect, which is also the reason behind the term “Greenhouse gases.” After the Industrial Revolution, where the use of non-renewable energy, mass production, and the expansion in the fields where fossil fuels are used, the emission of greenhouse gases reached unprecedented levels, which further accelerated climate change.

Providing very little time for the inhabitants to adapt, this fast climate change brings up threats and problems in almost every aspect of modern human life. For instance,

the distribution of vector-borne diseases also shifted with changing climate, creating new threats to human health. (Haines et al., 2006), or productivity in agriculture, which decreases due to increasing temperature offsets that lead to stronger evapotranspiration, infestations, and shorter crop durations. (Malhi et al., 2021)

Among these global impacts of climate change, this study aims at the one that will most directly and severely affect coastal heritage areas: sea level rise. The rise of the global sea level is a result of global warming and thermal expansion. The natural and historical values of heritage sites are under the threat of inundation and erosion due to sea level rise and extreme weather conditions, as climate change causes an increase in the severity and number of extreme weathers.

Recognizing coastal heritage areas' significance, assessing coastal values and conducting vulnerability analyses as part of an effective strategy should be integral to a country's emergent plans. This approach will aid in identifying areas of heritage that require adaptation or protection strategies. Türkiye, having 1250 cultural and 1266 natural coastal heritage sites, should be one of the first countries to do so. Knowing the extent of the future risk will be a guide to formulating these strategies. In the literature, there are different ways to indicate this risk of flooding of a heritage site. Indicator-based methods, GIS-based flood mapping, and hydrodynamic modelling are all widely used methods. The comparison of these methods, each with different advantages, and how sensitive they are to which inputs is the focus of this study. Also, how the resolution of the elevation model affects the consistency between this method is a question of interest of the thesis as well. Therefore, flood maps generated using GIS-based approaches and hydrodynamic model (Delft3d) are compared to the outputs of CVI-SLR (Özyurt, 2007), a fast indicator-based method to assess the sea level rise vulnerability, to present future flood extents, and to evaluate the compatibility of fast desk-based methods.

Chapter 2 is the literature review chapter. This section provides information about the work that has been done on the key aspects of this study, including research on

climate change, sea level rise, cultural heritage interaction and vulnerability, and flood and inundation mapping, and illustrates the gaps that motivated this study.

In Chapter 3, the methodology is explained. Since the study aims to capture as much case as possible, the number of datasets used are high and thus, this chapter starts with a dataset introduction part. After giving information about the datasets and in which part of this study they were used, the chapter continues along to the site selection part where the decision-making process behind the selection of study sites is explained. Then finally, the flood mapping methods and the vulnerability analysis method used for the study sites are presented.

In Chapter 4, the selected sites, maps and areal results of inundation and flooding are presented. Besides these, which are the main results of this study, the investigation of the extreme water level prediction datasets along the Turkish coasts are discussed. The results are given separately for each study site, each method and each elevation model that is used.

Chapter 5 is the conclusions. The outcomes of the study are summarized in this chapter and the comments and remarks for future studies are suggested.

# CHAPTER 2

# LITERATURE REVIEW

## 2.1 Global Climate Change, Sea Level Rise and Future Extreme Water Levels

### 2.1.1 Global Climate Change

Climate change is an ongoing gradual shift in the overall climate conditions of the Earth, driven by numerous factors. (Weber, 2010) The effect of this shift is sensible not only in the atmospheric phenomena but in every field and aspect of human life.

According to the Sixth Assessment Report of the Intergovernmental Panel on Climate Change (IPCC, 2023), human-induced greenhouse gases are the main driver for the observed climate change. The emission of greenhouse gases, mainly $CO_2$ and $CH_4$ (methane), has risen due to the excessive consumption of unsustainable energy, industrial production rates, and $CO_2$-emitting land use. Figure 2.1 shows the increase in the concentration of the three main greenhouse gases. The report states with high confidence that Earth's atmosphere had the highest $CO_2$ concentration in 2019 since the past 2 million years.

This increase in greenhouse gases is the main driver of the rise in surface temperatures. Greenhouse gases in the atmosphere are responsible for capturing solar radiation after it reflects from the globe's surface; re-emitting this absorbed radiation results in an overall rise in temperatures. This is known as the so-called greenhouse effect. This increase eventually results in a great loss of the ice mass of the globe, which causes global sea level rise.

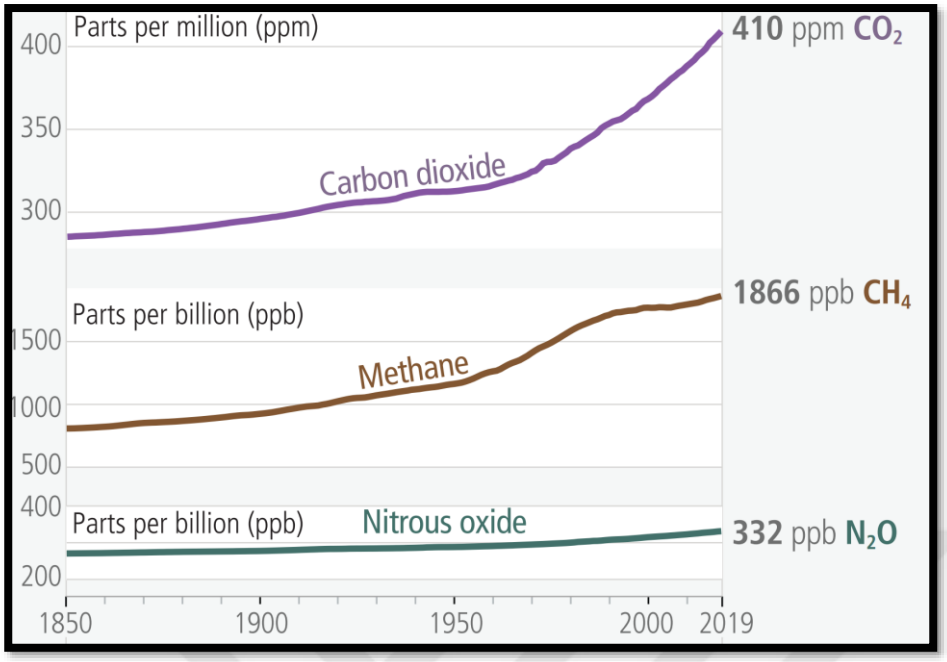



Figure 2.1. Concentration of Three Main Greenhouse Gases Since 1850 (Retrieved from IPCC AR6 Synthesis Report 2023) (IPCC, 2023)

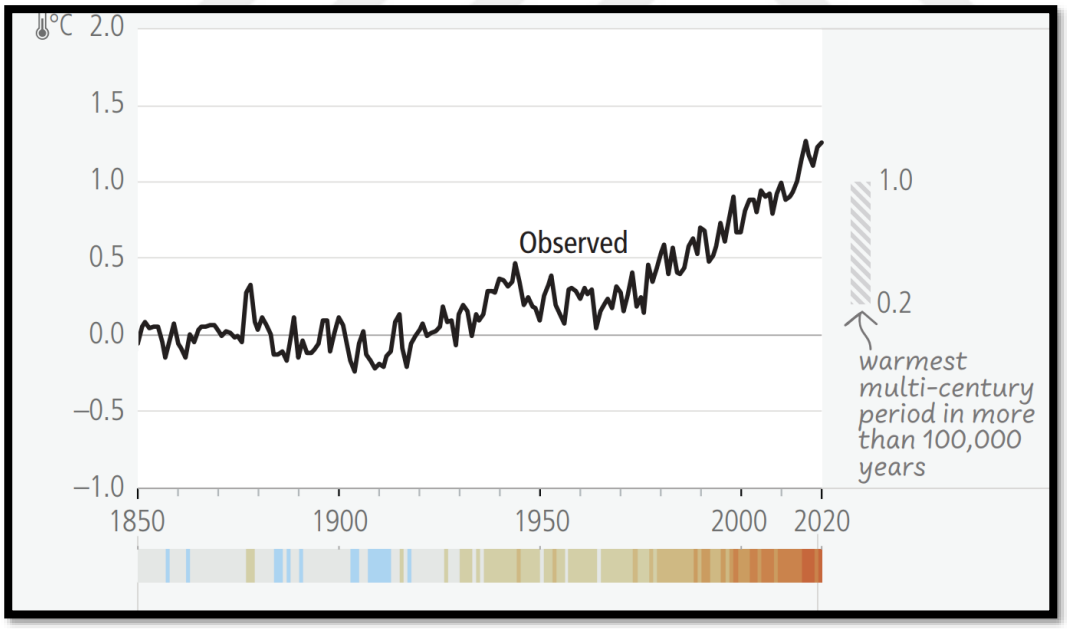



Figure 2.2. Observed Global Surface Temperature (Retrieved from IPCC AR6 Synthesis Report 2023) (IPCC, 2023)

According to Figure 2.2, the global surface temperature has risen by almost 1.5°C in the past 100 years. Humanity, the primary driver of the acceleration of global warming, will have a significant impact on how climate change develops in the future. Based on the actions that humanity must take, IPCC working groups have developed various emission scenarios.

In AR6 (IPCC, 2023), five representative scenarios are used to evaluate the global climate reaction. These scenarios are based on the potential future anthropogenic drivers, named the Shared Socio-economic Pathways (SSP) (IPCC, 2023).

- **SSP3-7.5 and SSP5-8.5:** High and very high GHG emission scenarios where the concentrations are predicted to be almost doubled by 2050 and 2100.
- **SSP2-4.5:** Intermediate scenario where the emission rates are not changing until the middle of this century.
- **SSP1-1.9 and SSP1-2.6:** Low and very low emission scenarios where the point of no emission is reached around 2050-2070.

| Category description | GHG emissions scenarios (SSPx-y*) in WGI & WGII |
|---|---|
| limit warming to 1.5°C (>50%) with no or limited overshoot*** | Very low (SSP1-1.9) |
| return warming to 1.5°C (>50%) after a high overshoot*** | |
| limit warming to 2°C (>67%) | Low (SSP1-2.6) |
| limit warming to 2°C (>50%) | |
| limit warming to 2.5°C (>50%) | |
| limit warming to 3°C (>50%) | Intermediate (SSP2-4.5) |
| limit warming to 4°C (>50%) | High (SSP3-7.0) |
| exceed warming of 4°C (>50%) | Very high (SSP5-8.5) |

Figure 2.3 Description of SSP's (IPCC, 2023)

Figure 2.3 shows the description and predicted rise in the global temperatures for the illustrated five scenarios. As this rise continues to bring significant and inevitable

consequences, the areas to be affected the most are predicted to be polar, mountain and coastal ecosystems.

### 2.1.2 Sea Level Rise and Projections

The major threat to the coastal ecosystems is the rising sea levels, due to the loss of glacier mass of the earth and thermal expansion. According to the AR6 Report by IPCC (2023), the average rate of sea level rise (SLR) has been increasing since the beginning of the 20$^{th}$ century, reaching 1.3 mm/year by 1976, 1.9 mm/year by 2006, and 3.7 mm/year by 2018. This indicates that the average rate of rise has almost tripled in the past 50 years when human influence became the main driver of global warming. Increasing observations suggest that this sea level rise will likely continue in the future (IPCC, 2023). Since SLR is directly linked to how much atmospheric temperature rises, different emission scenarios result in different levels of SLR projections (Figure 2.4) (IPCC, 2023).

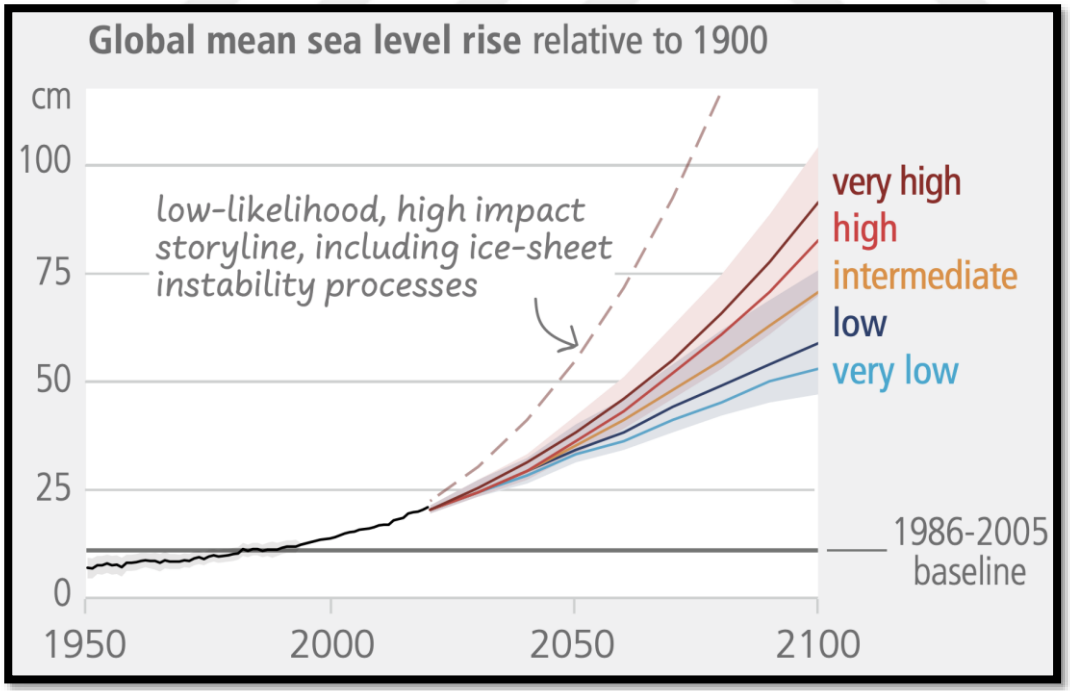



Figure 2.4 Global Mean Sea Level Change in centimeters (IPCC, 2023)

Predicting the global and local sea level rise these emission scenarios will lead to in the coming century is a widely studied topic. The processes underlying sea level rise are better understood as a result of these investigations with new scientific and analytic tools (Garner et al., 2018). The relationship between the global temperature rise and the sea level rise having been analyzed with basic statistical models set the foundations for these projections (Gornitz et al., 1982) In most SLR projection databases, a probabilistic approach has been used where lower, central, and upper estimates are provided. However, some databases give a single SLR projection value.

A widely used projection database is the Sea Level Projection tool of NASA which employs the analysis of the AR6 of IPCC. This database covers the uncertainties that stem from thermal expansion, ocean dynamics, glacier and ice sheet loss.

### 2.1.3 Extreme Water Level (EWL) Projections

In AR6, it is stated that the effects of extreme weather conditions on civil life have further increased since AR5. Compound extreme events have become more frequent since the 1950s due to high human influence on the climate (IPCC, 2023). When compounded with the SLR, the intensified climate extremes will increase the extreme water levels (EWL) and add to the risk of flooding (Wahl et al., 2017).

Extreme weather events taking place during the high tides create EWLs. Predicting these levels for the future when also climate induced SLR adds to the water levels is essential for comprehending and reducing the effects of future coastal flooding. According to Kirezci et al. (2020), the future extreme water levels consist 63% of surge and tide heights, 32% of SLR, and 5% of wave setups. EWLs have been projected using a variety of approaches in the studies that consider tidal fluctuations, surges, and SLR on both global and regional scales. (Lewis et al., 2011)

For example, Kirezci et al. (2020) used tide gauge data to validate and to find out 100-year RP extreme water levels with statistical methods. In the article, one of the key findings was that 100-year RP events are predicted to occur every 10 years in

majority of the 9866 coastal points they used. They provide a global dataset for the 21st century on these points under RCP4.5 and RCP8.5 emission scenarios. Tebaldi et al., (2021) generated sea level rise rates using global climate models (GCM) under 1.5℃, 2℃, 3℃, 4℃ and 5℃ global warming conditions to predict future EWLs at 7283 locations. Their results show that in at least half of these locations, 100-year RP events will take place annually. In another attempt to obtain the change of the EWLs in the 21st century by Vousdoukas et al. (2018), the global coastline is divided approximately into 5000 pieces and 6 member-ensemble CMIP5 GCMs were used to obtain future climate extremes. In this study, the regional distributions of EWL components were considered as probability density functions to provide a probabilistic approach for every 10 years throughout the 21st century. It is predicted that, at the end of this century, the world will experience 34-76 cm higher 100-year RP EWLs under RCP4.5 and 58-172 cm higher EWLs under RCP8.5.

## 2.2 Flood Mapping

The practice of mapping floods is essential for helping communities and governments prepare for hazards associated with flooding. GIS-based rapid flood inundation techniques, compound flooding assessments that combine hydrodynamic modeling and statistical analysis, and real-time flood hazard assessments using hydrogeomorphic classifiers are some of the novel approaches that researchers have investigated to improve the accuracy and efficacy of coastal flood modeling (Muñoz et al., 2020). These methods help to better understand the mechanics underlying coastal flooding in addition to offering crucial insights for initiatives involving coastal adaptation and management. Employing the suggestion by Flick et al., (2012), the term flooding is used for the temporary wetting of dry land which is episodic or periodic and due to the surges of strong storms and tides, and the term inundation is used for the permanent submergence of an area under water due to climate change-induced sea level rise.

- **Bathtub/Planar/Static Models**

The popular bathtub approach divides potentially inundated and dry areas with a deterministic line using only the elevation data of the terrain. It assumes that any land below a certain elevation will be inundated. It allows for rapid flood mapping using Geographic Information Systems (GIS) (Poulter & Halpin, 2008).

The bathtub models tend to overestimate flood areas as they don't take into account certain interactions and hydrodynamics, such as bed friction, flow direction, and topographic and structural barriers (Figure 2.5) (Seenath et al., 2016).

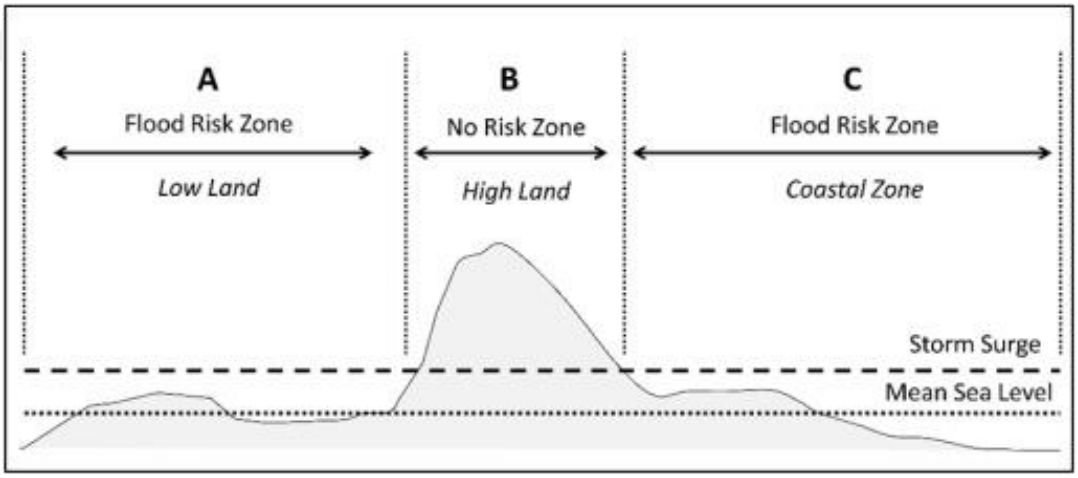



Figure 2.5 Bathtub approach to flooding (Seenath et al., 2016)

A digital elevation model (DEM) is typically the sole data needed for this procedure, however, the DEM having built-in flaws might affect the accuracy mapping. (Leon et al., 2014). For these models to accurately estimate the extent of floods, high-resolution and exact digital elevation models (DEMs) are necessary to capture the topographic features of floodplains (Shastry & Durand, 2019).

Although generally, bathtub static models use only the elevation data, some studies improved a simple bathtub model. For instance, Carneiro-Barros et al. (2023) modified the static bathtub model and created a model that calculates run-up height with empirical formulas, and considers the slope of the terrain. Williams (2019) incorporated the roughness and the slope of the terrain to capture more realistic water

pathways and created the Enhanced Bathtub Model. Another modified static bathtub model is created by Kasmalkar et al. (2024), where the inherent hydraulic connectivity problem of the simple bathtub model is eliminated and a reduction in the water depth is applied to account for the friction as the water moves inland.

Although numerous modifications by the researchers have improved the simple bathtub model, the lack of dynamic processes remains a problem in all of them. The exclusion of components like tidal non-linearity and short-term climate variability might give rise to the need for a dynamic model. In a study made for California coasts, Barnard et al. (2019), assesses a dynamic flood model for coastal impacts of climate change and concludes that the dynamic model predicts three times more population exposure than the static SLR models. This shows the need to consider hydrodynamic flood models due to their ability to incorporate various dynamics.

- **Hydrodynamic Flood Modeling**

Coastal hydrodynamic flood modeling is a specialized approach used to simulate and forecast flooding occurrences along coasts by integrating complex hydraulic equations and principles to mimic the movement of water during flood events. This type of modeling is necessary to comprehend the complex connections among human, hydrological, climatic, and marine systems that cause coastal flooding. Two-dimensional (2D) hydrodynamic models are frequently used to simulate coastal hydrodynamic floods. These models forecast coastal inundation and floods in a spatially and temporally fluctuating fashion by simulating overland flow, which includes storm surges, tidal effects, and wave action (Jafarzadegan et al., 2022).

An example model is LISFLOOD-FP (Bates et al., 2005), which is considered a suitable dynamic model for SLR analysis. It includes momentum and mass conservation equations while calculating the flow transfer between the cells. They conclude in this study that by correctly simulating the dominant coastal processes, this dynamic model surpasses the simple GIS-based flood models.

Another study by Yin et al., (2016) proposes a high-resolution modeling framework that encompasses combined ADCIRC storm surge and FloodMap 2D hydrodynamic modeling to enhance coastal inundation modeling. Using data from Hurricane Sandy to validate their integration, their coupled model was much more accurate than ADCIRC alone, agreeing more with observed flood extents and depths.

Another widely used hydrodynamic model is Delft3D by Deltares. With its various modules, Delft3D is capable of modeling and coupling complex dynamics. For instance, in a study made for the coasts of Bangladesh, Delft3D was used to simulate the effect of climate change-induced sea level rise on the surge inundations (Jisan et al., 2018). Adjusting the baseline under RPC4.5 scenario for 2050 and 2100, Jisan et al., (2018) tries to predict the future surge extents using two historical cyclones.

As exemplified above, there are numerous flood modeling methods. Which type of inundation/flood mapping method is more accurate and time-efficient is a topic of interest among the researchers. Kumbier et al. (2019) made this comparison for estuarine system flooding. Static models can be highly accurate, but they typically require the use of many simplified assumptions; dynamic models capture the temporal and spatial variability of water movement. Kumbier et al. (2019) discovered that static models overestimate flood extents owing to the extra parameters that these models could not account for (e.g., bottom friction and propagation of floodwaters). Dynamic (hydrodynamic) models, although expensive to generate, provide a better approximation of flooding, especially in urban coastal areas where the built environment and land use modify flooding significantly.

In a case study made for Southwest Tobago, Seenath et al., (2016) compared ArcGIS, TELEMAC-2D, and LISFLOOD-FP for a coastal vulnerability assessment. According to the study, “bathtub” (GIS-based) methods, although useful for quick and generalized flood analysis, tended to magnify flood extents because they did not consider flow dynamics, hydraulic connectivity, and physical barriers. TELEMAC-2D exhibited the highest accuracy of the tools; however, LISFLOOD-FP showed a faster performance without losing much in precision. The GIS application as a

screening tool proved effective in focusing attention on flood-vulnerable areas. In the article, they conclude that hydrodynamic models should be stressed to pinpoint areas more accurately for in-depth coastal flood vulnerability assessments, especially in smaller areas or in areas that are at particular risk, with GIS methods performing much better as a tool for large-scale or more general assessments.

## 2.3 Coastal Vulnerability Assessment - Index-Based Methods

Other than visualizing the flood hazard with a flood map, the vulnerability of a coastal area can be expressed with a vulnerability assessment. These assessments simplify the features of a coastal area and turn the complex dynamics into quantifiable indices.

The common methodology presented by IPCC (1991) can be considered the initiative step for vulnerability assessment studies where the impacts of sea level rise like land at loss, wetland at loss, and people at risk have been identified. Since then, numerous vulnerability assessment methods have been improved by the researchers against different coastal hazards.

One example of such a methodology is the Dynamic Interactive Vulnerability Assessment (DIVA) developed as a part of DINAS-COAST project. Integrating physical characteristics like tidal range and geomorphology with the socio-economic status of 12148 segments of the global coastline, this tool guides stakeholders and authorities to identify risks against climate change and sea level rise (Hinkel & Klein, 2006). The coastal vulnerability index (CVI) is one of the leading tools used to assess vulnerability against sea level rise. CVI creates a relative ranking approach by using the geomorphology, elevation and wave climate information (Gornitz, 1991). Having been used for the baseline for various vulnerability methodologies, this method is globally recognized.

Özyurt (2007) presents a coastal vulnerability matrix integrating human influence parameters and physical parameters to obtain a coastal vulnerability index to sea

level rise (CVI-SLR). The fast assessment of the risk level of the coast allows decision-makers to compare sections of coastlines and rank them accordingly. With the parameter-based index results, the method also shows the driving parameter that boosts the vulnerability.

## 2.4 Flood Vulnerability of Coastal Cultural Heritage Sites

Sea level rise and changes in climate parameters like temperature and precipitation will have an impact on cultural heritages situated along the coasts. According to (ICOMOS, 2019; Sesena et al., 2021), sea level rise might cause the loss of access to the heritage site or even total submersion by the seawater, the beginning of wave and saltwater interaction with cultural heritage assets, deterioration of the heritage materials, periodic flooding (storm surge/coastal flooding) due to erosion and extreme water levels caused by storms, which causes unplanned over-exposure of subsurface assets, damage and collapse of structural units such as foundations and walls of immovable assets. 136 locations that UNESCO has designated as cultural and historical treasures are thought to be submerged by 2100 due to sea level rise (Perez-Alvaro, 2016).

One major study by Reimann et al., (2018) evaluated UNESCO World Heritage sites in the Mediterranean and found that many are in serious danger of coastal flooding and erosion as sea levels rise. Many of these sites, they have found, are in low-lying coastal localities, vulnerable to storm surges and erosion (Reimann et al., 2018). Similarly, Vousdoukas et al. created an extensive database of African heritage sites, quantifying their exposure to coastal flooding and erosion under a range of climate scenarios. It is anticipated that the number of exposed locations will be more than tripled by 2050, reaching over 200 sites under high emission scenarios Based on this analysis, the authors highlight the need for flood risk assessment methods to be expanded to be applicable in cultural heritage management for the purpose of identifying priorities for preservation efforts (Vousdoukas et al., 2022; M. Vousdoukas et al., 2021)

The rising rate and severity of coastal flooding events much threaten cultural heritage, thus effective mapping and monitoring methods need to be developed. Several studies have identified increased flood vulnerability of coastal heritage sites and call for integrated assessments drawing on the use of advanced space-based technologies, including remote sensing and geographic information systems (GIS) and flood modeling and mapping methods.

In a study, Ravanelli et al., (2019) present a methodology using high-resolution digital surface models (DSMs), geodetic data and sea-level rise (SLR) projections to estimate the inundation risk that the archaeological site of Motya faces. Large DSMs were produced from UAV surveys. Regional vertical land movement (VLM) estimates from local geodetic data were combined with IPCC RCP 2.6 and RCP 8.5 projections to derive relative sea-level rise (RSLR). This allowed for an understanding of which areas are most vulnerable. This methodology represents good practice in its capacity to assess coastal flood risk management strategies, particularly for the protection of cultural heritage.

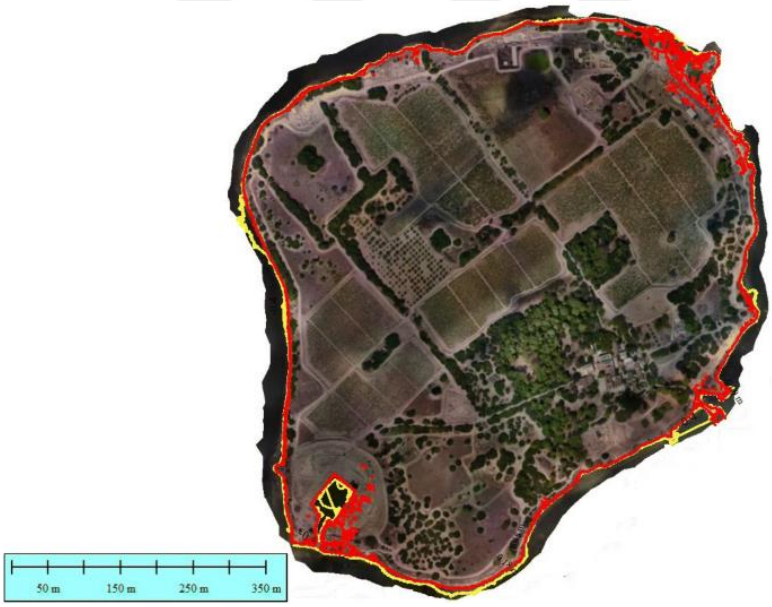



Figure 2.6 The Predicted Shoreline of Motya Island for 2100 under RCP8.5 Emission Scenario (Ravanelli et al., 2019)

A similar procedure is followed by Anzidei et al., (2020). They also combined high-resolution DSMs, vertical land motion (VLM) and the IPCC climate projections, to assess the effect of sea-level rise (SLR) on the Pyrgi heritage site in Italy. A UAV-based photogrammetric survey was used to simulate flooding scenarios for years 2050 and 2100 under RCP 2.6 and RCP 8.5. Land loss by 2100 was substantial (12.6% versus 46.4% using RCP 2.6 to RCP 8.5 extreme high-tide scenarios), including archaeological features such as temples and the Castle of Santa Severa, using the flood risk mapping tidal models. The authors concluded that the results confirm the susceptibility of Pyrgi to coastal hazards of sea level rise (Anzidei et al., 2020).

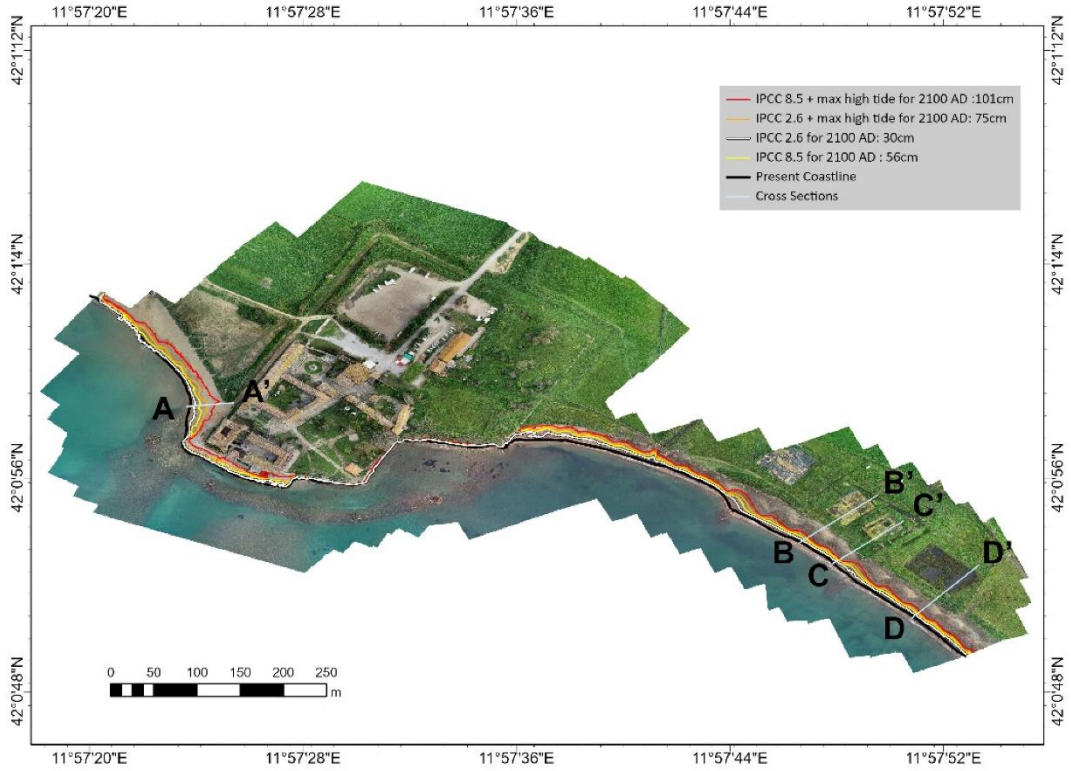



Figure 2.7 Projected Shorelines of Pyrgi for 2100 under different scenarios (Anzidei et al., 2020)

These studies show that use of detailed DSM for the assessment of flood/inundation at the heritage sites is a widely used method.

# CHAPTER 3

# METHODOLOGY

The methods and the data sets used in this study are covered in this chapter. The following steps are performed to answer the research questions of the study:

- Identification of heritage sites that are likely to be vulnerable to flooding due to sea level rise (Site Selection)
- Modeling of flood maps of the selected sites for different sea level rise scenarios for the years 2050 and 2100 using Simple Bathtub Model (SBTM), eBTM and Delft3D
- Obtaining desk-based vulnerability indices for flood vulnerability of the selected sites using CVI (SLR) (Ozyurt, 2007)
- Comparison of desk-based vulnerability indices with flood maps
- Investigating the sensitivity of flood maps to the method of modeling, the type of data set, and the characteristics of the data set.

Within this scope, this chapter is conceptually divided into three parts: site selection, flood mapping, and desk-based vulnerability. The first section "Datasets" introduces the data sets used for each part, their sources, constraints, preprocesses, and technical details.

## 3.1 Datasets

### 3.1.1 Türkiye Coastal Heritage Sites Database

The heritage site archive gathered in the scope of the TÜBİTAK Project 122M613 is used for the site selection. This archive is a country-broad database created by the combination of different official databases. These are:

- The environmental order plans of the Republic of Türkiye Ministry of Environment Urbanisation and Climate Change. (www.mpgm.csv.gov.tr)
- ATLAS database of the General Directorate of Geographic Information Systems, Republic of Türkiye Ministry of Environment Urbanisation and Climate Change. (www.atlas.gov.tr)
- The GIS (Geographic Information System) layers obtained from the Republic of Türkiye Ministry of Environment Urbanisation and Climate Change and the Ministry of Culture and Tourism (Kösem et al., 2023)
- Türkiye Culture Inventory. (Kültür Envanteri, 2019) (https://kulturenvanteri.com/tr/)

This database was created in a GIS environment with layers from the ministry and manually digitized data from other databases within the TUBITAK project. The digitizing was done using QGIS, where the polygons indicating the heritage site borders were drawn using the environmental order plans and the information about the area was obtained from the Culture Inventory and ATLAS database so that the missing attributes like site name, area, and level of conservation, would be filled. In the TUBITAK project's scope, a “coastal site” is defined as a site with an area below 10 m elevation or within 1 km from the shoreline (Kösem et al, 2023). According to this classification, the number of coastal cultural heritage sites in Türkiye is given in Table 3.1. After merging the above-mentioned databases in the GIS environment for the coastal towns of Türkiye, the dataset is filtered down accordingly with the “coastal heritage” definition. It should be noted that İstanbul was excluded from this database as the city is overloaded with coinciding heritage sites as it is one of the oldest capitals in the world. These sites are directly under use and effect of daily human life and many other industries, which indicated further detailed and specific parameter investigation in terms of vulnerability. This database covering the coastal archaeological and natural heritage sites of 27 coastal towns of Türkiye was used for the site selection of this study.

Table 3.1 Number of Coastal Heritage Sites According to the Criteria and Heritage (Kösem et al., 2023)

| Heritage Type | *Archeological* | *Natural* |
|---|---|---|
| Below 10 m Elevation | 527 | 416 |
| Within 1 km Distance from Shoreline | 714 | 470 |
| Satisfying Both Criteria | 499 | 407 |

### 3.1.2 Rate of Sea Level Rise

The sea level rise data is obtained from the Sea Level Projection Tool of National Aeronautics and Space Administration (https://sealevel.nasa.gov/ipcc-ar6-sea-level-projection-tool). This tool's projections are based on the Sixth Assessment Report of IPCC (AR6) (Calvin et al., 2023). It covers projected sea level rise rates for every 10 years up to 2100 for the five Shared Socio-economic Pathways presented in the AR6 report. This dataset is used both in the flood mapping to obtain the inundation depths at the study sites and it is also a parameter for the inundation module of CVI-SLR vulnerability analysis (Özyurt, 2007).

### 3.1.3 Extreme Water Levels

Extreme water level data includes storm surges with a return period of 100 years, tides and projected sea level rise due to climate change. This data is used to analyze the temporary flood areas that will be observed under extreme weather conditions on top of the inundated areas due to climate change driven sea level rise, and for the flood module of CVI-SLR. For this purpose, two datasets with extreme water level predictions on the Turkish coast have been analyzed in detail.

#### 3.1.3.1 LISCOAST: Large Scale Integrated Sea-level and Coastal Assessment Tool (Vousdoukas et al., 2018)

This dataset provides probabilistic forecasts of Extreme Sea Levels (ESL) along the global coastline through to the end of the twenty-first century, incorporating factors such as mean sea level, tides, waves, and storm surges. The extreme water level definition of this data set is given by Equation 3.1.

$$ESL = MSL + \eta_{Tide} + \eta_{CE} \quad 3.1$$

In the equation, MSL is the mean sea level, $\eta_{Tide}$ is the high tide water level and $\eta_{CE}$ is the water level fluctuations because of climate extremes. The data set employs a probabilistic process-based approach to account for global sea-level projection uncertainties. This uncertainty mostly derives from the uncertainty of the ice sheets of Greenland and the Antarctic (M. I. Vousdoukas et al., 2018). The emission scenarios used in LISCOAST study are based on the Representative Concentration Pathways (RCP) presented in the Fifth Assessment Report (IPCC, 2014). These pathways represent four different projections of the global greenhouse gas emissions, atmospheric concentrations, air pollutants and land use.

- **RCP2.6:** Scenario where strict measures are taken to keep global warming below 2 C° by reaching negative emission rates.
- **RCP4.5- RCP6.0:** Moderate scenarios where the emission rates reach a peak then decrease and reach a constant level at the end of the century. For RCP 4.5, the peak and the stabilization happen much earlier at a lower emission rate then RCP6.0.
- **RCP8.5:** This is the business-as-usual scenario where no emission constraints are implemented and the GHG emissions are at the highest level.

The analyses resulted in individual probability density functions for each contributing element of the extreme sea levels that vary in time and space. A time

and space-varying PDF for the ESL values is obtained worldwide using Monte Carlo simulations to combine these PDFs.

The ESL values from this database are tables for different emission scenarios, return periods, and confidence intervals in the raw form for the global coastlines. For this thesis, the median values for the years 2050 and 2100, with the $\eta_{CE}$ with 100-year return periods for the emission scenarios, RCP 4.5 and 8.5 are used.

After filtering the global raw tables for the selected years, return period, and scenarios, the dataset was cropped to account only for the Turkish coasts using QGIS. For further investigation and discussion, the percent changes between the base year 2050 and 2050-2100 and the difference between these percent changes were calculated. The data points obtained with approximately 20 km spatial resolution are shown in Figure 3.1.

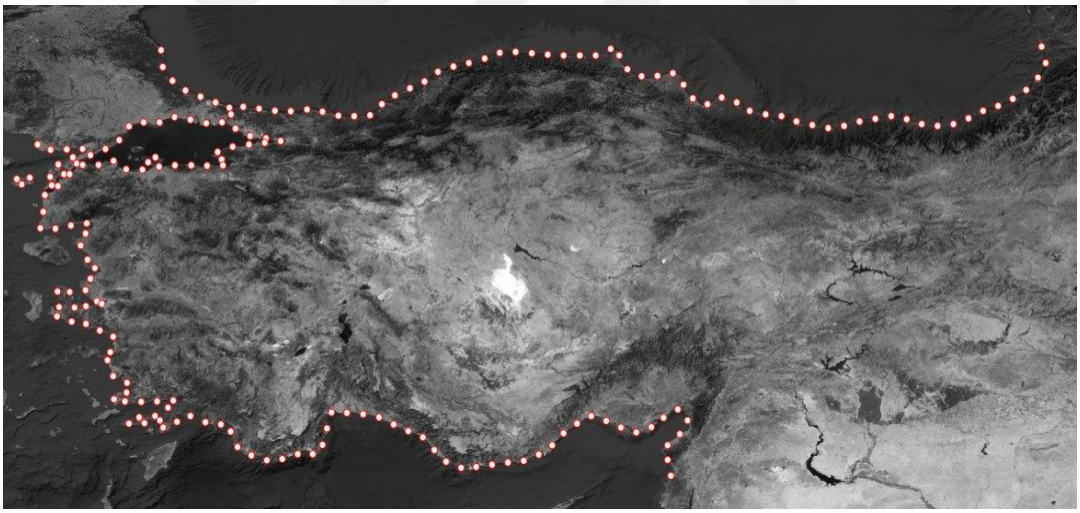


Figure 3.1 LISCOAST EWL Data Points Along Turkish Coasts

After downscaling the dataset for the Turkish coasts, the extreme water level values are assigned to the heritage sites using the closest data point to the area using QGIS.

The methodology of LISCOAST ignores nonlinear interactions between extreme water level components and treats them as independent variables. This limitation of the dataset is due to the considerable computational challenge of modeling the

nonlinear relationships between variables that cannot be overcome at global scale. In addition, it has been shown in previous studies in the literature that these nonlinear interactions are only locally significant (Pugh, 1996). Another limitation is that land movements are ignored when quantifying the rise in sea level. The local effect of sea level may increase or decrease with local ground subsidence or uplift. In addition, episodic erosion or accretion of shorelines caused by tidal and extreme events is ignored, and the shoreline is assumed to remain constant throughout the modeling (M. I. Vousdoukas et al., 2018).

#### 3.1.3.2 Kirezci et al. (2020) Dataset

The other extreme water level dataset Kirezci et al. (2020) is of similar concept with Vousdoukas et al. (2018). The extreme water level definition of this dataset is:

$$TSL(t) = T + S + WS \qquad 3.2$$

In Equation 3.2, TSL represents the assumed total water level, T is the tide, S is the surge and WS is the wave setup. For the extreme water level projections, this summation is coupled with the RSLR of the RCP 4.5 and 8.5 of IPCC AR5 (Kirezci et al., 2020). The dataset provides extreme water level projections for the years of 2050 and 2100 under RCP4.5 and RCP8.5 scenarios at a global scale with 9866 total data points.

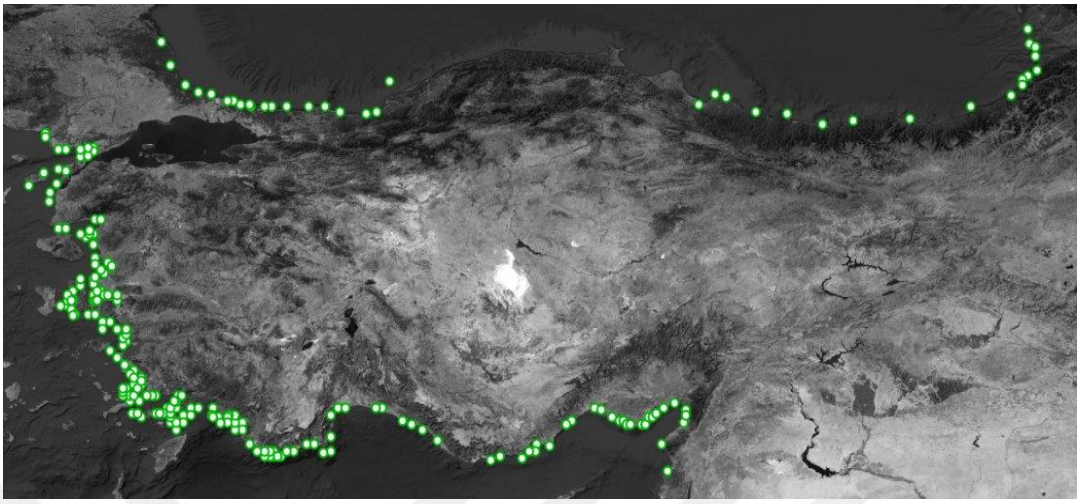


Figure 3.2. Kirezci et al. (2020) EWL Data Points Along Turkish Coasts

Unlike LISCOAST, Kirezci dataset does not provide data everywhere for the Turkish coast. Figure 3.2 shows the data points for the Turkish coasts and the lack of data for the Marmara Sea and the Central Black Sea. Furthermore, Kirezci dataset does not provide data points at regular intervals like LISCOAST, as it employs a different dataset for the data points.

The dataset was provided by the dataset owners as a point data layer in .kml format. The layer was transferred to QGIS to crop the data for Turkish coasts. Then, the same additional variables were calculated regarding the percent changes between the present, 2050 and 2100. This database was used to compare EWL values with those of LISCOAST to include the uncertainties of different EWL databases in the flood maps.

As for the limitations of this database, Kirezci dataset also ignores the non-linear interactions between water level components and does the summation linearly. Although it causes a relatively minor error except for certain locations, the dataset assumes a global average coastal bed slope which affects the wave set-up calculations. Moreover, tidal gauge data, which is used for validation, might not accurately depict wave setup, particularly in regions with short tidal ranges or semi-enclosed basins like the Mediterranean or Baltics (Kirezci et al., 2020).

### 3.1.4 Topography and Bathymetry

The most important variable in the present research is the topography data. To improve the model results and evaluate how sensitive the flood maps were to the type and resolution of the data, several digital elevation models were employed to depict the terrain. These digital elevation models are introduced below:

- Copernicus GLO-30 DEM

  This digital elevation model is of 30 m resolution, covering all of Europe, and is available worldwide. It has an absolute vertical accuracy of <4 m and an absolute horizontal accuracy of <6 m (European Space Agency & Airbus, 2022). The data is available in ESRI Shapefile format.

  After obtaining the data, it is cropped using ArcGIS for the Turkish Coasts for a buffer area of 2 km from the shoreline to determine the elevations of heritage sites that have an area within 1 km distance from the shoreline. This dataset was used for the preparation of GIS-based flood maps. Figure 3.3 shows a portion of the DEM data for the Ancient City of Knidos in Datça, Türkiye.

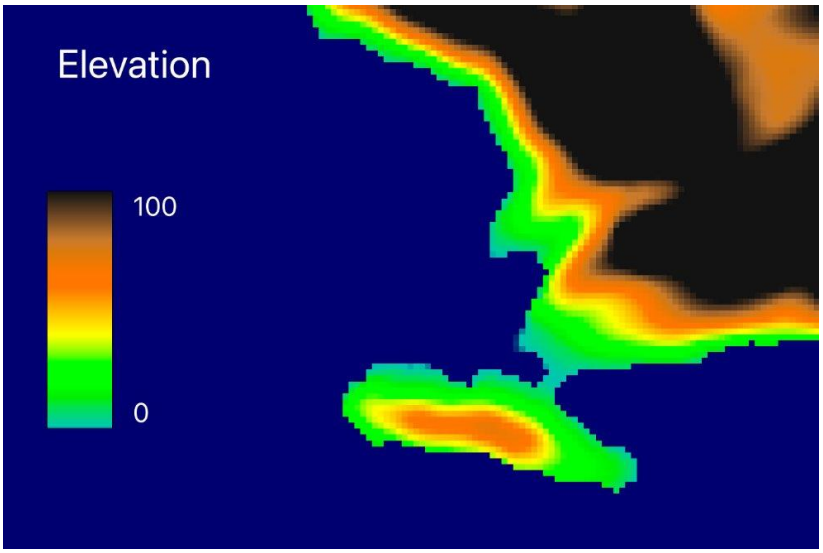



Figure 3.3 Copernicus GLO-30 DEM data for Ancient City of Knidos, Datça, Muğla

- SYM-5 and Bathymetry

This 5 m resolution elevation model, which is a combined bathymetry and surface model, was used in Dogan et al., 2021 on the modeling of the 2020 Tsunami in Sığacık, and was provided in .tif format by the authors for this project. The dataset used was created by combining the SYM-5 elevation model created by the General Directorate of Maps, and bathymetry data by Office of Navigation, Hydrography and Oceanography of Turkish Naval Forces. This elevation model available for the ancient city of Teos was used for both GIS-based flood maps and dynamic flood modeling with Delft3D.

- High-Resolution DTM-DSM

In the scope of the TÜBİTAK Project, the surface model of some selected sites was planned to be generated with an unmanned aerial vehicle. Out of the selected study sites, high resolution models were captured for the ancient cities of Teos, Anemurium and Soli-Pompeipolis. The model generation was carried out by I4works company with SiteEye application developed by them (https://siteeye.co). The type of drone used was Mavic Pro and a model with 2.5 cm/pixel resolution was built using several ground control points and a 5 cm x 5 cm raster was produced. Figure 3.4 illustrates the model generated for Teos.



Figure 3.4. The 3D SiteEye model of the Ancient City of Teos

Both DTM and DSM datasets were obtained in the format of point clouds and converted into .tif raster formats for operational feasibility. Due to the large size of sites and operational constraints, models were generated focusing on the coastal portions instead of the whole cultural heritage site.

### 3.1.5 Landcover

The Coastal Zones Land Cover/Land Use 2018 dataset offers comprehensive information about the land use and land cover (European Environment Agency, 2020). The dataset includes 71 thematic groups along the European coastline referenced to 2018. The data is obtained in the vector format and operated in QGIS environment. Figure 3.5 illustrates this vector layer as an example for Antalya and obtained for the entire Turkey.

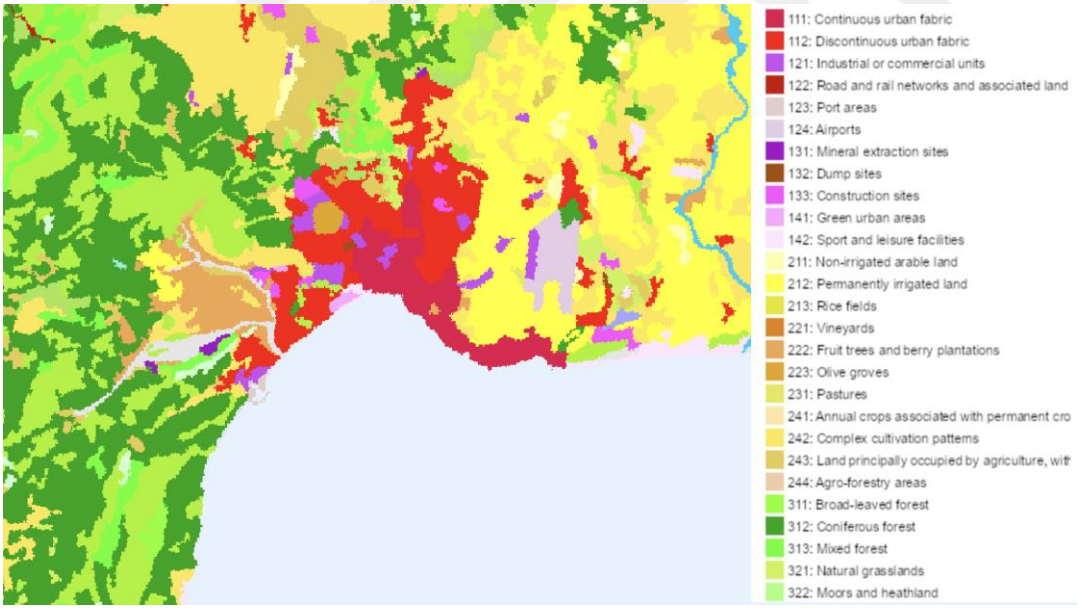



Figure 3.5 Land Cover Types of Antalya Province (EEA, 2020)

This vector layer was cropped following the project's definition of a coastal area, and the land cover/use codes corresponding to the heritage sites were obtained by

overlapping the layer with the polygons of the protected areas. The landcover data is used for the eBTM application to obtain the relative surface roughness values.

### 3.1.6 Coastal Slope

For this parameter, no readily available slope dataset for the coasts of Türkiye integrates bathymetry and topography at the coast. Therefore, the dataset had to be built within the TÜBİTAK Project 122M613. The elevation information is from the same database used in the flood modeling, GLO-30 of Copernicus. For the bathymetry, the broadly used commercial bathymetry services was not sufficient as the project requires detailed coastal slope information. Therefore, the bathymetry close to shore was obtained from the maps of Turkish Naval Forces Office of Navigation, Hydrography and Oceanography and the offshore parts were obtained from EMODNET Bathymetry of European Commission (Available at https://emodnet.ec.europa.eu/en/bathymetry). Merging these two datasets, the coastal slope was calculated together with the DEM, using the "Slope" function of ArcGIS.

### 3.1.7 Tidal Range

In scope of the TÜBİTAK Project 122M613, a database of the tidal ranges at the Turkish coasts is built on the GIS environment. The values are obtained from the FES2014 database provided by Aviso Altimetry as tidal constituents. Since Türkiye is in the micro-tidal region, only the Principal Solar (S2) and the Principal Lunar (M2) tidal constituents are considered, which are already relatively small. When these constituents coincide, the maximum tide is reached, which is known as the spring tide, and when they cancel each other, the minimum tide happens, which is known as the neap tide. The values for these constituents are obtained and the neap and spring tides are calculated for the data points around Turkish coasts using QGIS.

### 3.1.8 Engineered Frontage

This parameter indicates how much of the shoreline is built up for human activities. The ratio of area of structures that don't have a purpose of protecting the shoreline to the study area are presented as percentages of the shoreline to indicate the engineered frontage parameter, these built areas change the physical processes along the shoreline and affect the vulnerability of the area. For this parameter, the Copernicus Land Cover dataset (EEA, 2021) is used with the Google Earth Satellite views and ATLAS Portal of the Ministry of Environment, Urbanization and Climate Change of the Republic of Türkiye.

### 3.1.9 Natural Protection Degradation

This parameter accounts for the natural formations along the coast that protect the area against flooding. Dunes, marshes, wetlands, etc., either directly stop flooding or decrease its impact, thus reducing the vulnerability of the shoreline. When human activities degrade these formations, the vulnerability of the coastline increases. Hence, this effect should be included in the computations. For this parameter, the Copernicus Land Cover dataset (EEA, 2021) is used with the Google Earth Satellite views and ATLAS Portal of the Ministry of Environment, Urbanization and Climate Change of the Republic of Türkiye.

### 3.1.10 Coastal Protection Structures

This is the parameter that accounts for the protection structures along the shoreline. The principal function of these structures is to protect the shoreline against flooding and erosion such as seawalls and groins. This parameter is also calculated as percent ratio of the area that is protected by such structures. For this parameter, the Copernicus Land Cover dataset (EEA, 2021) is used with the Google Earth Satellite

views and ATLAS Portal of the Ministry of Environment, Urbanization and Climate Change of the Republic of Türkiye.

## 3.2 Site Selection

Since the vulnerability of heritage sites in Türkiye to sea level rise has not been assessed before, factors that might indicate vulnerability to flooding were selected based on CVI(SLR) model (Özyurt, 2007) and some heritage-specific parameters. Having obtained the database of the coastal heritage sites of Türkiye in a GIS environment within the TÜBİTAK Project 122M613, all the coastal heritage sites of Türkiye were evaluated based on these parameters to select the study sites of this thesis. These parameters were assessed using the datasets presented in the previous section.

The physical parameters considered during the site selection are:

- Elevation of the Site Above Sea Level
- Length of the Shoreline
- Predisposition of the Coast to Experience Storms

The vulnerability of the archeological site is also defined in terms of its “value” as being designated "more important" by the government would make the site more vulnerable in addition to these physical factors. The parameters taken into account in this context are:

- Degree of Conservation
- Status of the Remains

### 3.2.1 Elevation

The area's elevation is the most essential factor in determining its vulnerability to floods when screening it. Choosing regions susceptible to flooding is vital when the

area's elevation is compared to the predicted extreme water levels. As there are different coastal formations with various slopes, an area right at the shore does not mean it is prone to flooding (Figure 3.6). The average elevation of the shore directly affects the extent of inundation, and elevation is a direct parameter of the vulnerability model used in this study. Therefore, the elevation regimes and coastal types of coastal heritage areas were investigated. In site selection, the sites which have the lowest elevation levels along the shoreline were considered as the vulnerable sites and considered for model study candidates.

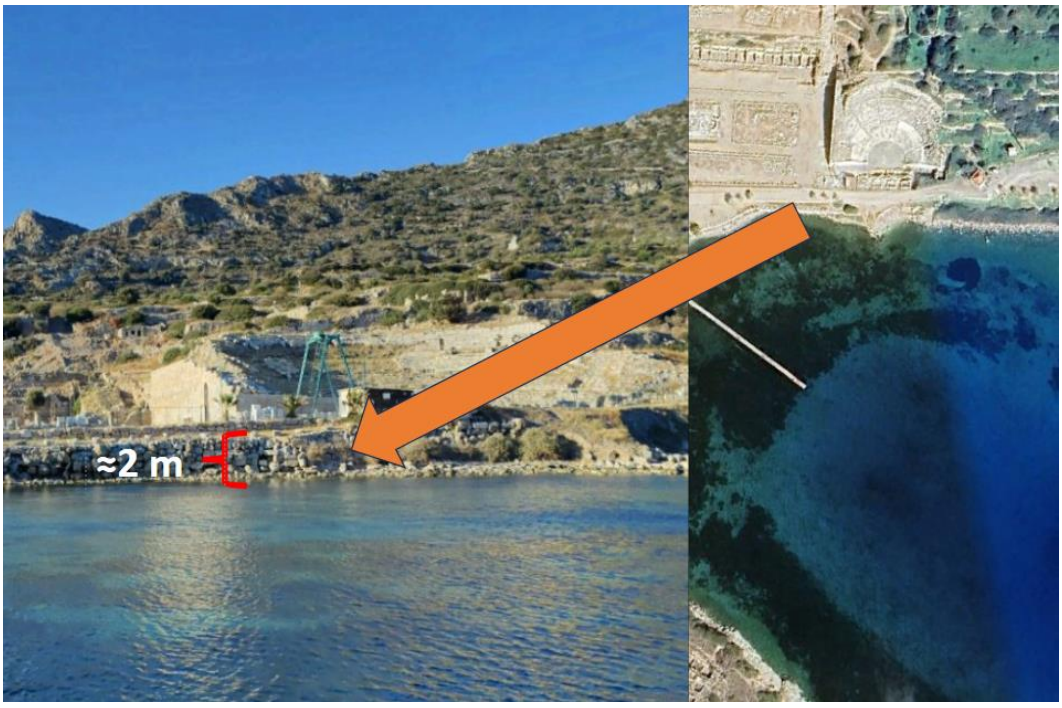



Figure 3.6. Satellite view and Coastal Formation of the Ancient City of Knidos, Datça, Türkiye (Google Earth, 2024)

### 3.2.2 Shoreline Length

Flooding by the sea level rise and storm surges is directly proportional to the extent of the area’s interaction with the sea. An area with a longer shoreline would be more vulnerable to the impacts coming from the sea compared to one with a short sea-land interaction length. Some archaeological heritage sites are located in narrow bays or

spread inland due to other geographical challenges. These areas will experience limited pressure during storms, concluding that areas with longer shorelines should be prioritized. To illustrate, the Ancient City of Anemurium and Adrasan Archaeological Site are shown in Figure 3.7. Although both areas qualify as coastal heritage sites according to the classification of the TÜBİTAK Project 122M613, their extent of interaction with the sea causes differences in their vulnerabilities. The sites with short shorelines were considered having low vulnerability and long shorelines indicated high vulnerability.




Figure 3.7. Anemurium and Adrasan Heritage Sites with Different Shoreline Lengths (Red lines representing heritage site borders) (Google Earth, 2024)

### 3.2.3 Predisposition of the Coast to Experience Storms

As stated in Chapter 2, the definition of extreme water levels includes storm surge heights. Mapping the extent of flooding under extreme weather conditions being among the main objectives of this study, selected area must be open and vulnerable to storms as much as possible. In this context, the type of coastal formations and the fetch distances from the seaward directions assume significant importance. The criteria considered can be explained as follows:

- The shoreline should be open for wave and wind impact.

- The site should not be in a narrow or closed bay that would limit wave and wind action.
- The topography should allow long fetch distances.

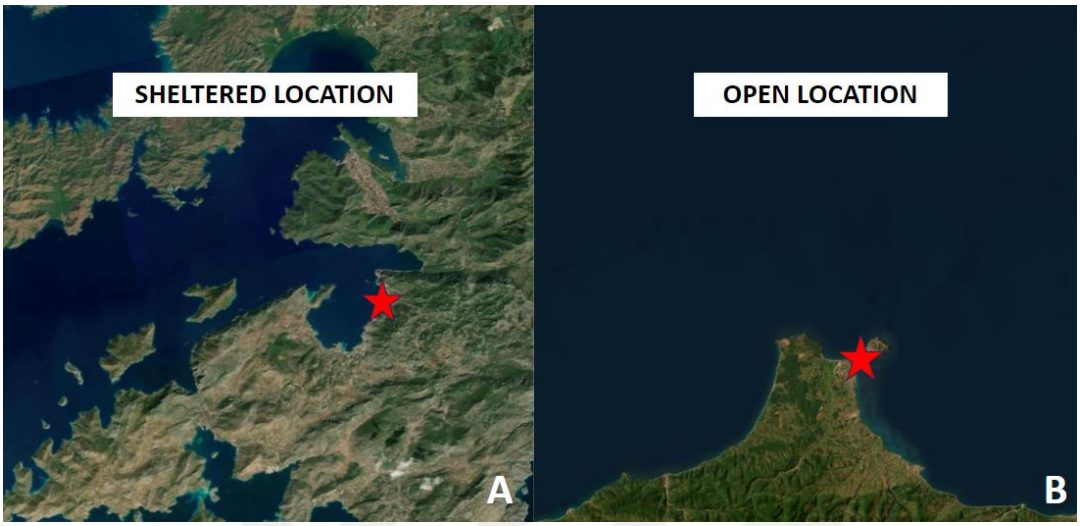



Figure 3.8. Two Coastal Heritage Sites with Different Storm Predispositions (Google Earth, 2024)

Figure 3.8 shows two heritage sites. It is evident that these sites will not be equally affected from a storm with the same intensity. The geography of the Location A creates a natural shelter for the wind and wave actions, which means the expected surges would be smaller here. Hence, heritage sites with open locations like Figure 3.8 -B were prioritized as they are considered more vulnerable.

### 3.2.4 Level of Conservation

All the heritage sites protected by the law are classified in three levels by the Republic of Türkiye Ministry of Culture and Tourism (Arkeolojik Sitler, Koruma ve Kullanma Koşulları, 1999). This classification not only indicates the importance of the heritage area, but also the level of conservation and what kind of operations are allowed inside the borders of the area designated as a heritage site. There are currently three degrees of conservation. The definitions of these classifications are set by the Ministry as (Arkeolojik Sitler, Koruma ve Kullanma Koşulları, 1999):

a) *I. Degree Archaeologic Site:* Areas where only scientific operations performed for the conservation of the area is allowed. Any kind of construction is strictly forbidden in these areas.
b) *II. Degree Archaeologic Site:* Areas that should be conserved but the conservation and the utilization conditions is determined by Conservation Boards. Simple repairs of unregistered buildings currently in use may be carried out, but no new construction is allowed in these areas.
c) *III. Degree Archaeologic Site:* Areas where new arrangements may be permitted in line with conservation decisions. The building density shall not exceed the density determined by the zoning plan.

During the prioritization, the degree of protected sites, which indicates the importance of the sites for both the ministry and the local people, was considered. It is seen that most of the sites in Türkiye are classified as either first or third-degree conservation levels.

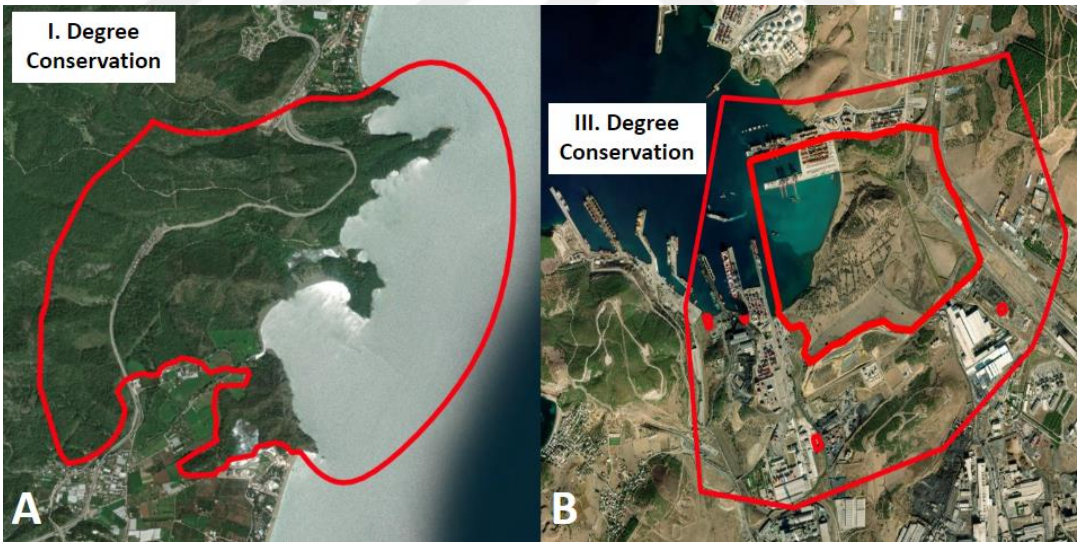



Figure 3.9. Two Archaeological Sites with Different Degrees of Conservation (A: Ancient City of Phaselis, B: Ancient City of Kyme) (Red lines representing heritage site borders) (Google Earth, 2024)

In Figure 3.9, two ancient cities with different degrees of conservation are shown. The differences in the permitted operations in these heritage sites are clearly visible

on these maps. Because of all the constructional and industrial pressures on the third-degree sites, the vulnerability of these sites might require different parameters. Moreover, since construction operations are not prohibited in these areas, the level of risk might completely change by the years for which the flood analysis has been carried out. Therefore, sites with first-degree conservation indicated high-vulnerability and third-degree conservation indicated low vulnerability.

### 3.2.5 Status of the Remains

There are two classifications for the status of the remains in the sites. The first is about the type of heritage site, and the second is the condition of the remains. The coastal heritage sites database showed that only some sites classified as archaeological are ancient cities; there are also singular monuments, sanctuaries, or forts that fall into the same classification. Considering the objective is to model flooding extent and express an area's vulnerability, only the sites that can be expressed as large land areas were considered. Therefore, mostly ancient cities were considered in the site selection for the modelling studies. It should also be noted that the vulnerability of the monolith-type heritages (single monuments, forts, single buildings, etc) to flooding would require different additional parameters. For those types of heritage sites, as direct material-seawater interaction would gain importance and the water would rise directly on the surface/wall of the heritage, the current parameters might need to be revised.

While investigating ancient cities, a specific focus was placed on the presence of elements such as remains or ruins excavated and unearthed. This is also another indicator of the attention and importance paid to the area. Therefore, sites that have never been excavated were not considered. On the other hand, particular emphasis was placed on identifying ancient harbors as evidence of long-standing interaction between the area and the sea.

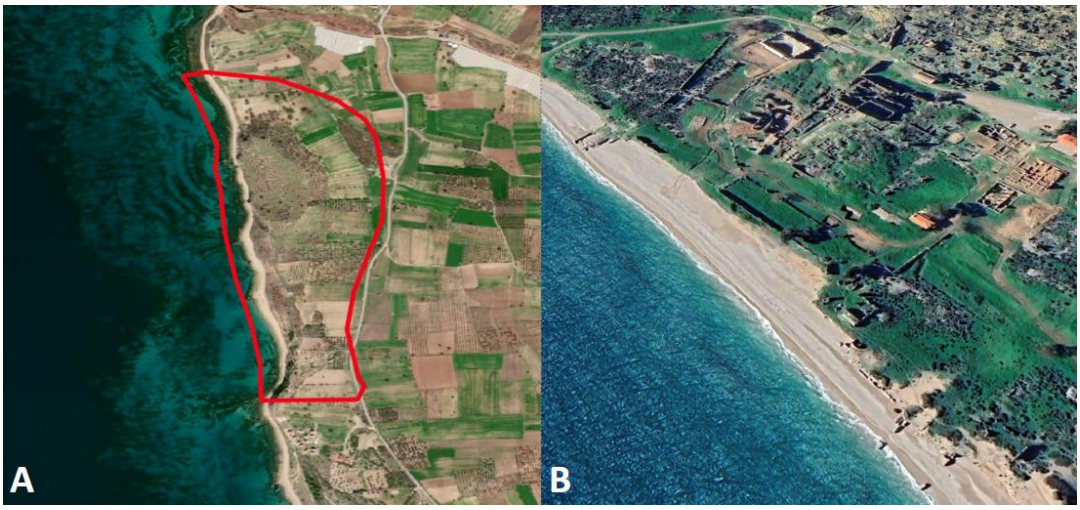



Figure 3.10. Totally unearthed and earthed heritage sites ( A: Ancient City of Colorna, B: Ancient City of Anemurium) (Red lines representing heritage site borders) (Google Earth, 2024)

## 3.3 Flood Modeling Methods

The flood methods used and compared in this study are simple bathtub modeling, enhanced bathtub modeling, and hydrodynamic modeling.

### 3.3.1 Simple Bathtub Model (sBTM)

This model solely uses the elevation data of the area and compares the elevation to the predicted increase of sea level to determine the flooded areas. The method assumes areas below a certain elevation will be flooded without considering any other parameter. The areas' digital elevation models (DEMs) are obtained as raster layers in the GIS environment. A raster data is a group of pixels where each pixel represents the value of a parameter, in this case, the elevation.

For all the GIS processes, QGIS and ArcGIS Pro programs are used interchangeably, depending on the limitations and ease of application of specific commands and tools used in the study. The procedure of performed sBTM is as follows:

1. Using the DEM raster to find where the desired water level corresponds to in the terrain:
    a. This is done using the “contour polygons” command in QGIS. This command creates polygons between the contour lines with the desired intervals. The contour polygons with an interval equal to the projected extreme water level are generated.
    b. Since this command produces polygons inside the limits of the raster's elevation range, the surplus polygons should be deleted so that only the polygon corresponding to the area between 0 m and the elevated water is left on the terrain.
2. Fixing the hydro-connectivity manually:
    a. The “contour polygon” command scans the entire area and draws contour lines at the specified height everywhere. As a result, polygons representing inundation will appear in the area, even if they are not connected to the coastline. To correct this, the polygons that are not connected to the shoreline polygon have been manually removed.
3. Smoothing:
    a. Due to the resolution of the DEM data and the pixels' quadrilateral nature, the contour polygons may have hard corners. This would be unrealistic as these polygons represent water bodies. For this reason, the edges of these polygons should be smoothed so that the area occupied by the liquid can be shown more realistically. The “Smooth” tool of the QGIS program is used.
4. Determining flood area and depth:
    a. To obtain the depth and extent of the inundation, the coastline indicated by the DEM data must be determined. The contour 0 m is drawn and smoothed to account for the shoreline. The polygon area beyond this line is the flooded area. The flood polygon is split into two to determine the area using the shoreline layer using the “split vector” command of QGIS. This results in two polygons, one

showing the newly flooded area and one showing the area that is already a body of water. Thus, the extent of the flood area is determined by calculating the perimeter and area information of the second polygon.

### 3.3.2 Enhanced Bathtub Model (eBTM)

The eBTM model is an upgraded version of the sBTM method. As explained in Chapter 2, this method utilizes the slope and roughness of the surface in addition to the elevation data. This enables to model the water progress and intrusion on land more realistically. Williams and Lück-Vogel (2020) developed an ArcMap tool for this method. ArcCoast Toolbox (Williams & Lück-Vogel, 2020) is open-source and available online. The toolbox is compatible with ArcMap 10.3 and has an interface where the GIS layers of shoreline, DEM, and uniform roughness of the area are entered as input. This toolbox is used for the eBTM applications.

In addition to the data required for the other methods, this method requires surface roughness information. Surface roughness depends on the soil texture, surface moisture, vegetation, and aggregation.

#### 3.3.2.1 Work Principle

Rather than directly increasing the water level to the desired elevation, this method considers the slope of the surface to simulate the progress of water better, and the effect of roughness is included by considering it as a factor that changes the slope. The model area is assigned a constant roughness coefficient that changes between 0-1, where one is the smoothest and 0 is the roughest coefficient, employing FEMA (2007). This coefficient is used to modify the slope angles of the raster pixels, which is obtained in a GIS environment using the DEM raster with the spatial analyst tool, so that if the surface is smooth (roughness coefficient:1), the slope won't be changing, if it is rough, it will be increased by a factor close to 0. Next, the modified

slope is put into a cost analysis, where the least costly path is analyzed between the pixels of the raster layer; this simulates the water path the water will choose to follow with the given roughness. In the end, the traveled pixels resemble the flood area (Williams & Lück-Vogel, 2020)

#### 3.3.2.2 Surface Roughness of the Study Sites

The roughness coefficient of the areas is decided depending on the land cover of the area. The Coastal Zones Land Cover/Land Use 2018 vector dataset of the Copernicus Land Monitoring Services is used for the land cover. The variety and distribution of the land cover types in the study sites provided by the dataset are shown in Figure 3.11-Figure 3.14:

- Ancient City of Aleksandria Troas

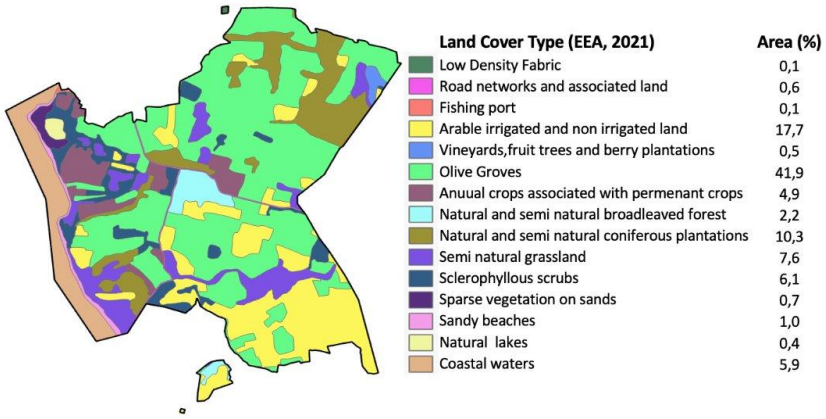



Figure 3.11. Land Cover of the Ancient City of Aleksandria Troas retrieved from Copernicus Coastal Zone Land Cover (2021)

- Ancient City of Teos

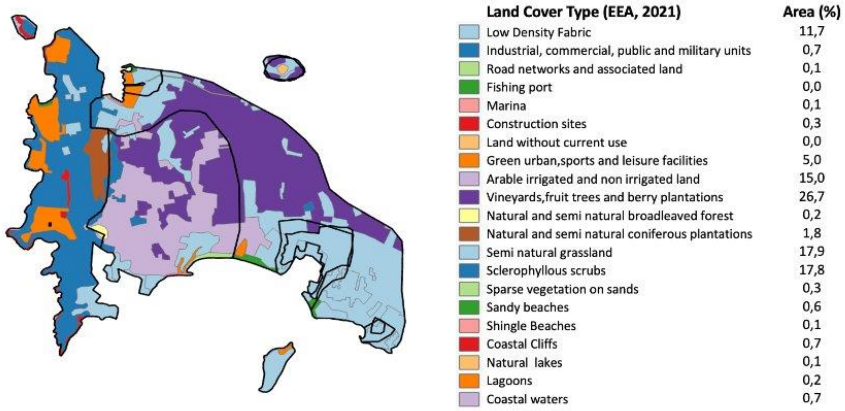



Figure 3.12. Land Cover of the Ancient City of Teos retrieved from Copernicus Coastal Zone Land Cover (2021)

- Ancient City of Anemurium

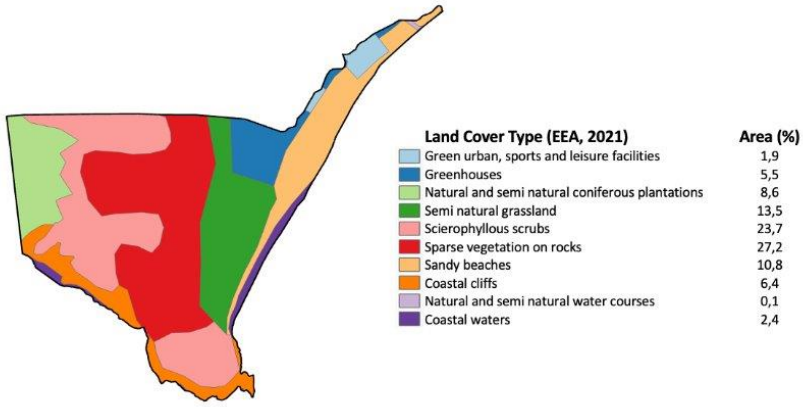



Figure 3.13. Land Cover of the Ancient City of Anemurium retrieved from Copernicus Coastal Zone Land Cover (2021)

- Ancient City of Soli-Pompeipolis

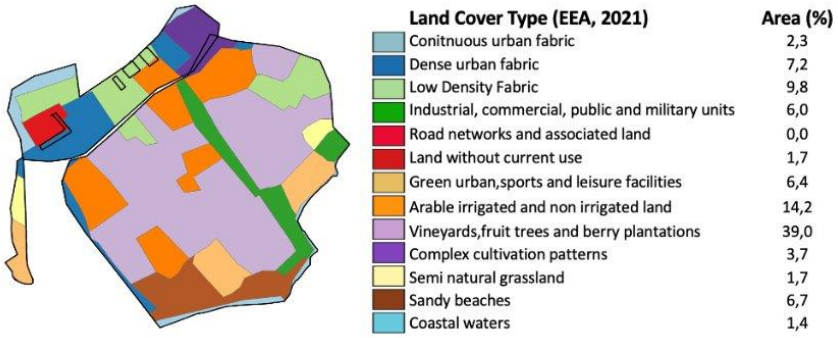



Figure 3.14. Land Cover of the Ancient City of Soli-Pompeipolis retrieved from Copernicus Coastal Zone Cover (2021)

Although the study areas have a wide variety of land use types, only the land use type in the expected flood-prone area is important for the eBTM application. Considering this, the most prominent land uses of the selected sites are found to be sandy beaches, semi-natural grasslands, agricultural land, vineyards. The roughness coefficient values used in eBTM were based on FEMA (2007), which takes values between 0-1. Williams & Lück-Vogel (2020) used the roughness for sandy beaches as 1 in their study of eBTM, which means the effect of roughness is lowest on the flooding. Accordingly, the flood-prone areas of the selected heritage sites being mostly sandy beaches, a uniform coefficient of 1 was used for this study. Also, taking the roughness coefficient as 1 provides a conservative approach since the largest possible flood area would be evaluated. The shoreline, which will be the water source in the eBTM model, was selected as the 0.01 m contour of the DEM used. After this contour was created, it was smoothed to match the natural coastline to eliminate the angularity of the raster pixels.

The biggest limitation of this model is the assumption of a single uniform roughness coefficient for the model area. In reality, the roughness in such a broad area would differ. Another limitation is the model being built in compatibility with FEMA coefficients, as there is no valid way to convert the roughness coefficients to each other. Like all the flood models, another limitation is the level of detail of the

databases used for the model. The GLO-30 DEM data has a spatial resolution of 30 m which is a very large area to assess flooding at a single step.

### 3.3.3 Hydrodynamic Model: Delft3D

As one of the objectives of this study being the investigation of the effect of realistic modeling of hydrodynamic processes to obtain the flood maps, Delft3D is used to obtain a dynamic flood map. Delft3D is a widely used multi-module numerical model developed by Deltares.

GIS-based flood maps are prepared for EWL with 100-RP, where each component of the EWL, which are MSL, tide and climate extremes, considered as a constant number given by the dataset that rises the water level. In the numerical model, the SLR is used to obtain the MSL in 2100, and the tide and the climate extreme are modeled dynamically, where climate extreme accounts for the surge height of a 100-year-RP storm. To clearly see the difference between the bathtub models, the flooded shoreline of the worst-case scenario RCP8.5 is used. In this context, the methodology followed for this part can be summarized as:

i) Make an extreme wave statistics analysis for the region.
ii) Select a historical 100-year RP storm to model to obtain the current flood extent.
iii) Model this storm with the 2100 still water levels and obtain the flood extents.
iv) If data for such a historical storm is not found, model a historical storm that is closest to a 100-year RP storm and generate a synthetic 100-year RP storm to obtain the flood extents.

#### 3.3.3.1 Extreme Wave Analysis

For the extreme wave analysis, the hourly significant wind wave height, wave period and wave direction data for the area is obtained from the database ERA5 Hourly Data on Single Levels from 1940 to Present (C3S, 2018) for 40 years between 1984-2023. Figure 3.15 shows the points this database provides data near Teos. It was decided that the circled point with coordinates 37.8°N, 26.5°E is the most appropriate one to use.

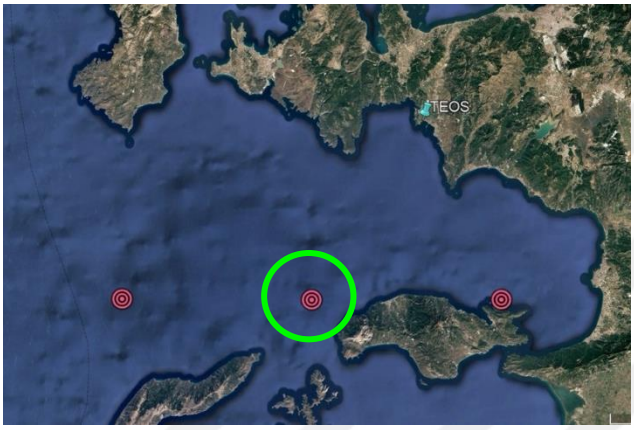



Figure 3.15 ERA5 Data Points of Hourly Data on Single Levels Database Near Teos

As the classic Extreme Wave Statistics procedure follows, the annual maxima for the past 40 years are extracted from ERA5 data (Figure 3.16).

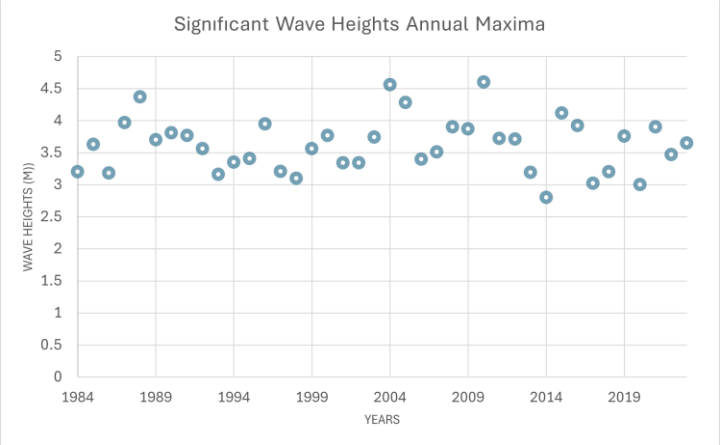



Figure 3.16 Annual Maxima Significant Wave Heights between 1984-2023 for Teos

The analysis resulted in the Gumbel distribution having the best fit to this data. The resultant wave heights with corresponding return periods are given in Table 3.2.

Table 3.2 Significant Wave Height of Corresponding Return Periods

| Return Period | *Significant Wave Height (m)* |
|---|---|
| 5 | 3.96 |
| 10 | 4.23 |
| 100 | 5.1 |
| 1000 | 5.91 |

Using all the data obtained from the ERA5 database, the deep-water wave steepness is calculated as 0.049 by drawing a fit to wave height vs. deep-water wavelength plot (Figure 3.17).

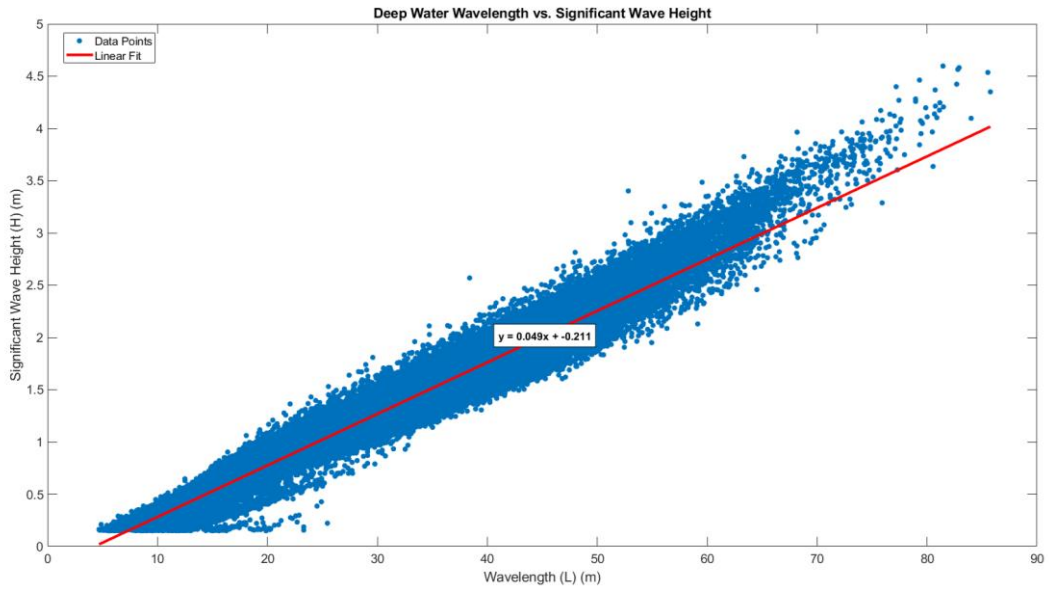



Figure 3.17 Deep-water Wavelength vs Significant Wave Height Graph for the past 40-year data

The resultant steepness, which is the slope of the fitted line, is used to obtain the periods of the 100-year RP storm wave heights.

### 3.3.3.2 Storm Selection

After obtaining the 100-year RP storm parameters, the data of the region is scanned to select a historical 100-year RP storm. However, as can be seen in Figure 3.16 such a storm hasn't happened in the past 40 years according to ERA5 data, which led this study to the generation of a synthetic storm.

On the other hand, an existing storm was selected among the ERA5 data to model and compare the present and future flood conditions. For this historical storm, a storm that happened on January 6$^{th}$, 2012, has been selected, wave and wind data time series of which are shown in Figure 3.18 and Figure 3.19. This storm had a maximum deep water hourly significant wave height of 3.6 m and maximum wind speed was around 17 m/s. According to the extreme wave analysis, this storm is found to be approximately a 5-Year RP storm. The difference between a 5-Year RP storm and a 100-Year RP storm being small (Table 3.2), and this storm being a frequently occurring one, made this storm eligible for modeling of historical storm conditions.

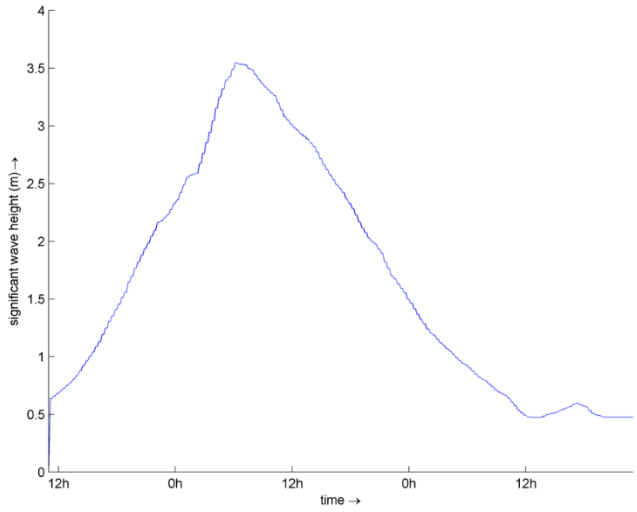



Figure 3.18 Wave Time Series of the January 6$^{th}$, 2012 storm

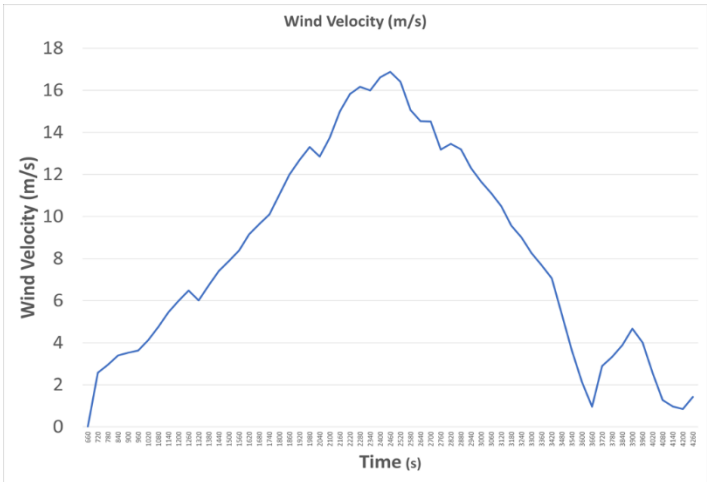



Figure 3.19 Wind Speed Time Series of January 6th, 2012 storm

To generate the synthetic storm of 100 year RP, the use of a triangular synthetic storm was decided on following similar studies from literature (Bocotti, 2000; ROM-1.0, 2009; Duo et al., 2020). The triangular form that the storm will have was decided by analyzing the shapes of the annual maxima storms of the region since there are both isosceles triangular and random triangular storms available in the literature. To analyze this, the hours where the maximum hourly significant wave heights of annual maxima storms were determined, and a threshold of 1.5 m wave height was applied before and after these maximum hours to extract storms. When the storms are aligned with respect to the hour with maximum significant wave height (Figure 3.20), it was seen that the peak moments nearly happen mid-storm, which indicated the possibility of using an isosceles triangular synthetic storm.

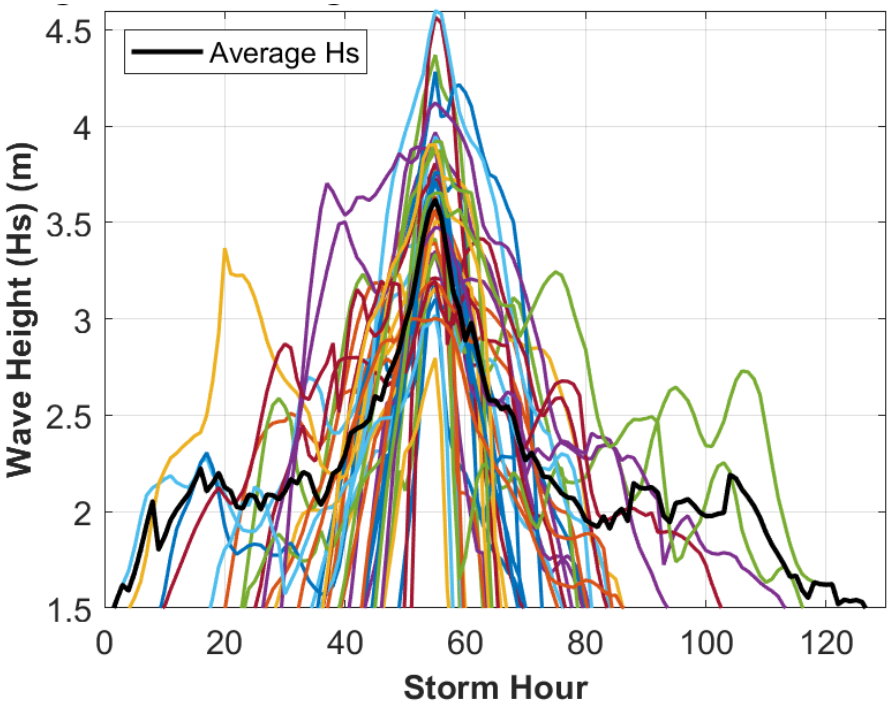



Figure 3.20 The Maximum Storms of Every Year with hours of maximum hourly significant wave height aligned

Thus, a triangular storm record (Figure 3.21) with the 100-year RP significant wave height as its peak value is generated, and hourly wave height data is obtained. The average of the durations of the storms that caused the annual maximum waves is used for the duration of the synthetic storm. The periods for the generated storm wave heights were obtained using the calculated steepness and the direction of this storm is assumed to be constant from the most critical direction which is southwest.

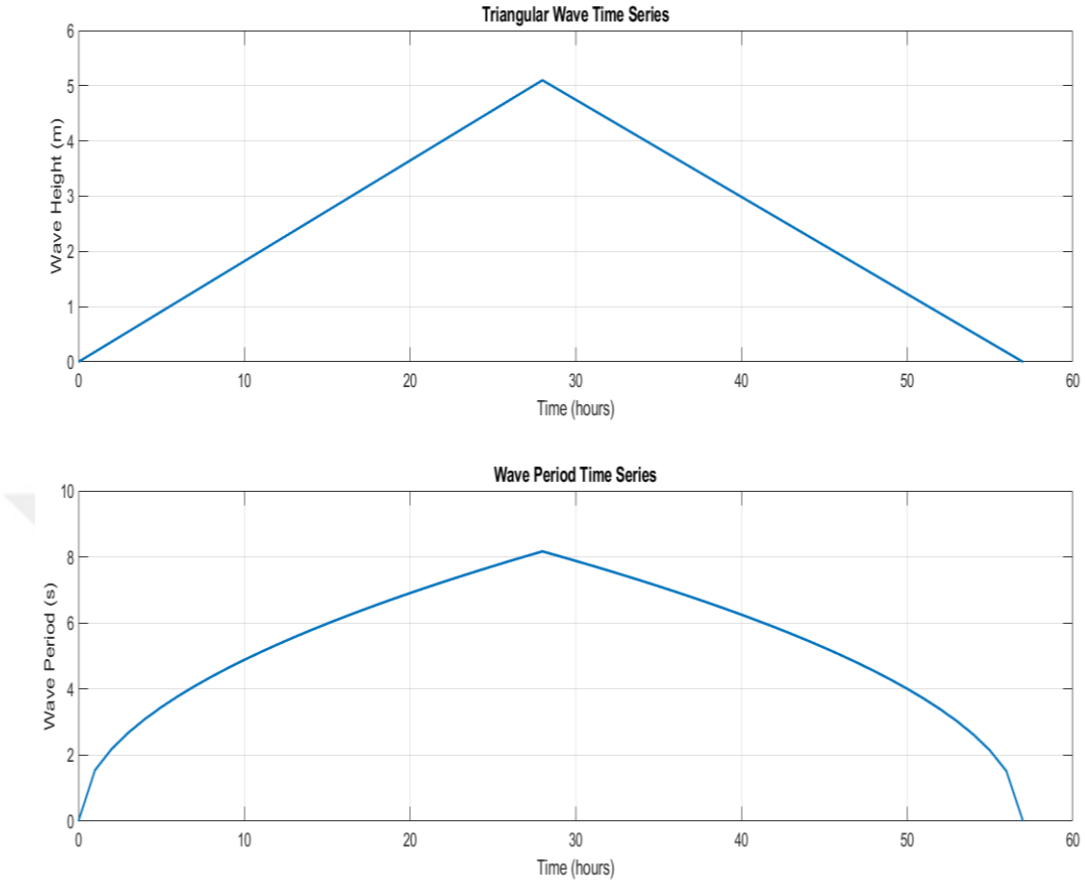



Figure 3.21 Time Series of Wave Height and Period of the Synthetic Storm

The next step would be the generate wind data that create these waves. For this, the Sverdruv Munk Bretschneider (SMB) method is used. The SMB approach is a semi-empirical technique utilized for estimating the significant height of waves, using the wind speed and the fetch length with Equation 1 (Aisjah et al., 2016). Here, the method is used inversely to obtain the wind speeds from the inserted wave heights from the triangular time series. The wind series obtained is shown in Figure 3.22.

$$\frac{gH_{1/3}}{U_{10}^2} = 0.3(1 - (1 + 0.004(\frac{gF}{U_{10}^2})^{1/2})^{-2}) \quad (1)$$

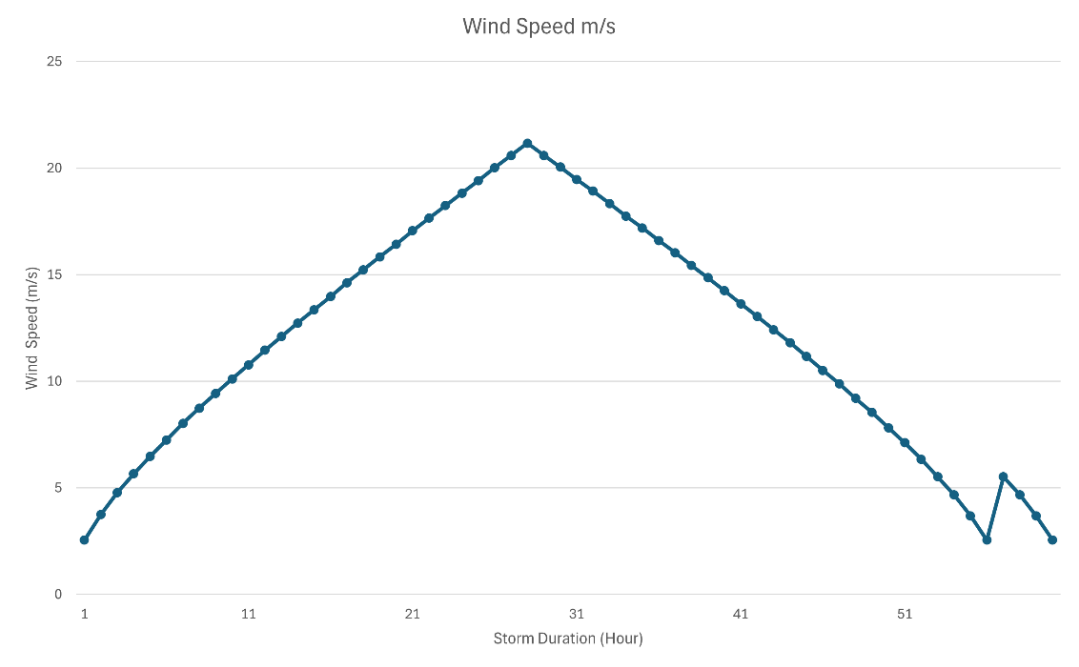



Figure 3.22 Wind Time Series obtained from the Synthetic Triangular Wave Time Series

In the end, a synthetic storm which is 60 hour long, with a maximum hourly significant wave height of 5.1 m, peak period of 8.2 s is obtained from the southwest direction.

### 3.3.3.3 Model Setup

Out of the various modules Delft3D provides, WAVE and FLOW modules are coupled to model the storms in this study. The FLOW module models the hydrodynamics of water systems. It operates based on physical processes such as tides, wind and pressure gradients to compute water levels and flow velocities. The WAVE module simulates waves, including generation, propagation, and transformation in coastal to offshore regions. It runs off the SWAN (Simulating WAves Nearshore) model. The modules are coupled to allow data exchange between the time steps for the computations like water level. SYM-5 DEM which also includes bathymetry is used for both modules.

- **WAVE DOMAIN**

The domain for the WAVE model consists of 4 domains nested into each other as the model area was kept large to capture the surge growth as much as the computational efficiency allows. The domains had 125 m, 25 m, and 5 m grid sizes. The wave boundary condition, which are the wave time series, was given from the southwest edge of the largest domain, constant through the edge. Smallest grid size is based on the available DEM resolution which is 5 m. Therefore, there was not much flexibility in the time step selection and an optimization was not possible. The time step that satisfied the Courant number Delft3D allows was 0.6 s.

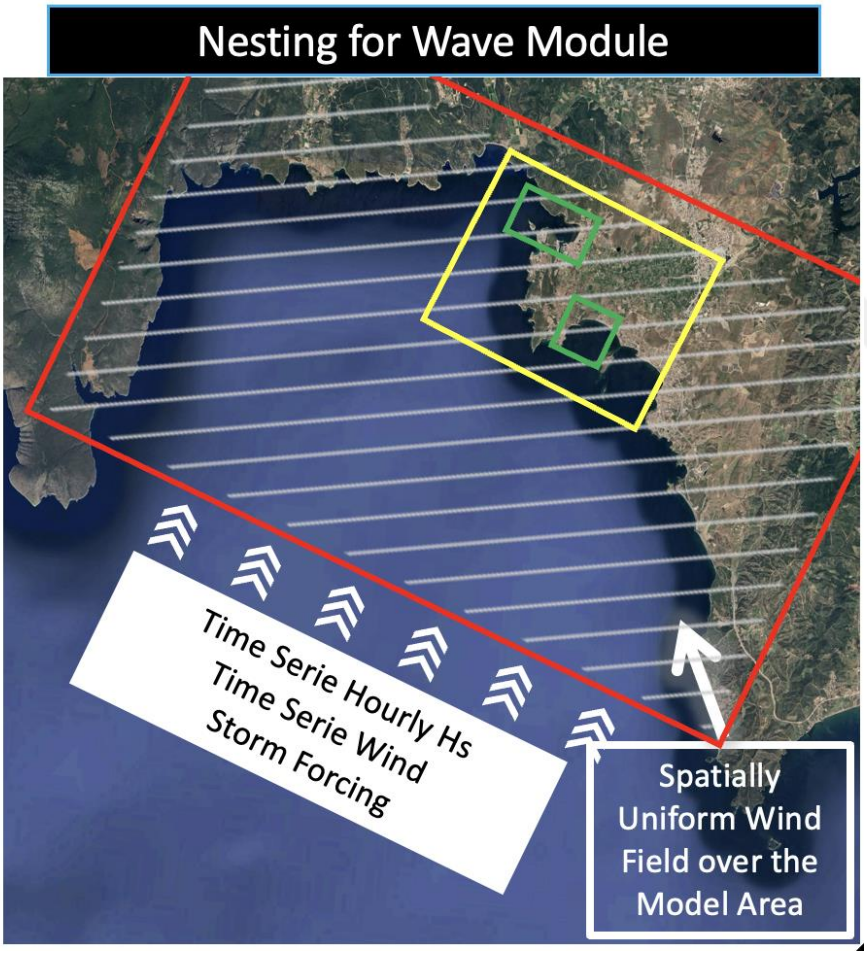



Figure 3.23 Computational Domain of Wave Module (Google Earth, 2024)

For the model, a circular directional space was used with 36 directions. The frequency space was from 0.05 Hz to 1 Hz with 24 partitions. The computation was done in a stationary mode since at this scale, non-stationary computation has no significant contribution. The coupling interval, where the computation results from the wave module is transferred to flow module, was selected as 20 minutes.

- **FLOW DOMAIN**

For flow computations, again four domains are used (Figure 3.24). The difference with the flow module is that sub-domains are not nested into each other but connected through grid points like puzzle pieces. The resolutions of the domains are the same as the wave domains, 125 m, 25 m, and 5 m. For the boundary conditions, the southwest boundary is provided with a water level time series, and the side boundaries are assigned as Neumann-type boundaries where the water flow is allowed. The same time step of 0.6 s was used as Delft3D does not allow different time increments when two modules are coupled. The physical parameters which include the hydrodynamic constants and wind drag coefficients were kept at their default values. After further evaluation of the computational domains, it was decided that the domain is too small to produce the realistic surge height value. Moreover, the computational and temporal limitations made it impossible to increase the size of the largest domain. Thus, water level data of the storm from Jan 6$^{th}$, 2012, is used as the input of flow boundary, both for the historical storm and the synthetic storm. Since there is no way to produce a synthetic surge level time series and since the storms are not so distinct in intensity, the use of the water level data of the historic storm for the generated storm was found to be appropriate. To obtain the water level increase during this storm, the Global sea level change time series from 1950 to 2050 derived from reanalysis and high-resolution CMIP6 climate projections (Copernicus Climate Change Service, 2022) database is used. Using the data point of this database at 38.0°N, 26.75°E given in Figure 3.25, the water level time series given in Figure 3.26 was obtained and used for the water level boundary condition.

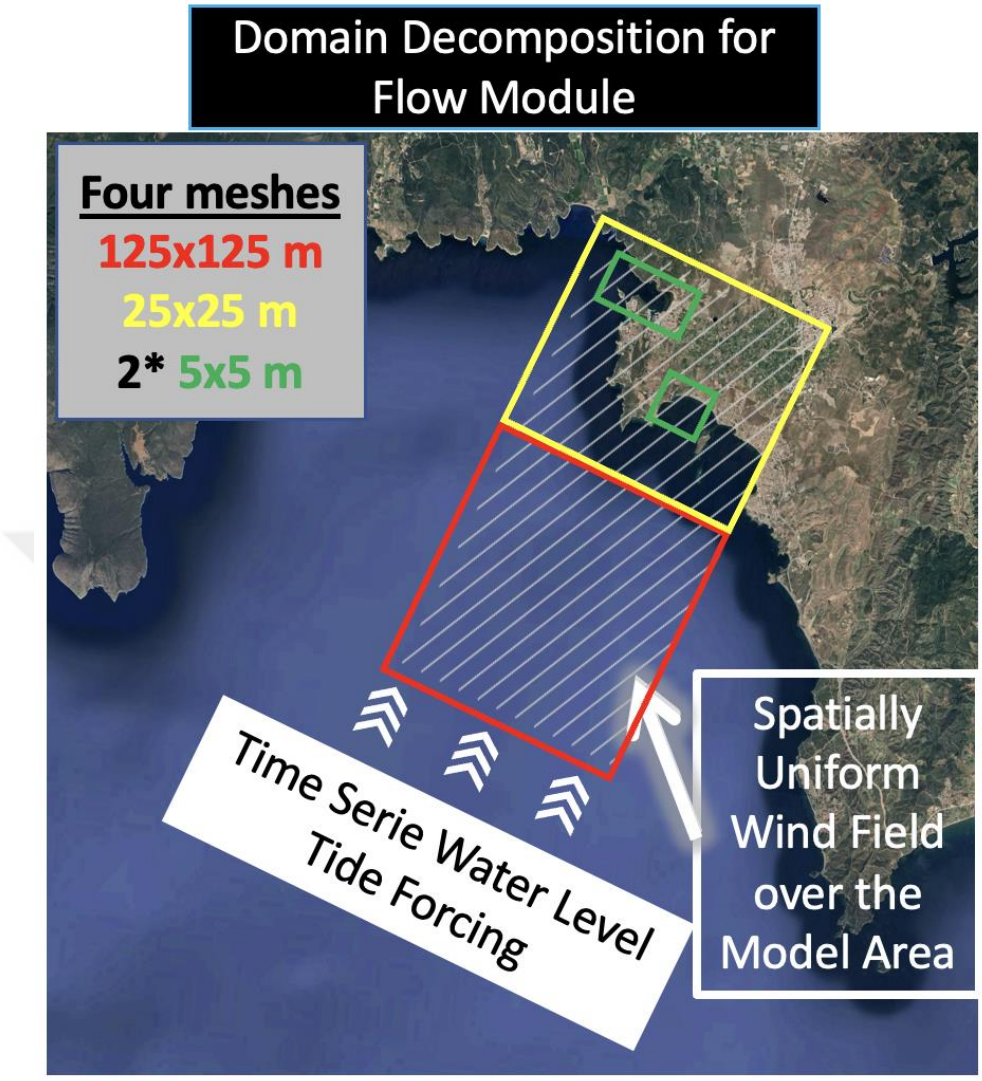



Figure 3.24 Computational meshes of Flow Module (Google Earth, 2024)

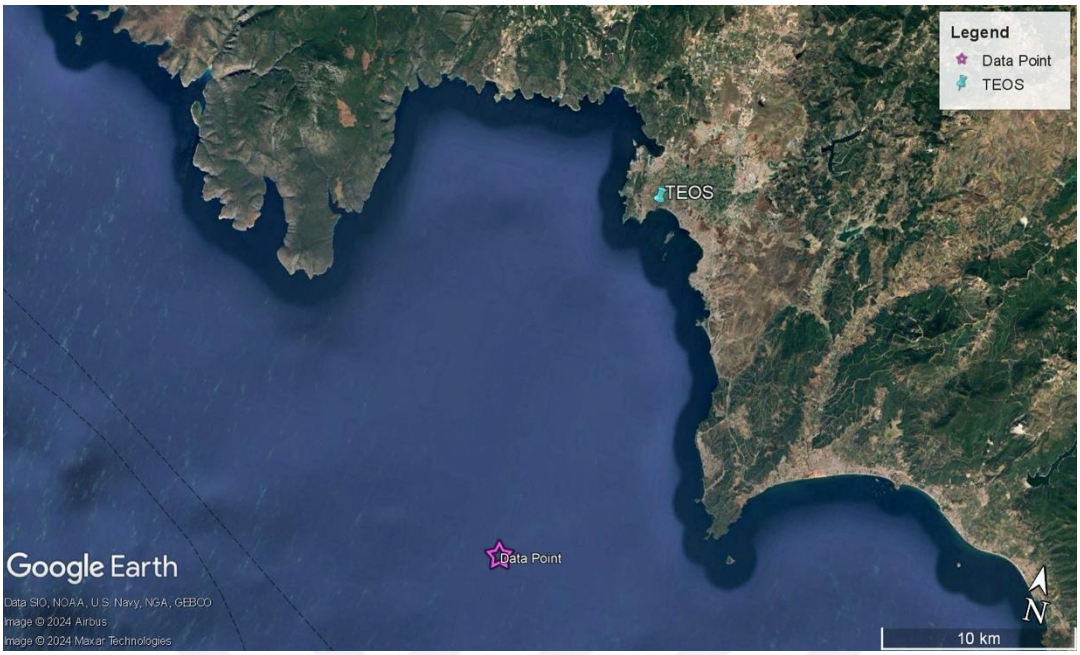



Figure 3.25 ERA5 Data Point for Water and Surge Level (Google Earth, 2024)

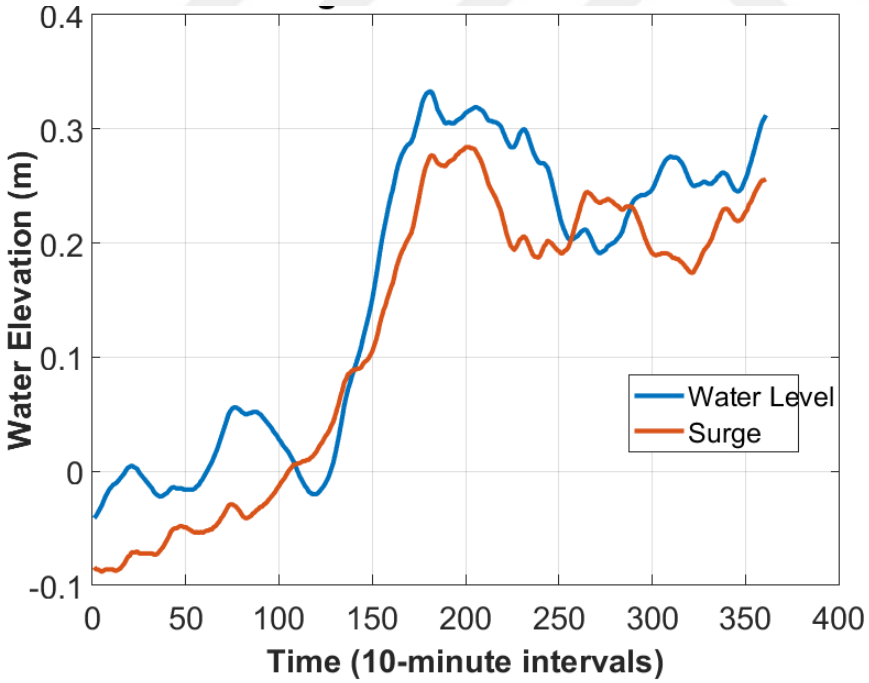



Figure 3.26 Water level increase during January 6th ,2012 storm

Using the historical 5-year RP storm, it was aimed to observe the episodic and frequent flooding of the heritage area, which might pose more danger when compared to an extreme event and what this storm will be able to risk in the future under sea level rise scenarios. Then using the 100-year RP synthetic storm, it was aimed to observe the flood extent under extreme conditions in the future where the surge height and wave effects are left to the performance of the hydrodynamic model rather than direct numbers from existing databases.

### 3.4 Vulnerability Assessment by CVI

The desk-based method used for the vulnerability assessment of heritage sites against flooding is the CVI (SLR) model by Özyurt (2007). This rapid vulnerability indicator model has been recognized by national and international studies. It quickly uses certain parameters to calculate a vulnerability value out of 5 against sea level rise. The vulnerability classification based on the value of the CVI (SLR) index is shown in Figure 3.27.

Very low vulnerability: 1≤CVI (SLR) <1.5
Low vulnerability: 1.5≤CVI (SLR) <2.5
Moderate vulnerability: 2.5≤CVI (SLR) <3.5
High vulnerability: 3.5≤CVI (SLR) <4.5
Very high vulnerability: 4.5≤CVI (SLR) ≤5

Figure 3.27 Vulnerability Classification based on CVI(SLR) (Özyurt, 2007)

The model takes into account human-based impacts together with physical impacts and employs 5 modules specific for 5 different impacts. The CVI of the impact is calculated performing a weighted sum approach using Equation 2.

$$CVI_{impact} = \frac{(0.5 * \sum_1^n PP_n * R_n) + (0.5 * \sum_1^m HP_m * R_m)}{CVI_{leastvulnerable}} \quad (2)$$

where PP is physical parameters, HP is human influence parameters, R is corresponding vulnerability range of the parameter, $CVI_{leastvulnerable}$ the value of the summation of the parameters for the least vulnerable case of the given impact.

When entered the required parameter values, the model matrix (Figure 3.28) calculates the vulnerability for each module and provides an overall vulnerability index.

| Impact | Physical Parameters | | | | | | | Human Influence Parameters | | | | | | | Impact Total | CVI impact |
|---|---|---|---|---|---|---|---|---|---|---|---|---|---|---|---|---|
| | Parameter | 1 | 2 | 3 | 4 | 5 | Total | Parameter | 1 | 2 | 3 | 4 | 5 | Total | | |
| 1. Coastal Erosion | P1.1 Rate of Sea Level Rise | 0 | 0 | 0 | 0 | 0 | 0 | H1.1 Reduction of Sediment Supply | 0 | 0 | 0 | 0 | 0 | 0 | | |
| | P1.2 Geomorpholgy | 0 | 0 | 0 | 0 | 0 | 0 | H1.2 River Flow Regulation | 0 | 0 | 0 | 0 | 0 | 0 | | |
| | P1.3 Coastal Slope | 0 | 0 | 0 | 0 | 0 | 0 | H1.3 Engineered Frontage | 0 | 0 | 0 | 0 | 0 | 0 | | |
| | P1.4 $H_{1/3}$ | 0 | 0 | 0 | 0 | 0 | 0 | H1.4 Natural Protection Degradation | 0 | 0 | 0 | 0 | 0 | 0 | | |
| | P1.5 Sediment Budget | 0 | 0 | 0 | 0 | 0 | 0 | H1.5 Coastal Protection Structures | 0 | 0 | 0 | 0 | 0 | 0 | | |
| | P1.6 Tidal Range | 0 | 0 | 0 | 0 | 0 | 0 | | | | | | | | | |
| | TOTAL | 0 | 0 | 0 | 0 | 0 | 0 | TOTAL | 0 | 0 | 0 | 0 | 0 | 0 | 0 | 0 |
| 2. Flooding due to Storm Surge | P2.1 Rate of Sea Level Rise | 0 | 0 | 0 | 0 | 0 | 0 | H2.1 Engineered Frontage | 0 | 0 | 0 | 0 | 0 | 0 | | |
| | P2.2 Coastal Slope | 0 | 0 | 0 | 0 | 0 | 0 | H2.2 Natural Protection Degradation | 0 | 0 | 0 | 0 | 0 | 0 | | |
| | P2.3 $H_{1/3}$ | 0 | 0 | 0 | 0 | 0 | 0 | H2.3 Coastal Protection Structures | 0 | 0 | 0 | 0 | 0 | 0 | | |
| | P2.4 Tidal Range | 0 | 0 | 0 | 0 | 0 | 0 | | | | | | | | | |
| | TOTAL | 0 | 0 | 0 | 0 | 0 | 0 | TOTAL | 0 | 0 | 0 | 0 | 0 | 0 | 0 | 0 |
| 3. Inundation | P3.1 Rate of Sea Level Rise | 0 | 0 | 0 | 0 | 0 | 0 | H3.1 Natural Protection Degradation | 0 | 0 | 0 | 0 | 0 | 0 | | |
| | P3.2 Coastal Slope | 0 | 0 | 0 | 0 | 0 | 0 | H3.2 Coastal Protection Structures | 0 | 0 | 0 | 0 | 0 | 0 | | |
| | P3.3 Tidal Range | 0 | 0 | 0 | 0 | 0 | 0 | | | | | | | | | |
| | TOTAL | 0 | 0 | 0 | 0 | 0 | 0 | TOTAL | 0 | 0 | 0 | 0 | 0 | 0 | 0 | 0 |
| 4. Salt Water Intrusion to Groundwater Resources | P4.1 Rate of Sea Level Rise | 0 | 0 | 0 | 0 | 0 | 0 | H4.1 Groundwater consumption | 0 | 0 | 0 | 0 | 0 | 0 | | |
| | P4.2 Proximity to Coast | 0 | 0 | 0 | 0 | 0 | 0 | H4.2 Land Use Pattern | 0 | 0 | 0 | 0 | 0 | 0 | | |
| | P4.3 Type of Aquifer | 0 | 0 | 0 | 0 | 0 | 0 | | | | | | | | | |
| | P4.4 Hydraulic Conductivity | 0 | 0 | 0 | 0 | 0 | 0 | | | | | | | | | |
| | P4.5 Depth to Groundwater Level Above Sea | 0 | 0 | 0 | 0 | 0 | 0 | | | | | | | | | |
| | TOTAL | 0 | 0 | 0 | 0 | 0 | 0 | TOTAL | 0 | 0 | 0 | 0 | 0 | 0 | 0 | 0 |
| 5. Salt Water Intrusion to River/Estuary | P5.1 Rate of Sea Level Rise | 0 | 0 | 0 | 0 | 0 | 0 | H5.1 River Flow Regulation | 0 | 0 | 0 | 0 | 0 | 0 | | |
| | P5.2 Tidal Range | 0 | 0 | 0 | 0 | 0 | 0 | H5.2 Engineered Frontage | 0 | 0 | 0 | 0 | 0 | 0 | | |
| | P5.3 Water Depth at Downstream | 0 | 0 | 0 | 0 | 0 | 0 | H5.3 Land Use Pattern | 0 | 0 | 0 | 0 | 0 | 0 | | |
| | P5.4 Discharge | 0 | 0 | 0 | 0 | 0 | 0 | | | | | | | | | |
| | TOTAL | 0 | 0 | 0 | 0 | 0 | 0 | TOTAL | 0 | 0 | 0 | 0 | 0 | 0 | 0 | 0 |

| | | |
|---|---|---|
| CVI(SLR)-1 | 0 | 0 |
| CVI(SLR)-2 | 0 | 0 |
| CVI(SLR)-3 | 0 | 0 |

Figure 3.28 The CVI (SLR) Vulnerability Matrix (Özyurt, 2007)

The values entered into the matrix are obtained by classifying the value of the relevant parameter for the place where the vulnerability calculation is performed. This study focuses on the vulnerability against flooding and inundation of the coastal area. Therefore, only the “Flooding due to Storm Surges” and “Inundation” modules are used.

Table 3.3 CVI Parameters of Inundation and Storm Surge Impacts (Özyurt, 2007)

| Impact | *Physical Parameters* | *Human Influence Parameters* |
|---|---|---|
| Flooding due to Storm Surge | 1. Rate of Sea Level Rise<br>2. Coastal Slope<br>3. Extreme Water Level (100 y RP)<br>4. Tidal Range | 5. Engineered Frontage<br>6. Natural Protection Degradation<br>7. Coastal Protection Structures |
| Inundation | 1. Rate of Sea Level Rise<br>2. Coastal Slope<br>3. Tidal Range | 4. Natural Protection Degradation<br>5. Coastal Protection Structures |

Table 3.3 shows the physical and human influence parameters these two modules use. The values of these parameters for the selected study sites are assigned a class that indicates how the given parameter value affects the vulnerability.

Table 3.4 shows the class ranges presented by (Özyurt, 2007) for these parameters.

Table 3.4 Class Ranges of the Parameters Affecting Inundation and Storm Surge Flood Impacts (Özyurt, 2007)

| | *Range* | | | | |
|---|---|---|---|---|---|
| | *Very Low* | *Low* | *Moderate* | *High* | *Very High* |
| Parameters | *1* | *2* | *3* | *4* | *5* |
| Rate of SLR mm/year | <1 | 1-2 | 2-5 | 5-7 | 7-9 and over |
| Coastal Slope | <1/10 | 1/10-1/20 | 1/20-1/30 | 1/30-1/50 | 1/50-1/100 |
| Significant Wave Height (m) | <0.5 | 0.5-3.0 | 3.0-6.0 | 6.0-8.0 | >8.0 |
| Tidal Range (m) | >6 | 4.0-6.0 | 2.0-4.0 | 0.5-2.0 | <0.5 |
| Engineered Frontage | <5% | 5-20% | 20-30% | 30-50% | >50% |
| Natural Protection Degradation | <20% | 20-40% | 40-60% | 60-80% | >80% |
| Coastal Protection Structures | >50% | 30-50% | 20-30% | 5-20% | <5% |

After determining the values parameter classification gives, the matrix is operated to obtain the CVI against flooding due to storm surge and inundation.

# CHAPTER 4

# RESULTS

## 4.1 Sea Level Rise and Extreme Water Level Projections at Turkish Coasts

The analysis of the extreme water level projections from the LISCOAST and Kirezci datasets yielded differing results. Looking at both 2050 (Table 4.1) and 2100 (Table 4.2) prediction ranges for the Turkish coasts, the LISCOAST dataset predicts significantly larger values in both RCP4.5 and RCP8.5 scenarios. For both scenarios, this difference is most evident in the lower limits for 2050, as LISCOAST predictions are around twice as high as Kirezci's. By 2100, the difference at these lower limits diminishes, and the two dataset predictions converge, although there is still a significant difference.

Table 4.1 Extreme Water Level Ranges at Turkish Coasts for 2050

| Projection | *RCP 4.5* | *RCP 8.5* |
|---|---|---|
| LISCOAST (Vousdoukas et al., 2018) | 0.81-1.37 | 0.9-1.46 |
| Kirezci et al. (2022) | 0.41-1.13 | 0.44-1.16 |

Table 4.2 Extreme Water Level Ranges at Turkish Coasts for 2100

| Projection | *RCP 4.5* | *RCP 8.5* |
|---|---|---|
| LISCOAST (Vousdoukas et al., 2018) | 1.09-1.66 | 1.41-1.94 |
| Kirezci et al. (2022) | 0.66-1.39 | 0.85-1.6 |

It should also be noted that the LISCOAST dataset provides a broader range of predictions across all years and scenarios, although the values it offers are larger. Moreover, predictions of both datasets are not much affected by the scenario change

in 2050, as Table 4.1 shows that the scenario change from RCP 4.5 to 8.5 affects the intervals by less than 10 cm.

In 2100, the difference between the scenarios and between the predictions provided by the two datasets increases dramatically. In 2100, the gap between the scenarios and the predictions provided by the two datasets will increase dramatically, so much so that Kirezci's maximum prediction in the RCP 8.5 scenario is almost equal to LISCOAST's maximum in the RCP4.5 scenario. Looking at the 2050 and 2100 predictions for the RCP8.5 scenario, the LISCOAST dataset shows a range change such that the upper limit in 2050 is the lower limit in 2100. In Kirezci, even though the lower limit in 2100 is double that of 2050, the range does not shift that much, and they still share a large common portion. The Discussions chapter will address the potential factors contributing to the sensitivity of the predictions from the two datasets to various scenarios and years and the reasons behind the mentioned differences.

Apart from the size of the estimates provided by these two datasets, their distribution along the country's coasts was also analyzed. The ranges given in Figure 4.1 are evaluated in three classes of equal intervals. The upper interval is designated as high, the middle as medium and the lower interval as low values of EWL in meters.

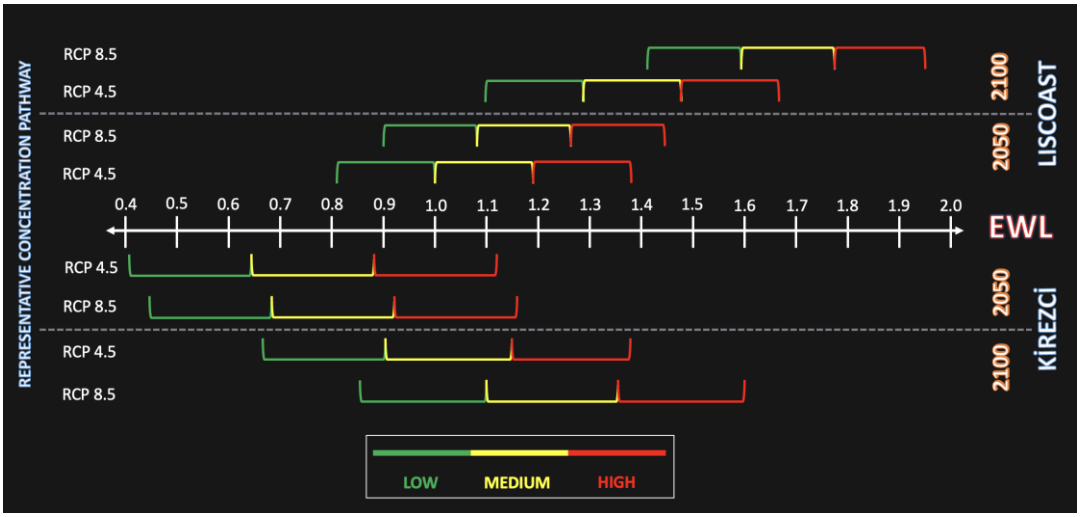



Figure 4.1 EWL (m) ranges for Turkish Coasts

Using this classification, the spatial distribution of high, medium and low EWL projections are analyzed. Figure 4.2 and Figure 4.3 show the distribution of Kirezci database and Figure 4.4 and Figure 4.5 show the distribution of LISCOAST database, for 2050 and 2100 respectively. In the figures, the distributions for RCP4.5 and RCP8.5 are presented together using a bivariate symbology.

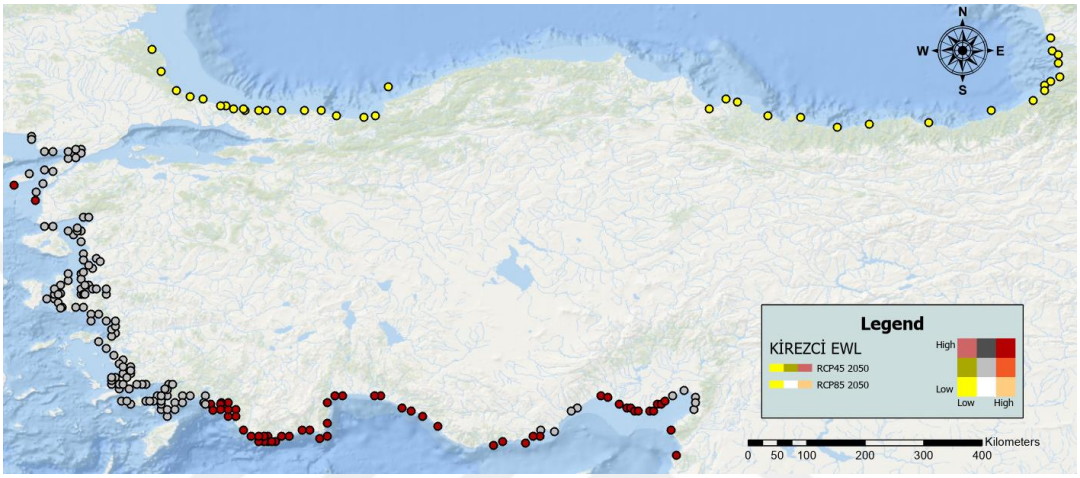



Figure 4.2 EWL Prediction Points and Classifications for 2050 from Kirezci

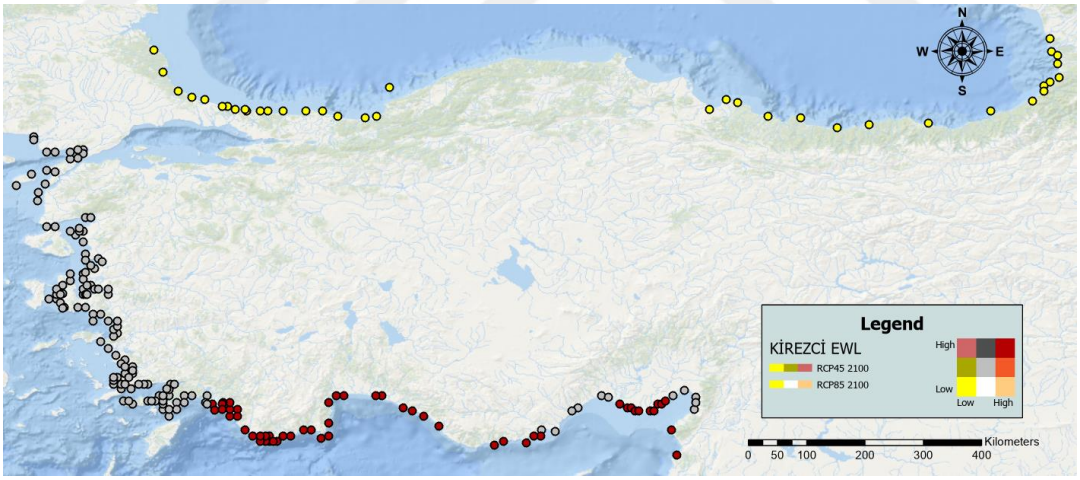



Figure 4.3 EWL Prediction Points and Classifications for 2100 from Kirezci

According to Figure 4.2 and Figure 4.4 the lowest EWL will be experienced at the Black Sea coasts of Türkiye, the medium EWL values at the Aegean coasts and some regional parts of eastern Mediterranean, and the highest EWL values will be experienced at the west, central and some parts of the east Mediterranean. The data

points being of the diagonal colours indicates that none of the points change their class when scenario is switched from 4.5 to 8.5.

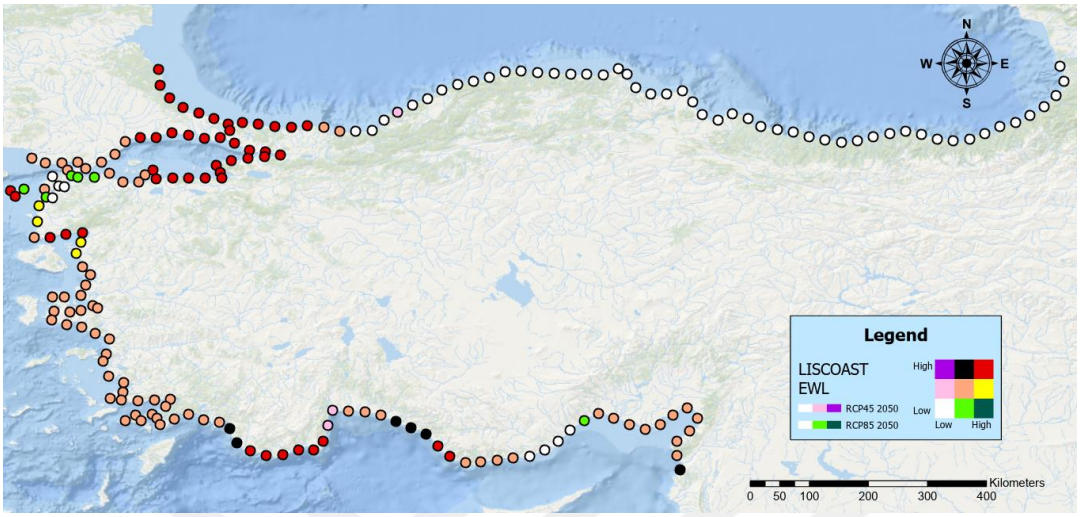



Figure 4.4 EWL Prediction Points and Classifications for 2050 from LISCOAST

With the same method, the values from LISCOAST database are mapped as well. The distribution with LISCOAST predictions is not as smoothly distributed as Kirezci's along the geographical regions of Türkiye. However, Black Sea region having the lowest levels and Aegean coasts having the medium levels valid for this database too. The high EWLs are along the coasts of Marmara Region, which was not available in the Kirezci database. The Mediterranean coasts are showing high variance. Even without checking the changes between scenarios, low, medium and high values are expected in the Mediterranean. When the predictions are switched from RCP4.5 to RCP8.5, the classification along the Black Sea and Aegean coasts remain the same. However, in Marmara Region, at the entrance of Çanakkale Strait, the yellow data points changed classification from medium to high, meaning they moved from the middle one-third to the upper one and green points moved from low to medium.

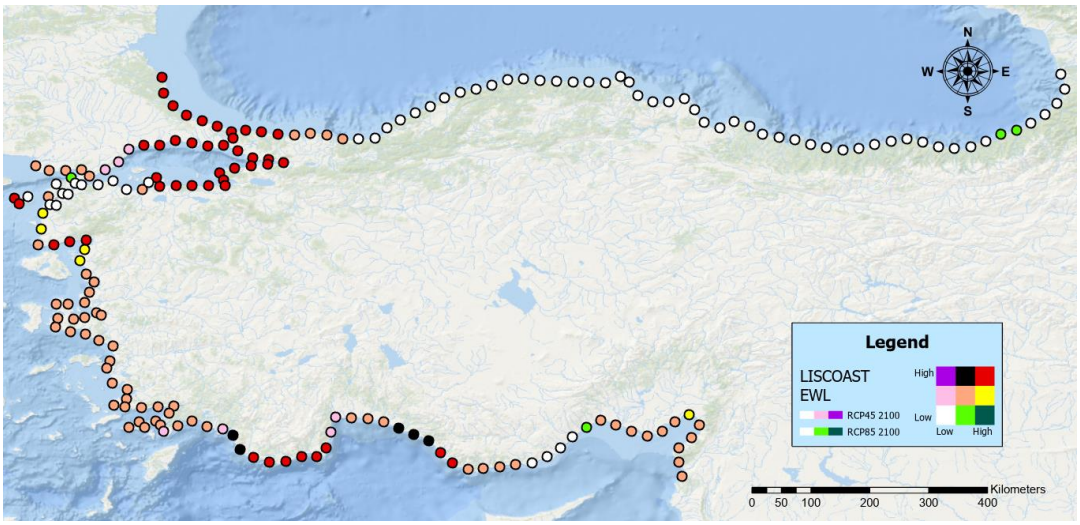



Figure 4.5 EWL Prediction Points and Classifications for 2100 from LISCOAST

## 4.2 Study Sites

Based on the explained criteria given in Section 3.2, the Ancient Cities of Soli-Pompeipolis, Anemurium, Aleksandria Troas, and Teos, all being harbor cities under first-level conservation, are selected to be studied. How the criterion-specific vulnerability is defined is explained in the methodology chapter. The detailed scanning of the databases revealed that there don't appear to be heritage sites that qualify as “vulnerable” for the specified criteria all at the same time, which is having identified uncovered remains with a high degree of conservation situated in a low-elevation area with a lengthy shoreline that is subject to strong storms. Thus, sites that possibly satisfy the greatest number of criteria were chosen. For instance, the Ancient City of Anemurium is located at a fast-elevating hillside, not being vulnerable according to the elevation criteria. However, having totally unearthed remains close to the shoreline which is 11 km long and totally open to storms made this site eligible to study. Similarly, the ancient cities of Aleksandria Troas and Teos were selected because Aleksandria Troas is located at a very storm-prone location and has a conserved lake close to the shoreline and Teos has mostly under 5 m of elevation, although both cities don’t have much remains unearthed close to their shores.

❖ ***Ancient City of Aleksandria Troas***

The ancient city of Alexandria Troas is in the Ezine district of Çanakkale. Located southeast of Bozcaada on the Aegean Sea coast. The ancient city dates to 310 BC. Serving as the main port of the region, the city is one of the largest ancient cities in Anatolia (Figure 4.6 A). Baths, the theatre building, the palace, the temple, and the harbour (Figure 4.6 B) are among the most important ruins.

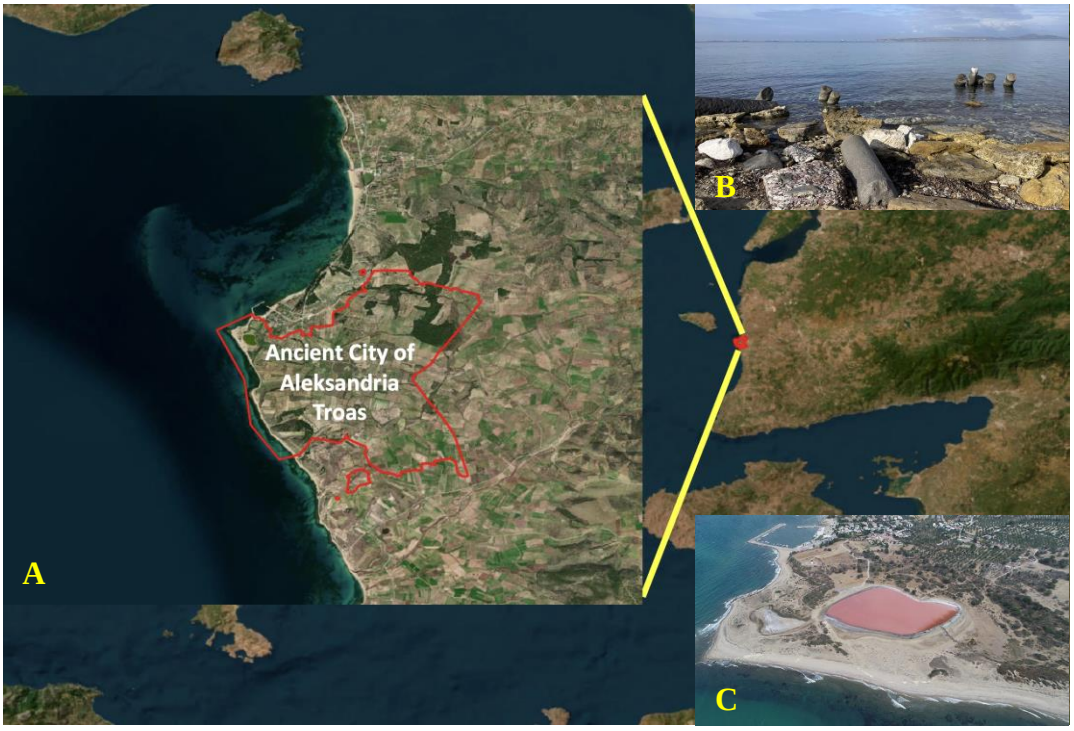



Figure 4.6 The Ancient City of Aleksandria Troas (A: The heritage site borders, B: Ancient Harbour Ruins, C: The Preserved Pink Lake behind the ancient harbour) (Google Earth, 2024)

The city has 2.7 km of coastline, and its coast is almost entirely made up of sandy beaches. Behind the ancient city is the pink lake (Figure 4.6 C), which stands out for its natural beauty. Right next to the pink lake, there is a lagoon-like formation, which can be seen from Google Earth photos that periodically fills up and dries up again.

❖ ***Ancient City of Teos***

The Ancient City of Teos is in the Seferihisar district of Izmir. It was founded on the Isthmos peninsula within the borders of Sığacık (Figure 4.7 A). It has two harbors, one in the north and one in the peninsula's south. In the northern part, there are modern Sığacık and Teos marina today, in the south, the ancient harbor still exists but has not totally been brought to the surface (Figure 4.7 B-C).




Figure 4.7 The Ancient City of Teos (A: The heritage site borders and Sığacık, B: The Ancient Breakwater of the South Harbor, C: A Photo from the Breakwater of the South Harbor) (Google Earth, 2024)

According to the information from the excavation group during the field visit to Teos, the city was founded on this peninsula, on the plain formed by the alluvium carried by the rivers Yassıçay, Pınarlı and Kantarcı, flowing into the sea here. This delta formed by the rivers joined the mainland with the piece of land to the west of the city, an island at the time, and formed the present peninsula. This explains why the altitude of the city is so low. The portion of the ancient city trapped in the modern Sığacık today is now designated as an "urban conservation area" by the Ministry of Culture and Tourism. The city also borders a nature park to the west, which is a first-degree natural conservation area, and Sazlıgöl Tumulus on the east which is another

first-degree conservation area. The city has 1 km of shoreline consisting of sandy beaches.

- ***Ancient City of Anemurium***

Located in Anamur district of Mersin and giving its name to the district, Anemurium was an important trade center in its heyday as a part of the Commagene Kingdom. There are various churches, baths, and aqueduct structures still standing in the city.




Figure 4.8 The Ancient City of Anemurium (Google Earth, 2024)

The city is founded on a 2 km long sandy beach and on the slope rising behind it, today known as the Anamur Cape. According to Russell, (1976), the name Anemurium means "Windy Place", which supports the idea behind the selection of this site, which is its predisposition to storms.

- ***Ancient City of Soli-Pompeipolis***

The ancient city of Soli-Pompeipolis is in the Mezitli district of Mersin. The history of the city dates to the 6$^{th}$ century BC. Colonnaded Street, Soli Mound, and Ancient Harbor are the most important remains. The city had a unique harbor design with twin breakwaters (Figure 4.10), which are covered by the sediment and under the

current ground at the moment, however, excavations have been performed by the archaeologists at the west breakwater (Figure 4.9 A-C).




Figure 4.9 The Ancient City of Soli-Pompeipolis (A: Remains of the west breakwater, B: Heritage Site Borders, C: Excavations of the breakwater) (Google Earth, 2024)

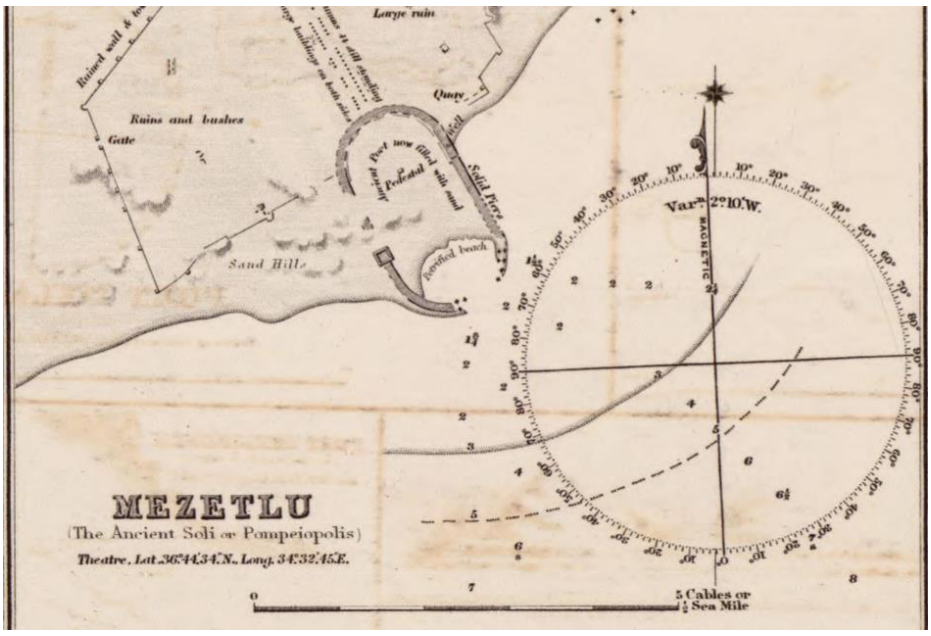



Figure 4.10 Map of the Ancient Harbour and Breakwaters of Soli-Pompeipolis (Great Britain Hydrographic Office, 1885).

## 4.3 CVI-SLR Analyses

The CVI-SLR analysis is performed for only the inundation and storm surge flooding under SSP5 scenario. Table 4.3 shows the inputs of the model.

Table 4.3 CVI-SLR Input Parameters for Flooding and Surge Impacts (Blue: Actual value of the parameter, Red: CVI Class of that value)

| Type of Travel | *Aleksandria Troas* | | *Soli-Pompeipolis* | | *Anemurium* | | *Teos* | |
|---|---|---|---|---|---|---|---|---|
| **Physical Parameters** | | | | | | | | |
| Rate of SLR (mm/yr) | 11 | **5** | 12 | **5** | 12 | **5** | 12 | **5** |
| Coastal Slope (degree) | 14.5 | **1** | 6.34 | **1** | 36.3 | **1** | 4.9 | **2** |
| 100 Yr. RP EWL (m) | 1.78 | **2** | 1.61 | **2** | 1.66 | **2** | 1.63 | **2** |
| Tidal Range (m) | 0.087 | **5** | 0.15 | **5** | 0.12 | **5** | 0.046 | **5** |
| **Human Influence Parameters** | | | | | | | | |
| Engineered Frontage (%) | 11.93 | **2** | 76.2 | **5** | 1.7 | **1** | 19.8 | **2** |
| Natural Protection Degradation (%) | 0 | **1** | 0 | **1** | 0.16 | **1** | 0 | **1** |
| Coastal Protection Structures (%) | 3.37 | **5** | 19.4 | **4** | 0 | **5** | 0 | **5** |

Table 4.3 CVI-SLR Input Parameters for Flooding and Surge Impacts (Blue: Actual value of the parameter, Red: CVI Class of that value)Table 4.3 reveals that the physical parameter values of the 4 sites are close to each other. For this reason, the physical parameter classes were found to be the same in Alexandria, Soli and Anemurium, while only one of them was found to be different in Teos. In human influence parameters, engineering frontage is the parameter that usually makes the difference between the areas.

Table 4.4 CVI-SLR Results (Vulnerability Indices out of 5)

| CVI-SLR Impact | ***Inundation*** | ***Flooding due to Storms*** |
|---|---|---|
| Aleksandria Troas | 3.4<br>Moderate Vuln. | 3<br>Moderate Vuln |
| Soli-Pompeipolis | 3.4<br>Moderate Vuln. | 3.43<br>Moderate Vuln. |
| Anemurium | 3.4<br>Moderate Vuln. | 2.86<br>Moderate Vuln. |
| Teos | 3.6<br>Moderate Vuln. | 3.14<br>Moderate Vuln. |

CVI-SLR results (Table 4.4) show that all 4 studied areas have medium vulnerability to both inundation and flooding due to storms. The most vulnerable area against inundation is the ancient city of Teos and the most vulnerable area against flooding due to storm surge is Soli-Pompeipolis.

## 4.4 Flood Maps

In this section, the flood maps and areal information on inundation/flooding will be presented. The results are given separately for each study site, the different methods, and the different DEM data used. The inundation maps are prepared only for 2100 whereas surge flooding maps are prepared for 2050 and 2100. On the inundation maps, SSP2 and SSP5 are presented together. For the surge flood maps, two datasets Kirezci and LISCOAST, and two scenarios RCP4.5 and 8.5 are presented on the same map, prepared for the years 2050 and 2100. Under the related headings, first, a table is given where the inundated and flooded area information is provided in square meters and percentages, and then the following figures showing the maps are presented.

### 4.4.1 Ancient City of Aleksandria Troas

For Aleksandria Troas, only available elevation model was GLO-30 of Copernicus. This 30 m resolution DEM model was used both for sBTM and eBTM application.

#### 4.4.1.1 sBTM

Aleksandria Troas loses 0.79% and 1.26% of land in the mid-way and the worst-case scenario, relatively. For predictions under extreme weather conditions, as expected, LISCOAST gives more flood area than the Kirezci database. Table 4.5 shows that LISCOAST gives 0.2% more flood area than Kirezci in the RCP4.5 scenario and 0.3% more in the RCP8.5 scenario for 2100. For the worst emission scenario, LISCOAST predicts that 1.9% of Alexandria Troas will be flooded. Alexandria Troas has a natural asset called the Pink Lake right on its shores. Figure 4.11-A shows that in the worst-case scenario of emissions, the lake would be lost to the sea. During extreme weather events, this intrusion is certain to occur in both 2050 and 2100. This mixing appears to be mostly from the shore on the ancient breakwater side of the lake. However, with the LISCOAST RCP8.5 scenario for 2050, seawater inflow from the south is also observed (Figure 4.11-B). This secondary seawater intrusion is observed in all scenarios except for the best-case scenario of Kirezci in 2100. As a result, even if the emission estimates do not follow the worst-case scenario, the lake will lose its structure by mixing with seawater during extreme weather events. For 2050, the change in the emission scenario does not change the flooded area much. Especially for Kirezci, this difference is as small as 0.02%, while in 2100 the scenario change causes a difference of 0.13% (Table 4.5). In the SSP2/RCP4.5 scenarios of LISCOAST, flooded areas for 2100 are twice as large as inundated areas (Table 4.5). In other words, in the RCP4.5 scenario, the area flooded by an extreme weather event in 2100 will be equal to the area lost to water level rise by 2100. In the RCP8.5 scenario, this doubling is not observed.

Table 4.5 Inundated and Flooded sBTM Areas of the Ancient City of Aleksandria Troas ($m^2$)

| | ***SSP2*** | ***SSP5*** |
|---|---|---|
| Area Inundated by 2100 | *53740.7* ***(0.79%)*** | *86204.9* ***(1.26%)*** |

| | ***LISCOAST*** | ***Kirezci*** | |
|---|---|---|---|
| *Area Flooded under EWL for 2050* | *102795.3* ***(1.51%)*** | *87460* ***(1.29%)*** | ***RCP4.5*** |
| | *108783.7* ***(1.6%)*** | *89311.9* ***(1.31%)*** | ***RCP8.5*** |
| *Area Flooded under EWL for 2100* | *115653.3* ***(1.7%)*** | *100906* ***(1.48%)*** | ***RCP4.5*** |
| | *129232* ***(1.9%)*** | *109232* ***(1.61%)*** | ***RCP8.5*** |

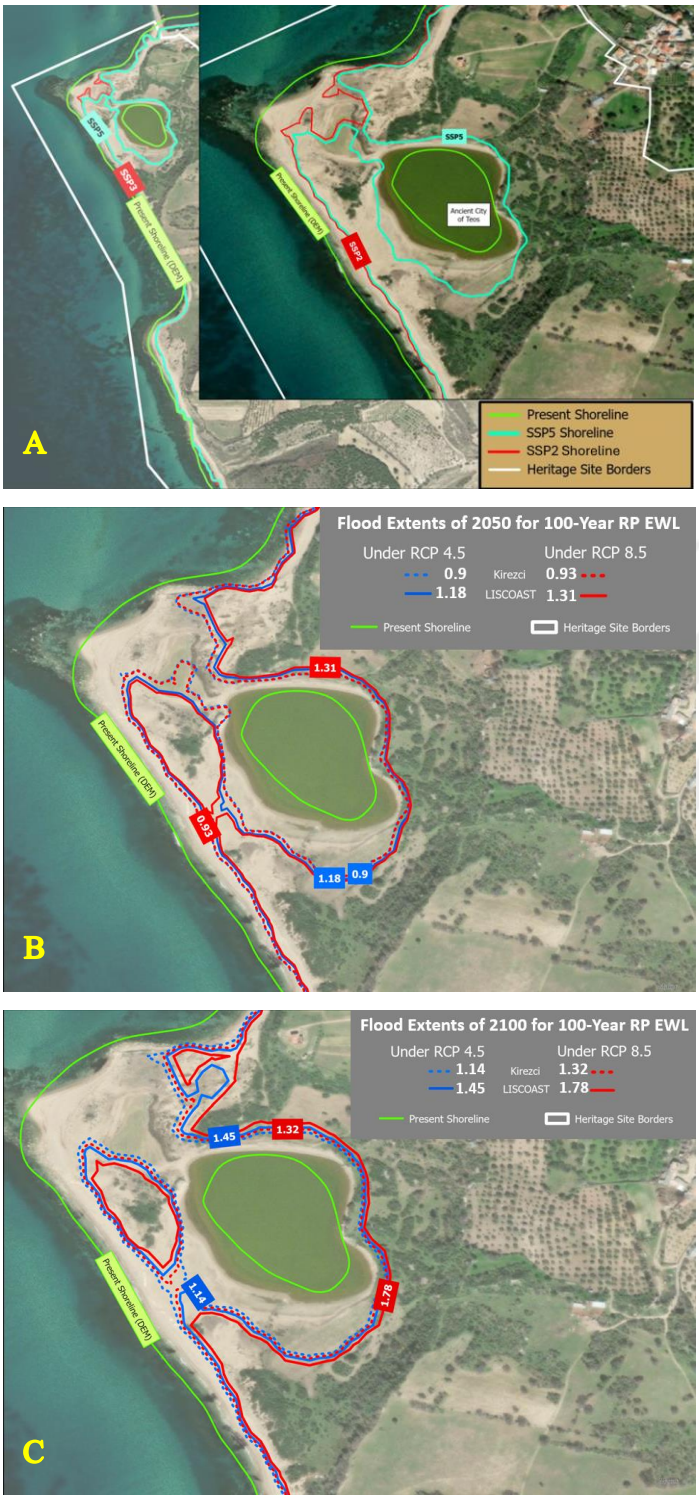



Figure 4.11 Aleksandria Troas sBTM Inundation and Flood Maps using GLO-30 (A: Inundation in 2100, B: Storm Surge Flooding in 2050, C: Storm Surge Flooding in 2100)

#### 4.4.1.2 eBTM

In the flood maps generated with eBTM, the flooded areas are shown with polygon layers consisting of pixels of the elevation model raster. These pixels are colored according to the inundation depth in that pixel. Since the polygons are shown together, the areas further inundated when the scenario or dataset is different can be understood from the different colour pixels. The colour notations are shown in the legend given on the figures. Looking at the maps provided by the eBTM method, agreement with the sBTM method is observed. Table 4.6 shows that the eBTM method found much larger flood areas. Similar results were obtained with sBTM in terms of water intrusion behavior. eBTM also found the mixing of Pink Lake with seawater and the paths of water intrusion in the same way. the only difference with sBTM is the inundated area information.

Table 4.6 Inundated and Flooded eBTM Areas of the Ancient City of Aleksandria Troas ($m^2$)

| | ***SSP2*** | ***SSP5*** | |
|---|---|---|---|
| Area Inundated by 2100 | *78007.25* ***(1.15%)*** | *112704.3* ***(1.66%)*** | |
| | ***LISCOAST*** | ***Kirezci*** | |
| *Area Flooded under EWL for 2050* | *122420.17* ***(1.8%)*** | *110321.85* ***(1.62%)*** | ***RCP4.5*** |
| | *127682.41* ***(1.88%)*** | *111464.38* ***(1.64%)*** | ***RCP8.5*** |
| *Area Flooded under EWL for 2100* | *130736.46* ***(1.92%)*** | *119023.43* ***(1.75%)*** | ***RCP4.5*** |
| | *145946.79* ***(2.15%)*** | *127654* ***(1.88%)*** | ***RCP8.5*** |

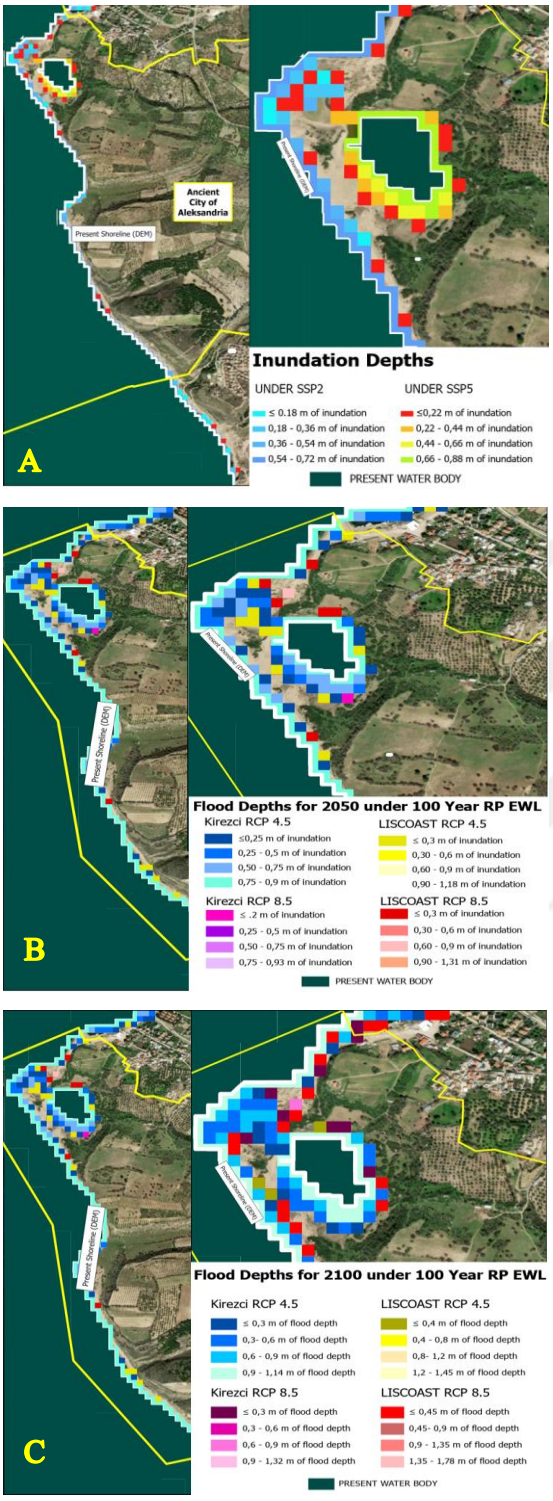



Figure 4.12 Aleksandria Troas eBTM Inundation and Flood Maps using UAV DSM (A: Inundation in 2100, B: Storm Surge Flooding in 2050, C: Storm Surge Flooding in 2100)

### 4.4.2 Ancient City of Anemurium

For the Ancient City of Anemurium, it was possible to obtain flood maps with both methods using both GLO-30 of Copernicus and the UAV-generated DSM. The original UAV model has a 5 cm resolution however a 1 m resolution raster is generated from it for ease of operation in ArcMap.

#### 4.4.2.1 sBTM

##### 4.4.2.1.1 GLO-30

In the sBTM model using GLO-30, the amount of permanently or temporarily inundated area varies between approximately 2.6% and 4.7%. In the values shown in Table 4.7, first, the difference in inundated areas between scenarios is noticeable. Changing the emission scenario increases the inundated area by 20%. Considering that Anemurium has a shoreline length of approximately 2 km, the new shoreline will be 25-30 m inland.

Table 4.7 Inundated and Flooded sBTM areas of Anemurium using GLO-30

| | ***SSP2*** | ***SSP5*** | |
|---|---|---|---|
| Area Inundated by 2100 | *53229* ***(2.59%)*** | *63672.38* ***(3.1%)*** | |
| | *LISCOAST* | *Kirezci* | |
| *Area Flooded under EWL for 2050* | *70388.67* ***(3.43%)*** | *67475.24* ***(3.29%)*** | ***RCP4.5*** |
| | *72896.87* ***(3.55%)*** | *68715.76* ***(3.35%)*** | ***RCP8.5*** |
| *Area Flooded under EWL for 2100* | *82113.2* ***(4%)*** | *78069* ***(3.8%)*** | ***RCP4.5*** |
| | *95580.5* ***(4.66%)*** | *88794.16* ***(4.33%)*** | ***RCP8.5*** |

Surge flooding during extreme weather conditions does not vary significantly according to the scenarios or the EWL dataset used. In 2050, a surge flooding of 3.29% in the best-case scenario and 3.55% in the worst-case scenario is predicted, which means that the sea will be approximately 35 meters inland compared to now on average. As shown in Figure 4.13-B, this proves that the interaction of the ruins near the coast with the sea will increase considerably during strong storms.

By 2100, the difference that a change in the emissions scenario will make is clearer. The scenario change, which creates a difference of 0.6% in both datasets, also led to a widening of the difference between the datasets' predictions. The spectrum between the best-case and worst-case scenarios nearly triples from 0.26% to 0.86%. Figure 4.13-C shows that Anemurium loses its entire beach in 2100. At the same time, the mouth of the river to the east of the city expands and is inundated and the seawater moves to the back of the eastern side of the city.

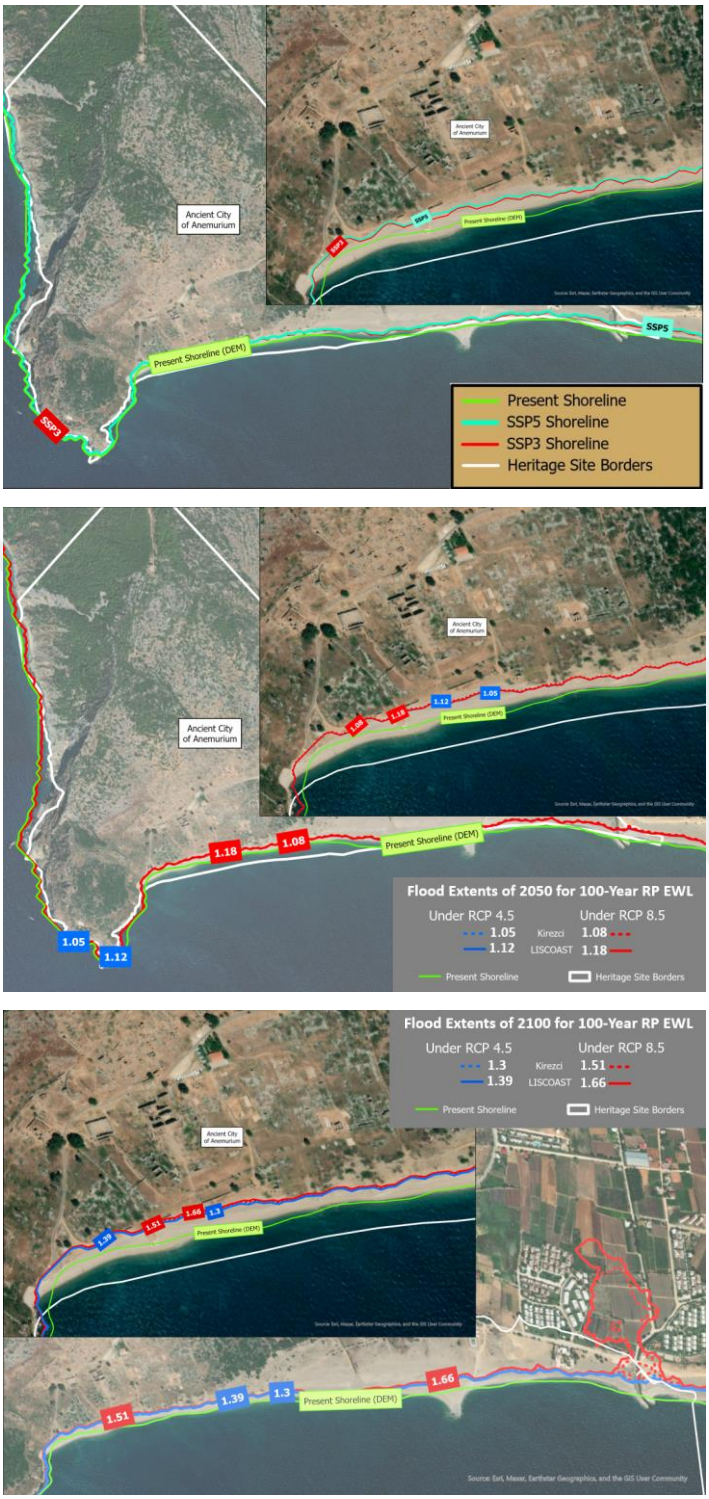



Figure 4.13 Anemurium sBTM Inundation and Flood Maps using GLO-30 (A: Inundation in 2100, B: Storm Surge Flooding in 2050, C: Storm Surge Flooding in 2100)

#### 4.4.2.1.2 UAV

Table 4.8 shows that when the detailed surface model is used, the inundated areas are reduced by up to 50%. The amount of SSP2 inundation obtained using GLO-30 could not be reached even with the LISCOAST 2100 RCP8.5 EWL, which has the largest value. Figures prepared with high-resolution photographs taken while obtaining the detailed surface model reveal that although the loss of area is relatively low, the remains on the coast will still interact with the sea considerably (Figure 4.14). The ruins on the beach to the west of the city appear to be completely surrounded by water during extreme weather conditions in 2100 (Figure 4.16). Figure 4.15-B and Figure 4.16-C also revealed that the seawater will move further inland following the two waterways located east of the city.

Table 4.8 Inundated and Flooded sBTM Areas of Anemurium using UAV DSM

| | ***SSP2*** | ***SSP5*** |
|---|---|---|
| Area Inundated by 2100 | *18596.62* ***(0.91%)*** | *25842.32* ***(1.26%)*** |

| | ***LISCOAST*** | ***Kirezci*** | |
|---|---|---|---|
| *Area Flooded under EWL for 2050* | *29275.28* ***(1.43%)*** | *27793.32* ***(1.35%)*** | ***RCP4.5*** |
| | *31397.69* ***(1.53%)*** | *28501.51* ***(1.39%)*** | ***RCP8.5*** |
| *Area Flooded under EWL for 2100* | *36760.25* ***(1.79%)*** | *34274.1* ***(1.67%)*** | ***RCP4.5*** |
| | *46226.96* ***(2.25%)*** | *40497.23* ***(1.97%)*** | ***RCP8.5*** |

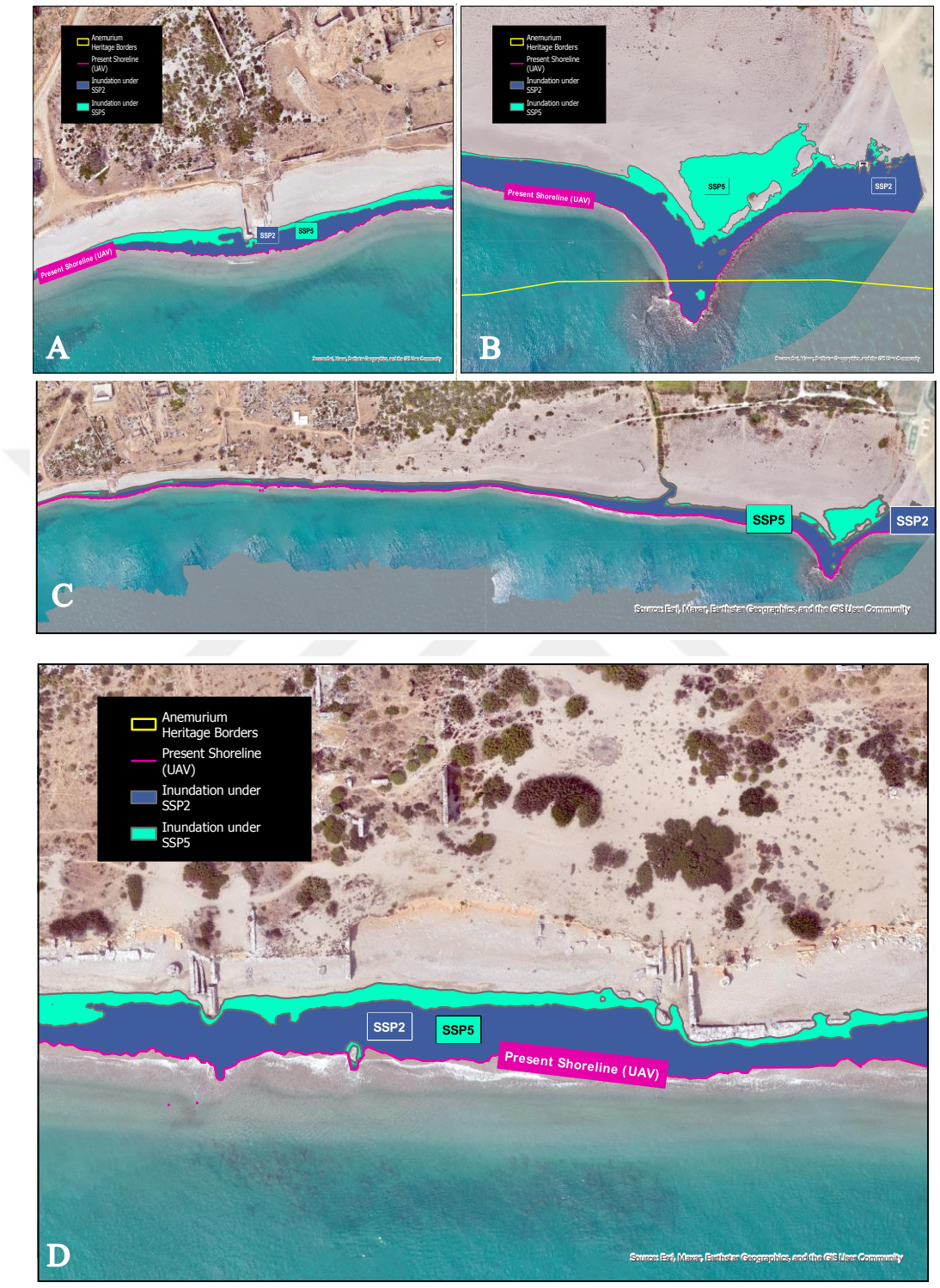



Figure 4.14 Anemurium sBTM Inundation Map using UAV DSM (A: Result near the ruin on the beach, B: Result on the eastern part, C: The whole shoreline, D: Results near the coastal ruins)

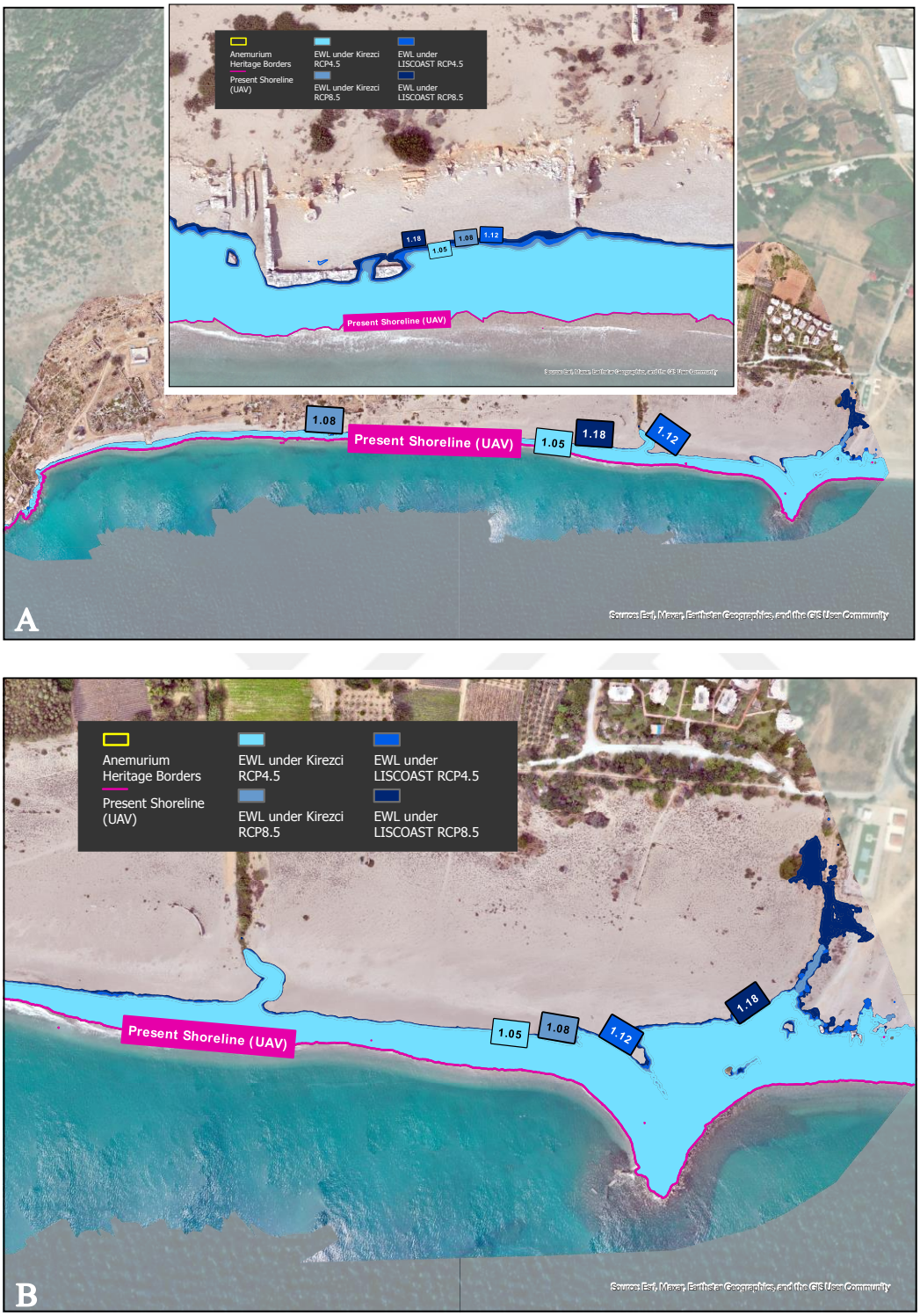



Figure 4.15 Anemurium sBTM Storm Surge Flood Map for 2050 using UAV DSM (A: The whole shoreline focusing on the portion with ruins, B: Result on the eastern part)

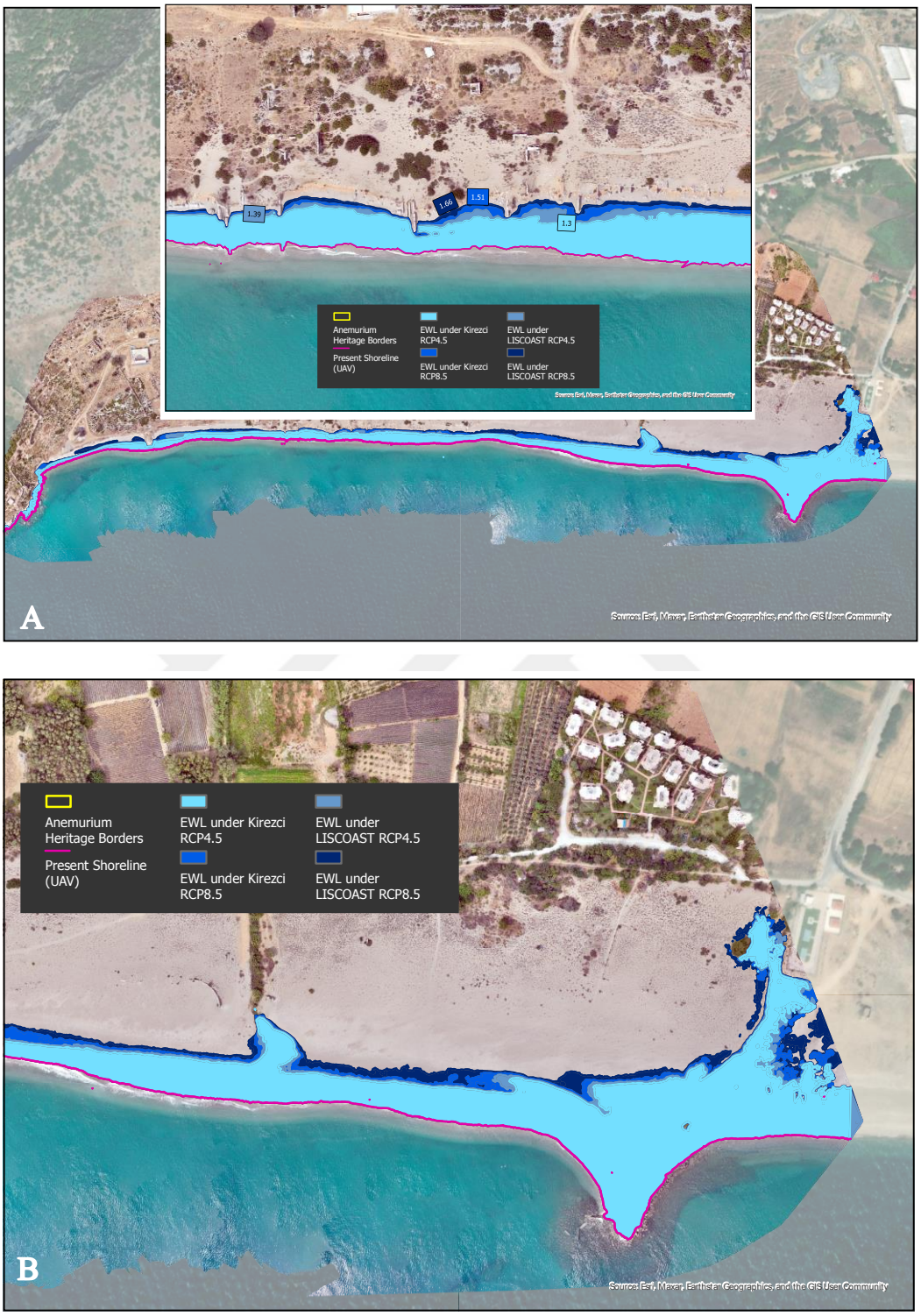



Figure 4.16 Anemurium sBTM Storm Surge Flood Map for 2100 using UAV DSM (A: The whole shoreline focusing on the portion with ruins, B: Result on the eastern part)

#### 4.4.2.2 eBTM

##### 4.4.2.2.1 GLO-30

According to Table 4.9, it is seen that the eBTM method predicts larger flood areas than the sBTM method when GLO-30 data is used. The eBTM method also shows water inflow from the riverbed east of the city, but in a very large amount compared to sBTM. The area lost in 2100 according to the sBTM method is lost in 2050 according to the eBTM method. The interaction of flood waters with heritage remains cannot be observed. Looking at the shoreline, it is clear that the beach west of the city has disappeared, but the water intrusion to the east, which is revealed by the sBTM methods, cannot be observed.

Table 4.9 Inundated and Flooded eBTM Areas of Anemurium using GLO-30

| | ***SSP2*** | ***SSP5*** |
|---|---|---|
| Area Inundated by 2100 | *77585.94* ***(3.78%)*** | *82618.13* ***(4.03%)*** |

| | ***LISCOAST*** | ***Kirezci*** | |
|---|---|---|---|
| *Area Flooded under EWL for 2050* | *85638.86* ***(4.17%)*** | *84951.28* ***(4.14%)*** | ***RCP4.5*** |
| | *88725.6* ***(4.32%)*** | *84951.28* ***(4.14%)*** | ***RCP8.5*** |
| *Area Flooded under EWL for 2100* | *98233* ***(5.85%)*** | *93603* ***(4.79%)*** | ***RCP4.5*** |
| | *106108.66* ***(5.17%)*** | *100286.6* ***(4.89%)*** | ***RCP8.5*** |

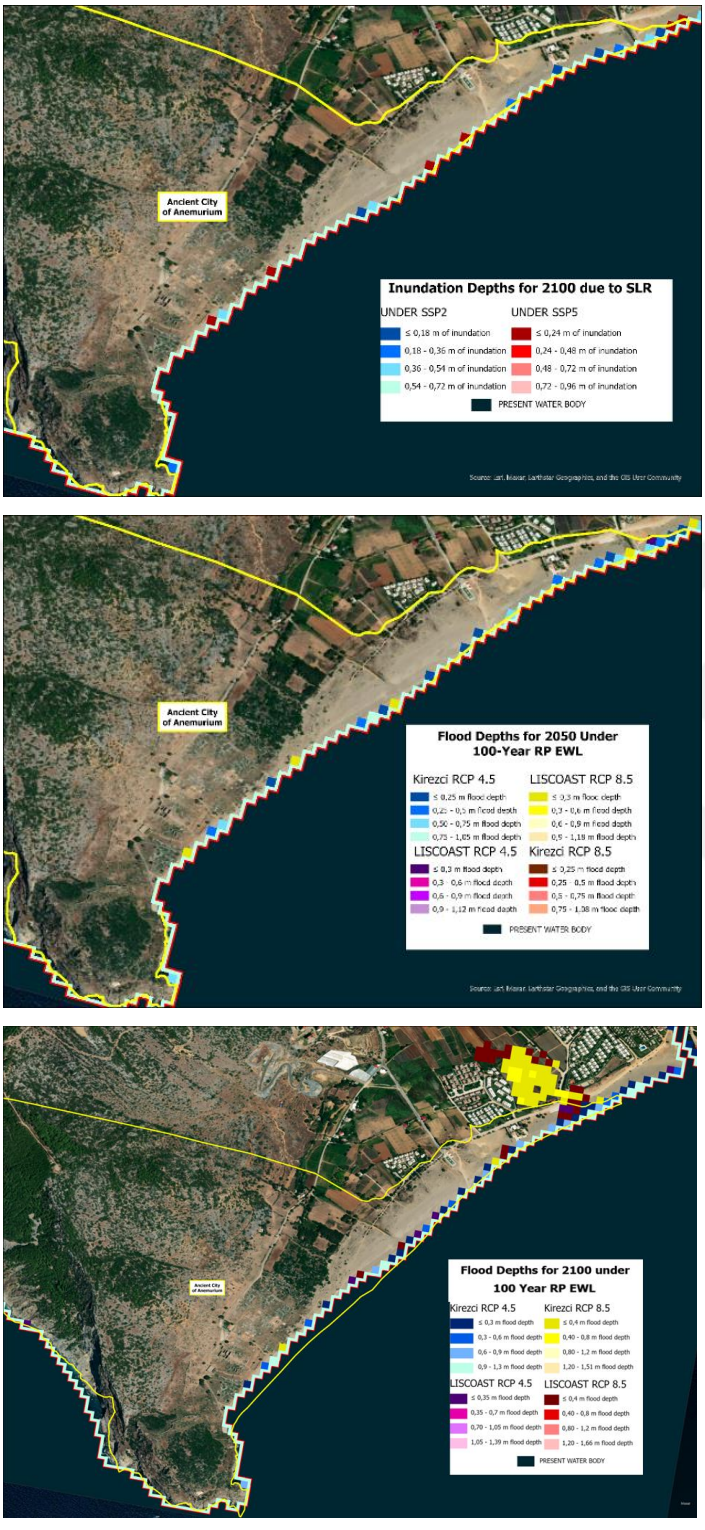



Figure 4.17 Anemurium eBTM Inundation and Flood Maps using GLO-30 (A: Inundation in 2100, B: Storm Surge Flooding in 2050, C: Storm Surge Flooding in 2100)

#### 4.4.2.2.2 UAV

UAV eBTM results shown in Table 4.10 show that the gap between the results of sBTM has reduced significantly. The consistency between two methods improved when the resolution of the elevation model was improved. Figure 4.19 A-B and Figure 4.20 A-B show that the eBTM method can predict the water intrusion around the remains and the present waterways complying with the sBTM method when used with such a detailed elevation model. The results also show that by 2100, Anemurium will lose its beach. The range of area to be lost is narrow, reaching a maximum of 2.1%. The increase in the difference between the emission scenarios in 2050 and 2100 is observed.

Table 4.10 Inundated and Flooded eBTM Areas of Anemurium using UAV-DSM

| | ***SSP2*** | ***SSP5*** | |
|---|---|---|---|
| Area Inundated by 2100 | *18866.35* ***(0.92%)*** | *25684.51* ***(1.25%)*** | |
| | ***LISCOAST*** | ***Kirezci*** | |
| *Area Flooded under EWL for 2050* | *28993.87* ***(1.41%)*** | *27584.57* ***(1.34%)*** | ***RCP4.5*** |
| | *30127.21* ***(1.47%)*** | *28286.24* ***(1.38%)*** | ***RCP8.5*** |
| *Area Flooded under EWL for 2100* | *34935.44* ***(1.7%)*** | *32881.28* ***(1.6%)*** | ***RCP4.5*** |
| | *43057.61* ***(2.1%)*** | *38330.69* ***(1.87%)*** | ***RCP8.5*** |

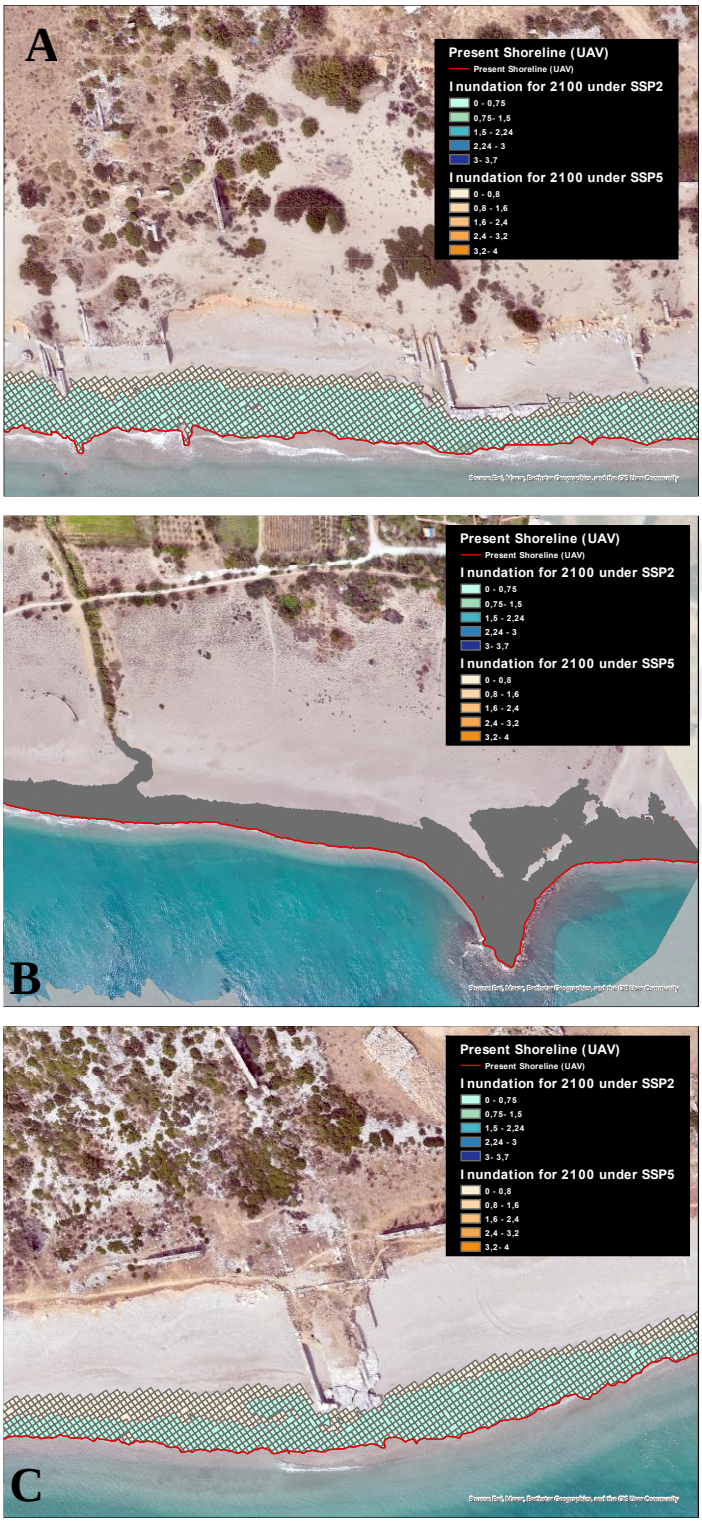



Figure 4.18 Anemurium eBTM Inundation Map for 2100 using UAV DSM (A: Beach Portion with Ruins, B:Eastern Side of the city, C: Situation around the coastal ruin)

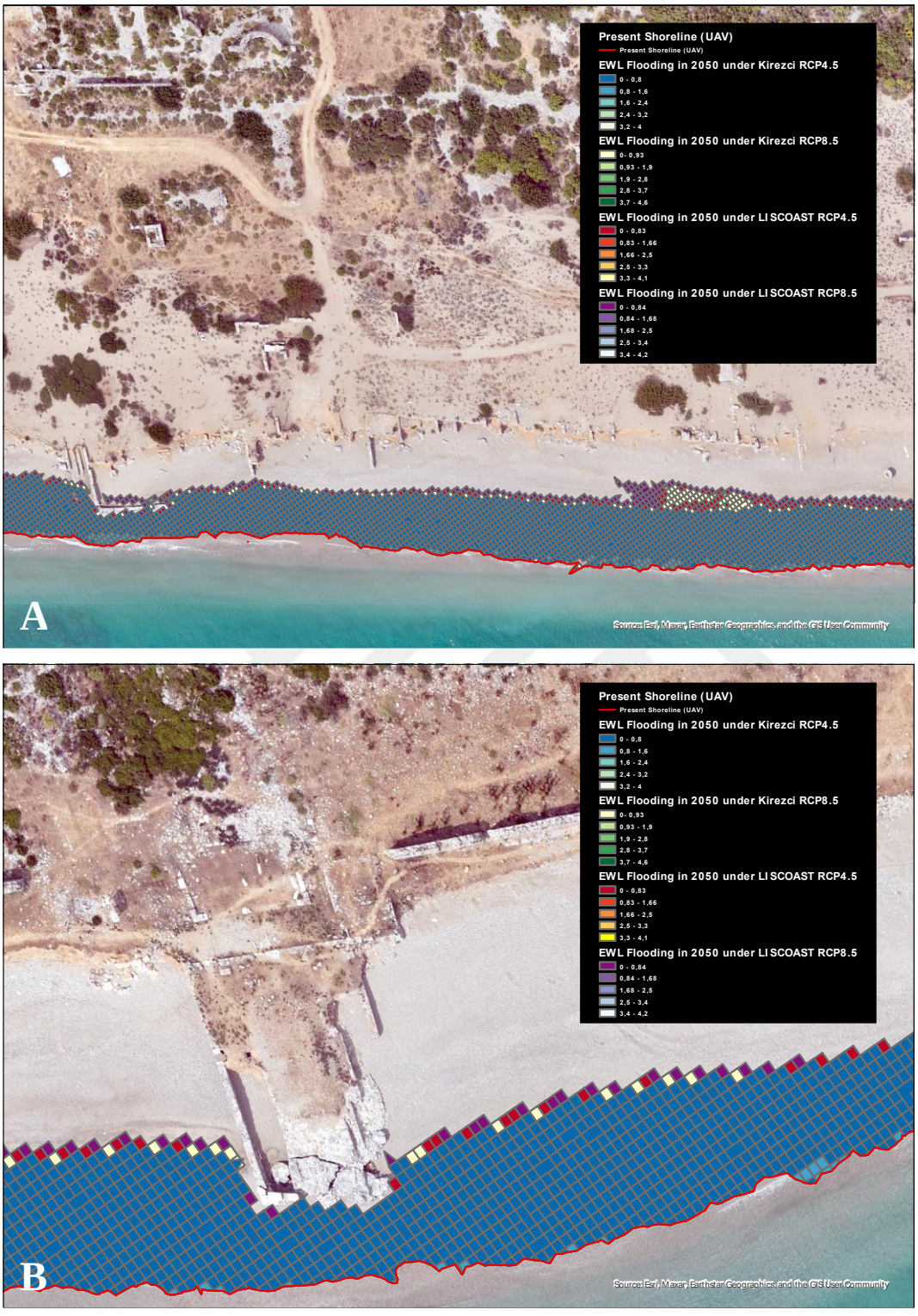



Figure 4.19 Anemurium eBTM Storm Surge Flood Map for 2050 using UAV DSM (A: The beach with ruins, B: Focusing on the building ruin)

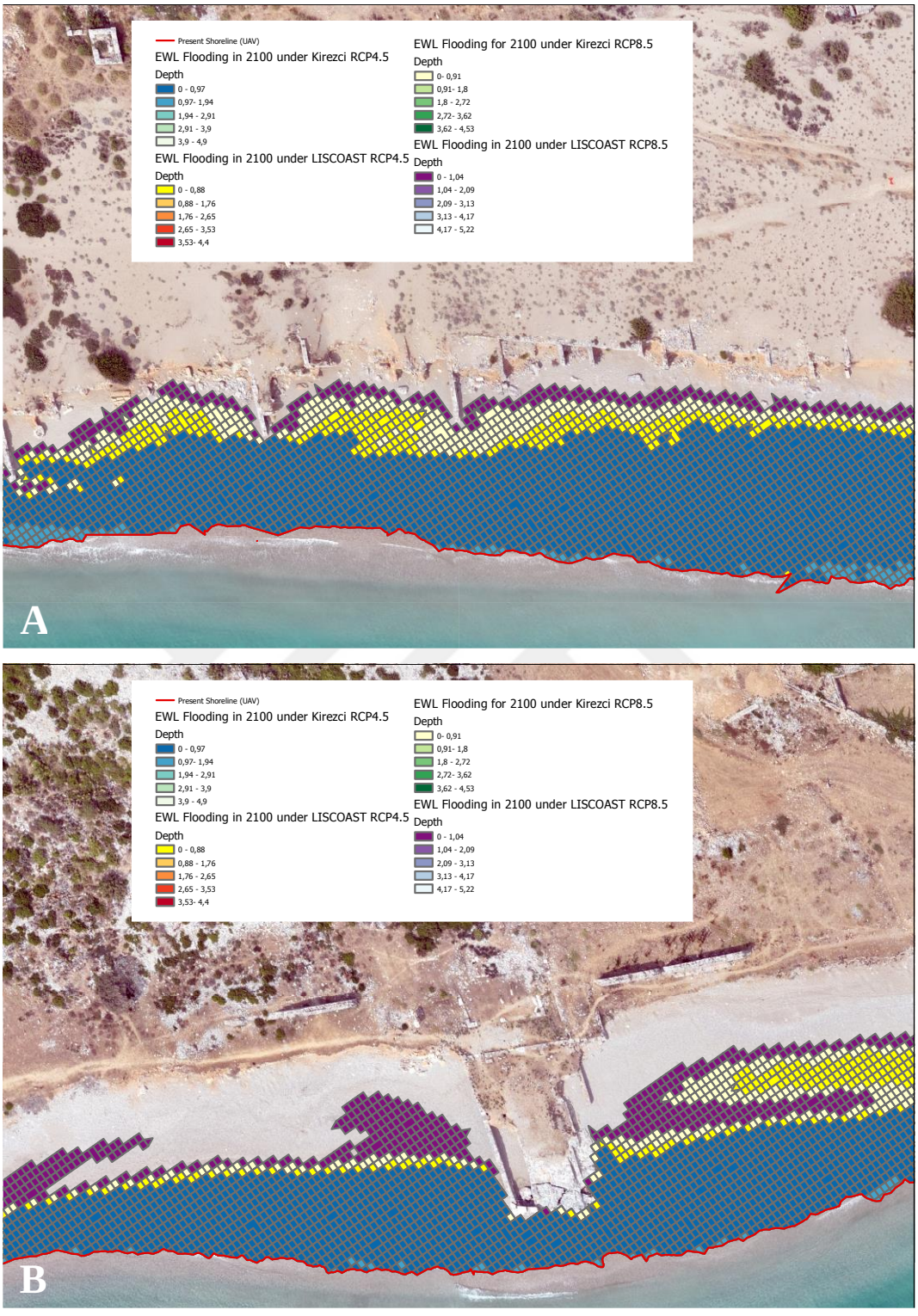



Figure 4.20 Anemurium eBTM Storm Surge Flood Map for 2100 using UAV DSM (A: The beach with ruins, B: Focusing on the building ruin)

### 4.4.3 Ancient City of Soli-Pompeipolis

For Soli-Pompeipolis, two elevation models are used, GLO-30 of Copernicus and the detailed surface model generated in the scope of the project using a UAV. The original UAV model has a 5 cm resolution however a 1 m resolution raster is generated from it for ease of operation in ArcMap.

#### 4.4.3.1 sBTM

##### 4.4.3.1.1 GLO-30 (30 m Resolution)

According to Table 4.11, climate change causes at least 30000 $m^2$ of land loss at Soli-Pompeipolis.

Table 4.11 Inundated and Flooded sBTM Areas of the Ancient City of Soli-Pompeipolis using GLO-30 ($m^2$)

| | ***SSP2*** | ***SSP5*** | |
|---|---|---|---|
| Area Inundated by 2100 | *31128.9* ***(5.72%)*** | *36664.14* ***(6.74%)*** | |
| | ***LISCOAST*** | ***Kirezci*** | |
| *Area Flooded under EWL for 2050* | *37299.4* ***(6.86%)*** | *33778* ***(6.21%)*** | ***RCP4.5*** |
| | *39451.76* ***(7.25%)*** | *34669* ***(6.37%)*** | ***RCP8.5*** |
| *Area Flooded under EWL for 2100* | *43229* ***(7.95%)*** | *39215.9* ***(7.21%)*** | ***RCP4.5*** |
| | *50062.2* ***(9.2%)*** | *43458* ***(8%)*** | ***RCP8.5*** |

Figure 4.21 shows that the majority of the land loss happens at the sandy beaches to the west and east of the ancient breakwater. The western ancient breakwater gets completely inundated.

In 2050, in case of a 100-year RP storm surge, the water will reach approximately to the predicted shoreline in 2100. The LISCOAST having greater flooding is expected, however, even Kirezci value under RCP8.5 causes less flooding than that of LISCOAST RCP4.5.

In 2100, it is seen in Figure 4.21-C that the eastern breakwater also, which is under the current pavement, gets flooded during a strong storm surge. On the eastern beach, the flooding extent is rather small compared to the western one.

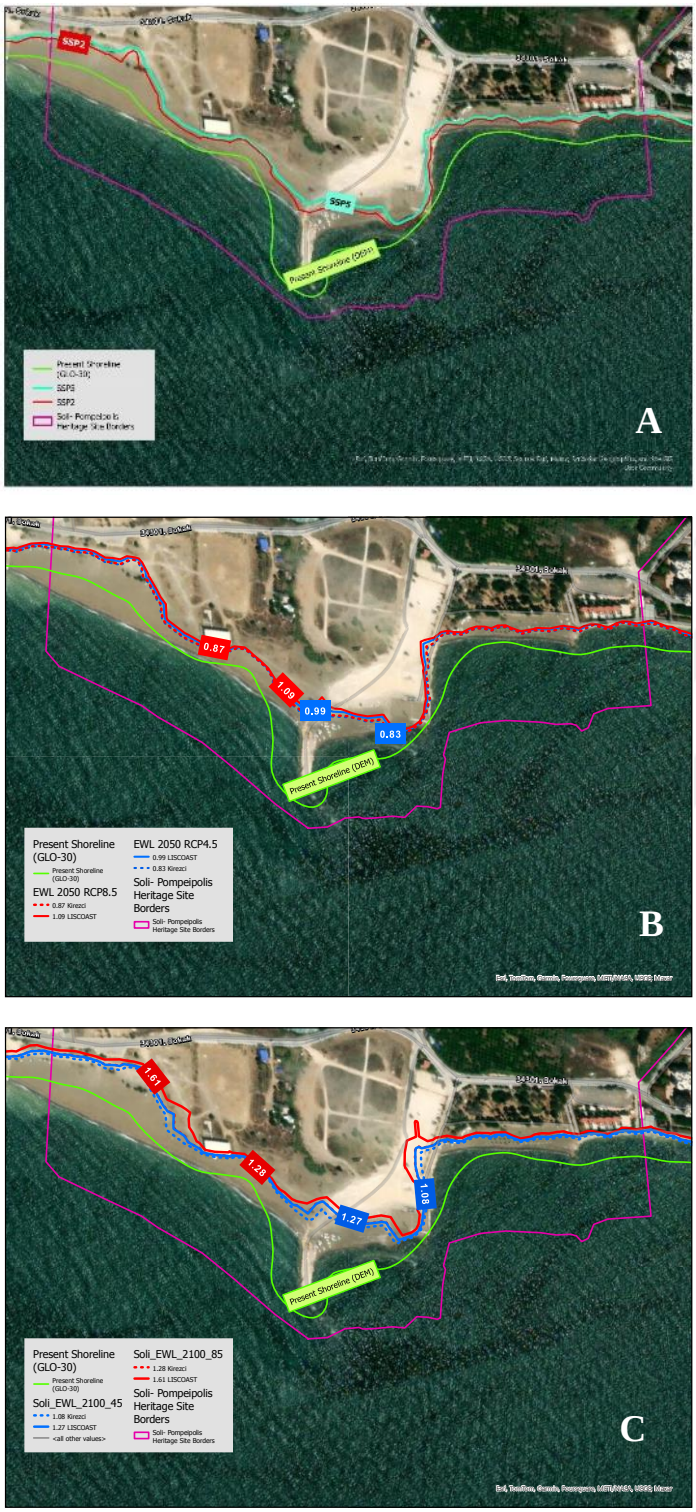



Figure 4.21 Soli-Pompeipolis sBTM Inundation and Flood Maps using GLO-30 (A: Inundation in 2100, B: Storm Surge Flooding in 2050, C: Storm Surge Flooding in 2100)

#### 4.4.3.1.2 UAV Generated DSM (1 m Resolution)

According to Figure 4.22-A, the city has mostly permanently lost the beach to the west of the ancient harbour, and even in the good scenario SSP2 the sea comes in about 80 m inland. The same intrusion was not observed on the beach east of the harbour The western breakwater is partially submerged.

According to the 2050 EWL projections shown in Table 4.12, the flooded area varies by less than 1% across scenarios and datasets. In this scenario, in addition to the inundated area, there is no clear flooded area that would make a significant difference. The detailed elevation model led to smaller inundation/flood areas in all the cases except for the surge flooding of LISCOAST RCP8.5 in 2100. In this scenario, the water re-floods the space between the two ancient breakwaters, which used to be the harbor area, and the flooding area doubles those of the other scenarios.

Table 4.12 Inundated and Flooded sBTM Areas of the Ancient City of Soli-Pompeipolis using UAV DSM ($m^2$)

| | ***SSP2*** | ***SSP5*** | |
|---|---|---|---|
| Area Inundated by 2100 | *18476.57* ***(3.4%)*** | *24289.4* ***(4.46%)*** | |
| | ***LISCOAST*** | ***Kirezci*** | |
| *Area Flooded under EWL for 2050* | *25238.69* ***(4.64%)*** | *22914.32* ***(4.21%)*** | ***RCP4.5*** |
| | *27445.94* ***(5.04%)*** | *23000* ***(4.23%)*** | ***RCP8.5*** |
| *Area Flooded under EWL for 2100* | *31707.49* ***(5.83%)*** | *27258.43* ***(5.01%)*** | ***RCP4.5*** |
| | *59983.8* ***(11.02%)*** | *31842.93* ***(5.85%)*** | ***RCP8.5*** |

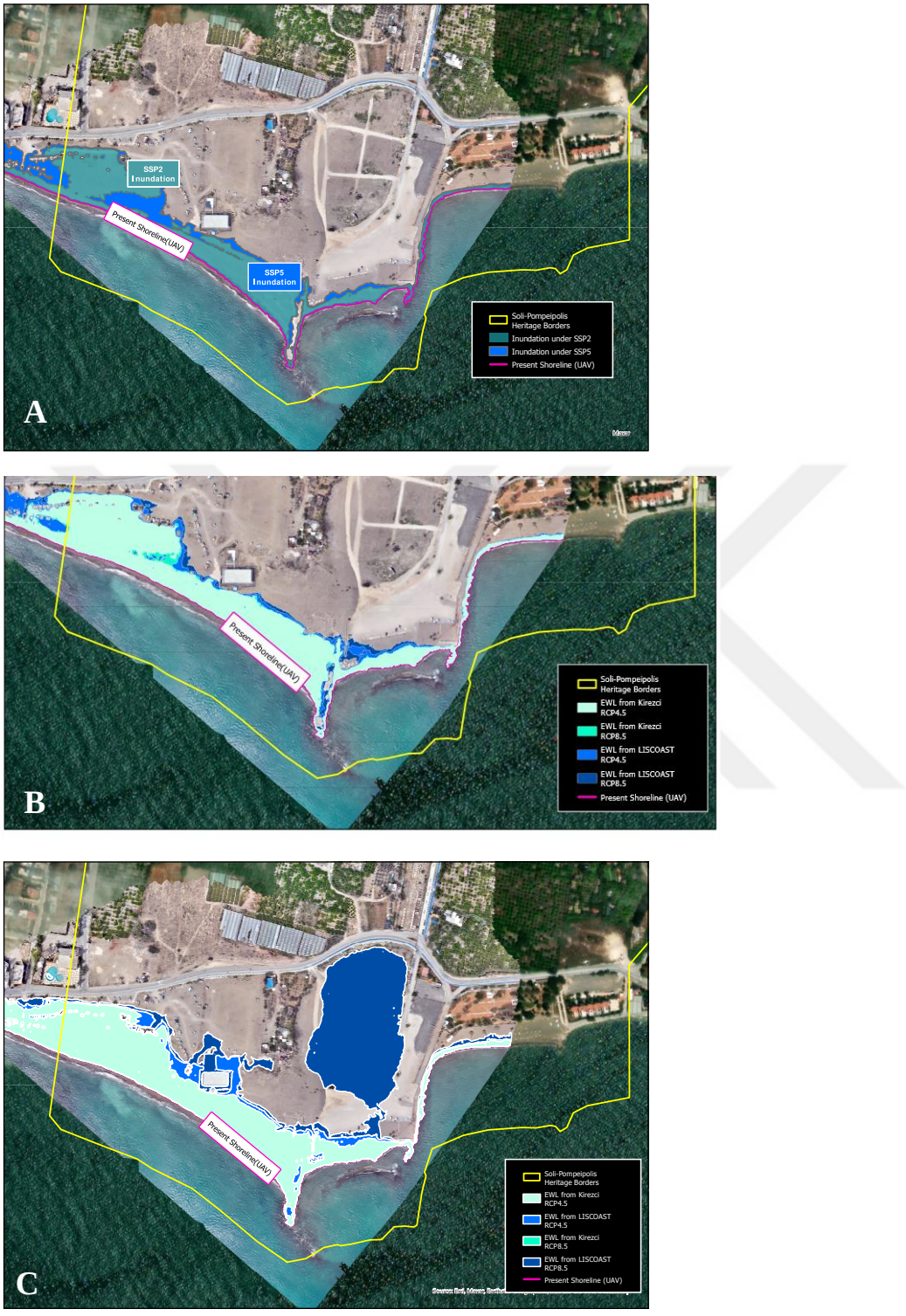



Figure 4.22 Soli-Pompeipolis sBTM Inundation and Flood Maps using UAV DSM (A: Inundation in 2100, B: Storm Surge Flooding in 2050, C: Storm Surge Flooding in 2100)

#### 4.4.3.2 eBTM

##### 4.4.3.2.1 GLO-30

When GLO-30 DEM is used for eBTM analysis, results are in good agreement with those of sBTM analysis. The inundation of the western breakwater is also visible here; however, the loss of the western sandy beach is not as clear. 2050 flood areas and 2100 inundation areas are very close to each other for this method and area. The filling of the area between the two breakwaters with water seen in the sBTM method prepared with UAV is not observed in Figure 4.23-C, but it is seen that the west breakwater is approximately 30 cm under water even in LISCOAST 4.5. It is also observed that the progression of the water to the central area is from the west breakwater line. In the worst-case scenario, LISCOAST RCP8.5, although the flooded area is larger than in the sBTM method prepared with GLO-30 and smaller than in the sBTM method prepared with UAV, the results are close to each other with 1-2% difference.

Table 4.13 Inundated and Flooded eBTM Areas of the Ancient City of Soli-Pompeipolis using GLO-30 ($m^2$)

| | ***SSP2*** | ***SSP5*** | |
|---|---|---|---|
| Area Inundated by 2100 | *32399.63* ***(5.95%)*** | *38477.16* ***(7.07%)*** | |
| | ***LISCOAST*** | ***Kirezci*** | |
| *Area Flooded under EWL for 2050* | *39287.67* ***(7.22%)*** | *34700.34* ***(6.38%)*** | ***RCP4.5*** |
| | *40053.13* ***(7.36%)*** | *36254* ***(6.66%)*** | ***RCP8.5*** |
| | | | |
| *Area Flooded under EWL for 2100* | *48820* ***(8.97%)*** | *40055.2* ***(7.36%)*** | ***RCP4.5*** |
| | *54182.74* ***(9.96%)*** | *48823.4* ***(8.97%)*** | ***RCP8.5*** |

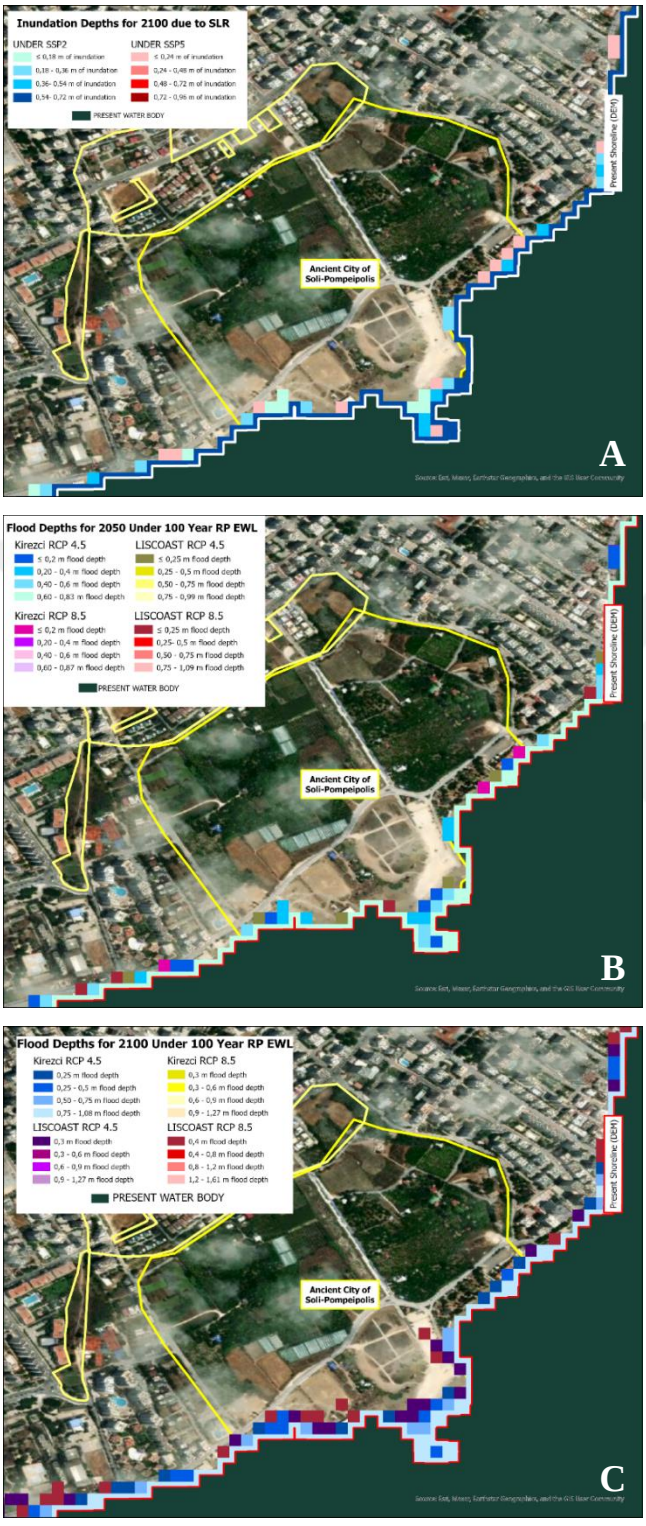



Figure 4.23 Soli-Pompeipolis eBTM Inundation and Flood Maps using GLO-30 (A: Inundation in 2100, B: Storm Surge Flooding in 2050, C: Storm Surge Flooding in 2100)

#### 4.4.3.2.2 UAV

The results of the eBTM method prepared with the UAV agree with the sBTM method. In fact, for most cases, the difference is less than 200 $m^2$. Even in the Kirezci RCP8.5 scenario for 2100, the two methods give almost the same result with a difference of 1 $m^2$. The eBTM method was able to capture the flooding of the area between the two breakwaters at this resolution, and the flooded area was twice as large in this scenario. Again, the inundation and flooding of the beach west of the harbor is also observed by eBTM at the resolution.

Table 4.14 Inundated and Flooded eBTM Areas of the Ancient City of Soli-Pompeipolis using UAV DSM ($m^2$)

| | ***SSP2*** | ***SSP5*** | |
|---|---|---|---|
| Area Inundated by 2100 | *18408.32* ***(3.38%)*** | *24472.29* ***(4.5%)*** | |
| | ***LISCOAST*** | ***Kirezci*** | |
| *Area Flooded under EWL for 2050* | *25230.92* ***(4.64%)*** | *21843* ***(4.01%)*** | ***RCP4.5*** |
| | *27411.41* ***(5.04%)*** | *22796.88* ***(4.19%)*** | ***RCP8.5*** |
| *Area Flooded under EWL for 2100* | *31717.23* ***(5.83%)*** | *27249.69* ***(5.01%)*** | ***RCP4.5*** |
| | *59793.64* ***(11%)*** | *31843.96* ***(5.85%)*** | ***RCP8.5*** |

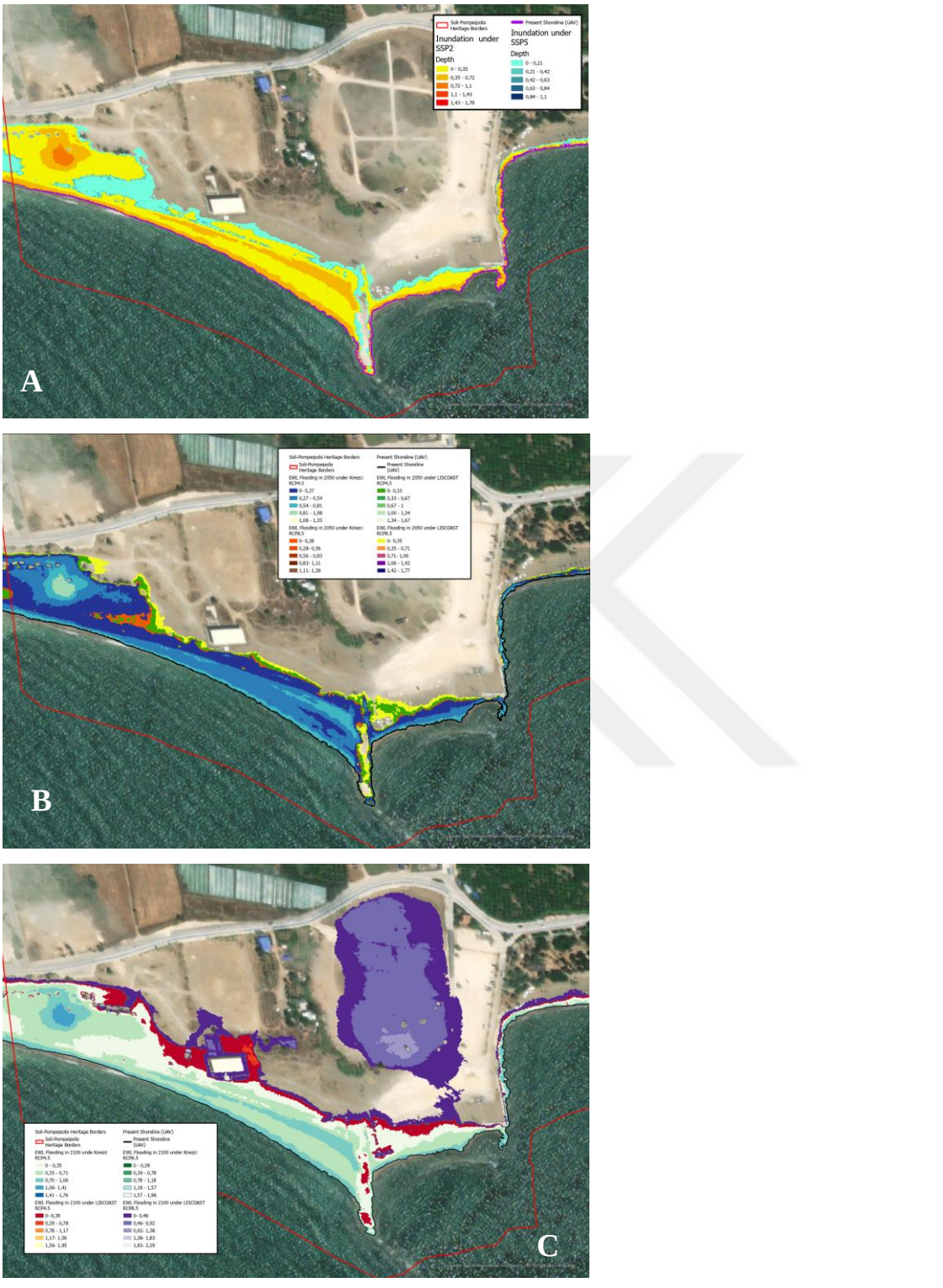



Figure 4.24 Soli-Pompeipolis eBTM Inundation and Flood Maps using UAV DSM (A: Inundation in 2100, B: Storm Surge Flooding in 2050, C: Storm Surge Flooding in 2100)

### 4.4.4 Ancient City of Teos

For the Ancient City of Teos, four different DEM datasets were used for both sBTM and eBTM. The additional one is the terrain model generated from the UAV model. For the Delft3D application, SYM-5 was used.

#### 4.4.4.1 sBTM

##### 4.4.4.1.1 GLO-30

Table 4.15 shows that by 2100, Teos will lose approximately 8% of land to the sea. Depending on the emission scenario used in the study, the inundated area might increase about 2000 $m^2$.

Table 4.15 Inundated and Flooded sBTM Areas of the Ancient City of Teos using GLO-30 ($m^2$)

| | ***SSP2*** | ***SSP5*** | |
|---|---|---|---|
| Area Inundated by 2100 | *228972.33* ***(7.92%)*** | *247069.14* ***(8.54%)*** | |
| | ***LISCOAST*** | ***Kirezci*** | |
| *Area Flooded under EWL for 2050* | *265355.64* ***(9.18%)*** | *230145.78* ***(7.96%)*** | ***RCP4.5*** |
| | *282406.73* ***(9.77%)*** | *233536.51* ***(8.08%)*** | ***RCP8.5*** |
| *Area Flooded under EWL for 2100* | *312301.85* ***(10.8%)*** | *267940.11* ***(9.27%)*** | ***RCP4.5*** |
| | *373956.27* ***(12.93%)*** | *302002.6* ***(10.44%)*** | ***RCP8.5*** |

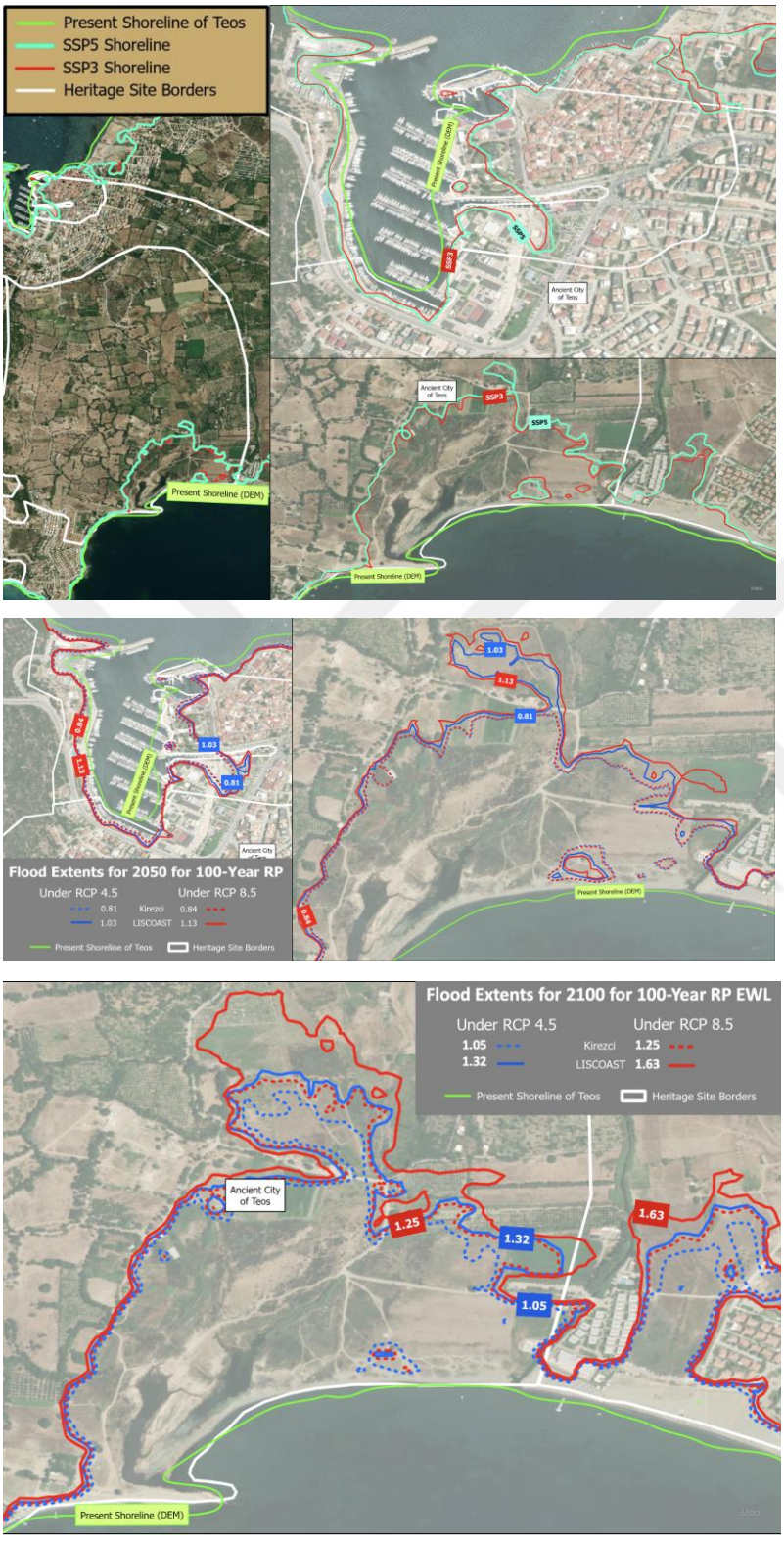



Figure 4.25 Teos sBTM Inundation and Flood Maps using GLO-30 (A: Inundation in 2100, B: Storm Surge Flooding in 2050, C: Storm Surge Flooding in 2100)

This inundation will take place mostly around the ancient harbour of Teos which is the South harbor (Figure 4.25-A). The inundation in the north doesn't reach to the conservation site in 2100 even for SSP5 (Figure 4.25-A). During an extreme weather event in 2050, the flooded area accounts for around 8-9% of the conservation site. It is noticeable that the Kirezci value for RCP8.5 causes less flooding than the LISCOAST value for RCP4.5. When the emission scenario switches, there isn't a significant increase in the flooding caused by Kirezci predictions, however, LISCOAST predictions add another 2000 $m^2$. This means that in 2050, in the Kirezci dataset, the emission scenario doesn't affect the predictions as much as it does for the LISCOAST dataset. The flooded area continues around the small streambed behind the south harbour and along the whole beach (Figure 4.25-B). In 2100, the flooded area reaches 10% of Teos and the water moves far inland from the south harbor so much that it reaches other buildings of the ancient city (Figure 4.25-C).

#### 4.4.4.1.2 SYM-5

When the SYM-5 elevation dataset of the General Directorate of Mapping is used, the inundated and flooded areas change drastically. The first significant change is in the inundation extent. Under SSP2 scenario with 0.8 m of sea level rise, the inundated area is only 0.33% of the conservation area, which is around 4% of the predicted area with GLO-30. This rather small inundation area is also valid for storm surge flooding in 2050 under Kirezci's predictions of 0.81 and 0.84 m water levels. However, when the water level prediction is 0.96 m, the inundated area is 4 times as much, which is due to the water intrusion through the northern end of the ancient city (Figure 4.26-A).

Table 4.16 Inundated and Flooded sBTM Areas of the Ancient City of Teos using SYM-5 ($m^2$)

| | ***SSP2*** | ***SSP5*** |
|---|---|---|
| Area Inundated by 2100 | *9565.42* ***(0.33%)*** | *37641.48* ***(1.3%)*** |

| | ***LISCOAST*** | ***Kirezci*** | |
|---|---|---|---|
| *Area Flooded under EWL for 2050* | *127595.23* ***(4.41%)*** | *9770.7* ***(0.34%)*** | ***RCP4.5*** |
| | *144185.31* ***(4.99%)*** | *10477.52* ***(0.36%)*** | ***RCP8.5*** |
| *Area Flooded under EWL for 2100* | *166323.62* ***(5.75%)*** | *131454.32* ***(4.55%)*** | ***RCP4.5*** |
| | *187287.02* ***(6.48%)*** | *160739.39* ***(5.56%)*** | ***RCP8.5*** |

The flooded area's given by this elevation model for 2050, and 2100 years are half of those given by GLO-30. Kirezci values do not cause almost any flooding in 2050,

but this amount reaches to 5.6% in 2100 (Table 4.16). Under LISCOAST predictions, it is seen that the flooding will occur both in the south harbour and the north harbor so much that it reaches the conservation area (Figure 4.27-A). The water intrusion in the south (Figure 4.27-B) complies with the GLO-30 models. One significant difference of this elevation model is that the shoreline at the south harbour is captured differently. It is seen that this model was generated when the stream mouths were open and flowing, thus the shoreline reaches much more inland.

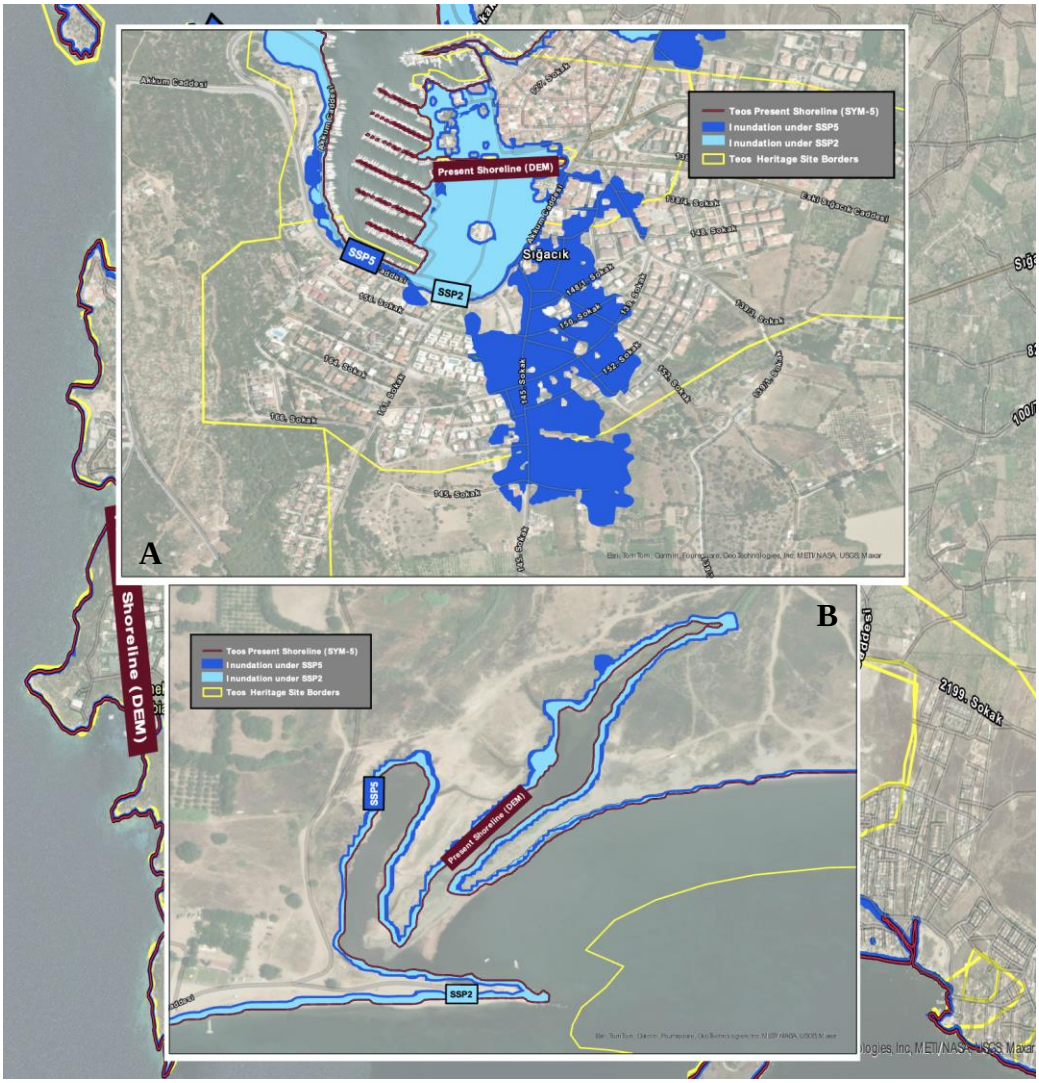



Figure 4.26 Teos sBTM Inundation Maps using SYM-5 (A: Inundation from the Teos Marina (Ancient North Harbour), B: Inundation at the South Ancient Harbour)

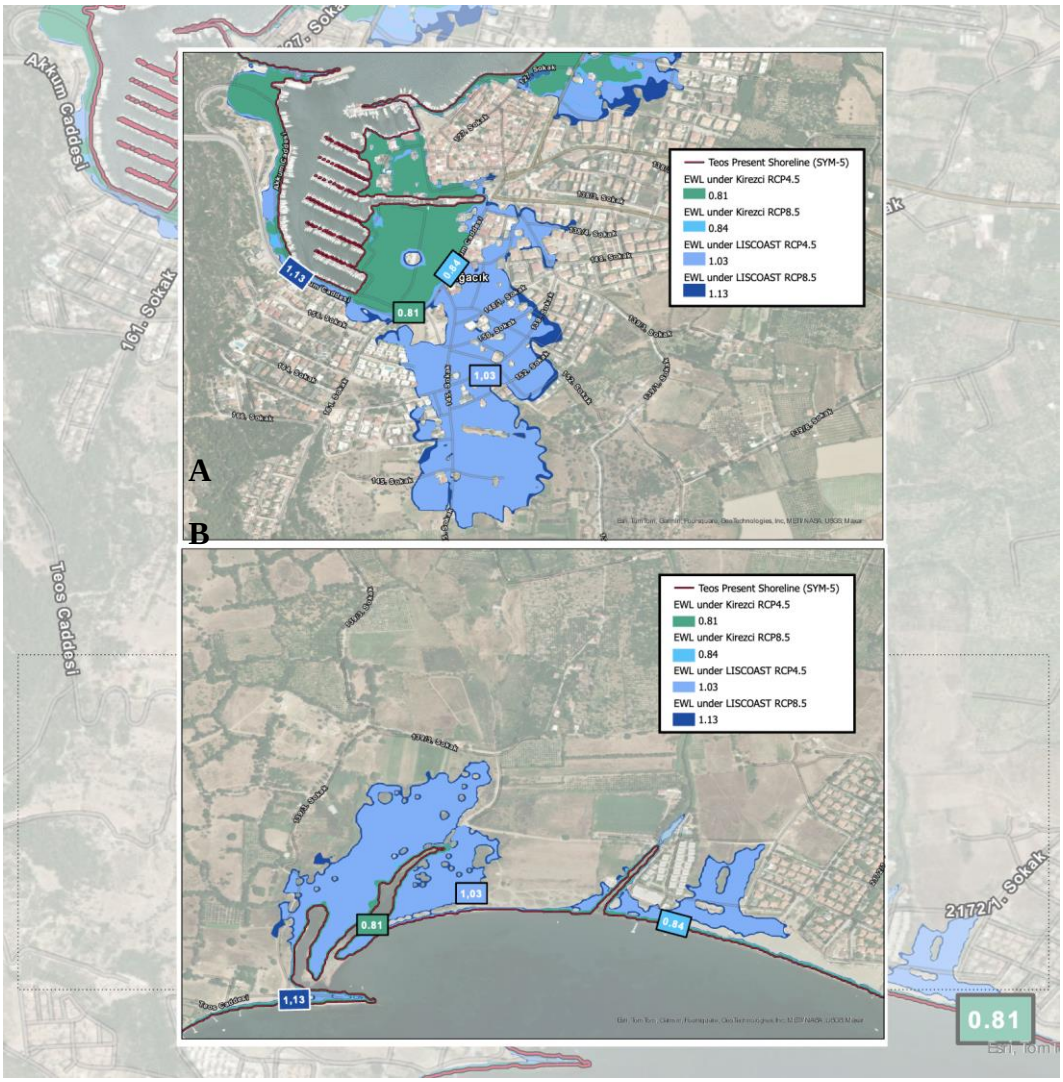



Figure 4.27 Teos sBTM Flooding Maps for 2050 using SYM-5 (A: Flooding from the Teos Marina (Ancient North Harbour), B: Flooding at the South Ancient Harbour)

Under EWL conditions in 2100, all scenarios cause flooding in both North and South harbours, with flood area ranging between 4.5% and 6.5%. The flooding in the North continues through Sığacık and reaches the first-degree conservation area (Figure 4.28-A). In the South, the flooding continues on the area behind the ancient breakwater. The sea connects intruding on the ancient breakwater and the ancient breakwater is completely submerged except for certain stone blocks.

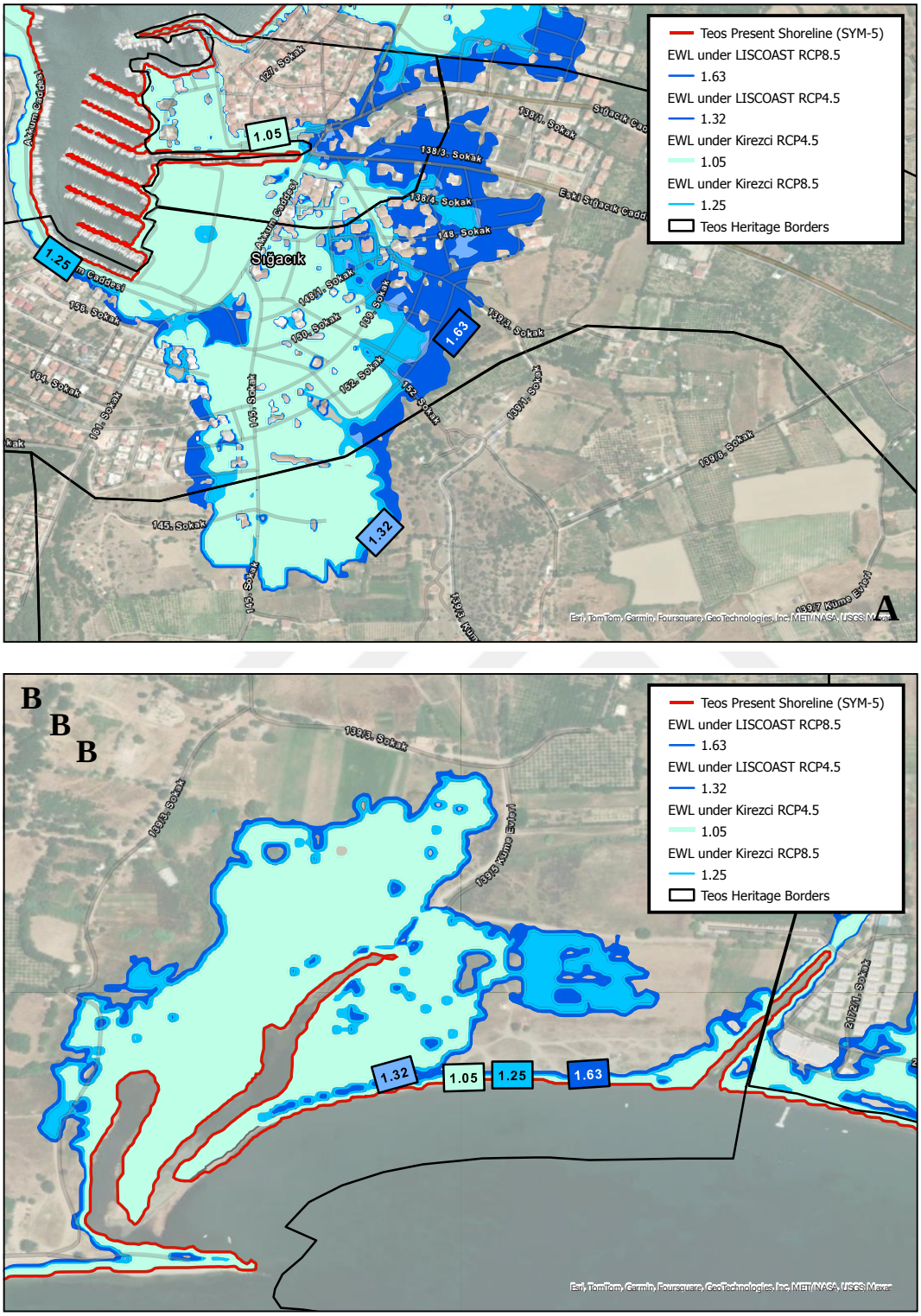



Figure 4.28 Teos sBTM Flooding Maps for 2100 using SYM-5 (A: Flooding from the Teos Marina (Ancient North Harbour), B: Flooding at the South Ancient Harbour)

#### 4.4.4.1.3 UAV DSM

❖ **Digital Surface Model (DSM)**

Firstly, it should be noted about the UAV-generated elevation model of Teos that the flight area of the UAV to cover the whole conservation area was not possible due to site and weather conditions. Thus, the elevation model was generated only for the south harbor area. In other words, water intrusion into the area from the north, if it is the case, won't be able to be seen with the maps prepared using UAV. UAV DSM gave similar results to SYM-5 in terms of inundation and Kirezci predictions for 2050. The areas were rather limited for these cases in SYM-5, and even smaller for UAV-DSM, covering only 0.1% (Table 4.17). It is seen that the inundation area increases dramatically for SSP5. But this increase happens due to flooding in the south harbor, not because of flooding from the north like in the SYM-5 case.

Table 4.17 Inundated and Flooded sBTM Areas of the Ancient City of Teos using UAV-DSM ($m^2$)

| | ***SSP2*** | ***SSP5*** | |
|---|---|---|---|
| Area Inundated by 2100 | *3219.42* ***(0.11%)*** | *80632.9* ***(2.79%)*** | |
| | ***LISCOAST*** | ***Kirezci*** | |
| *Area Flooded under EWL for 2050* | *94712.58* ***(3.28%)*** | *3360.5* ***(0.12%)*** | ***RCP4.5*** |
| | *107498.86* ***(3.72%)*** | *3930.7* ***(0.14%)*** | ***RCP8.5*** |
| *Area Flooded under EWL for 2100* | *152374.09* ***(5.27%)*** | *107458.16* ***(3.72%)*** | ***RCP4.5*** |
| | *202902.68* ***(7.02%)*** | *140817.35* ***(4.87%)*** | ***RCP8.5*** |

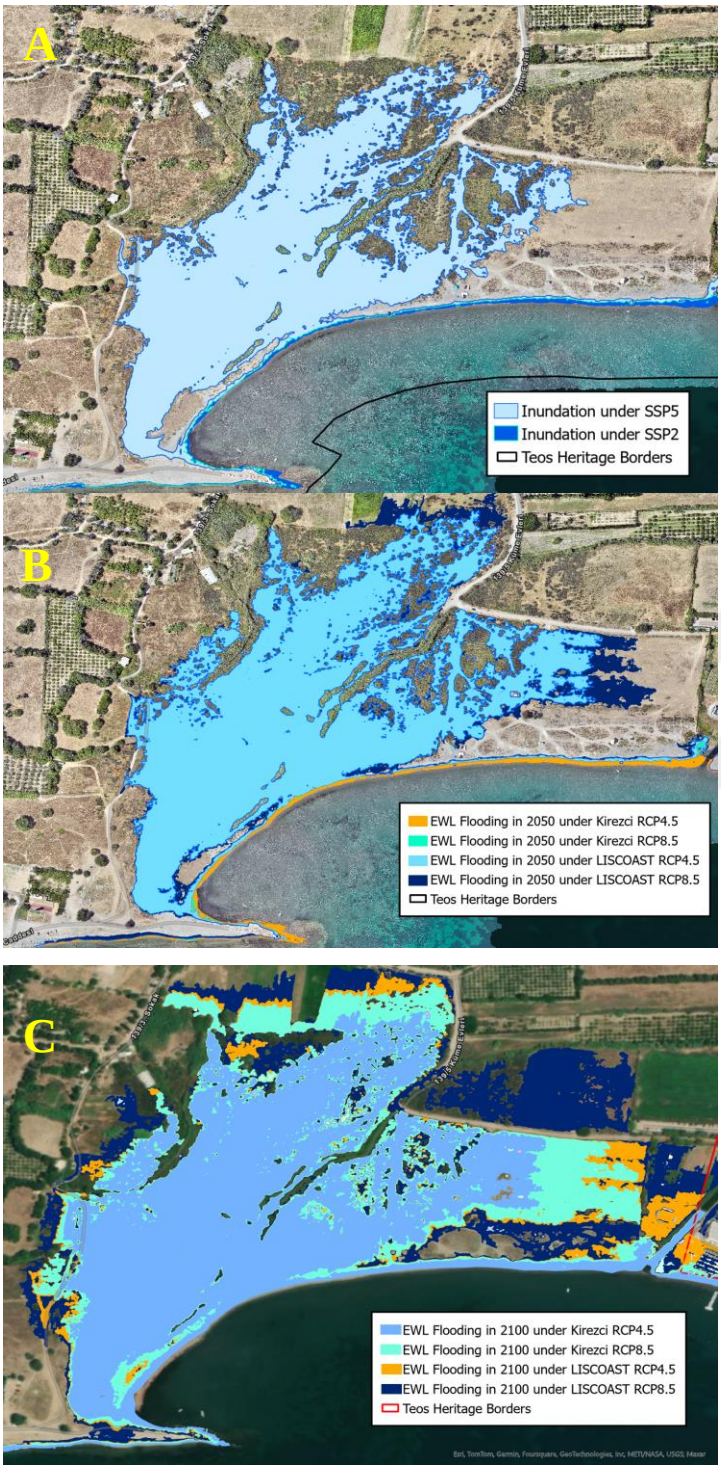



Figure 4.29 Teos sBTM Inundation and Flood Maps using UAV DSM (A: Inundation in 2100, B: Storm Surge Flooding in 2050, C: Storm Surge Flooding in 2100)

For the other scenarios, the difference between the SYM-5 and UAV DSM results is around 1% even though the north part of the site is not included in the DSM. In other words, DSM gave bigger results than SYM-5, considering the flooding through the north is included in SYM-5. Figure 4.29 A-C shows that the ancient breakwater is not being flooded as it was with the previous models. Even though the flood path behind the breakwater and along the stream is similar, the area west of the breakwater did not show the same amount of flooding.

- **Digital Terrain Model (DTM)**

The inundation and flood areas of the DTM model are in good agreement with those of DSM mode comparison of the areas presented in Table 4.18 and Table 4.17.

Table 4.18 Inundated and Flooded sBTM Areas of the Ancient City of Teos using UAV DTM ($m^2$)

| | ***SSP2*** | ***SSP5*** | |
|---|---|---|---|
| Area Inundated by 2100 | *3242.42* ***(0.11%)*** | *86690.58* ***(3%)*** | |
| | ***LISCOAST*** | ***Kirezci*** | |
| *Area Flooded under EWL for 2050* | *92735* ***(3.2%)*** | *3441.31* ***(0.12%)*** | ***RCP4.5*** |
| | *108842.6* ***(3.76%)*** | *3934.32* ***(0.14%)*** | ***RCP8.5*** |
| *Area Flooded under EWL for 2100* | *155701.79* ***(5.38%)*** | *110730.57* ***(4.05%)*** | ***RCP4.5*** |
| | *205128.74* ***(7.09%)*** | *141086.33* ***(4.87%)*** | ***RCP8.5*** |

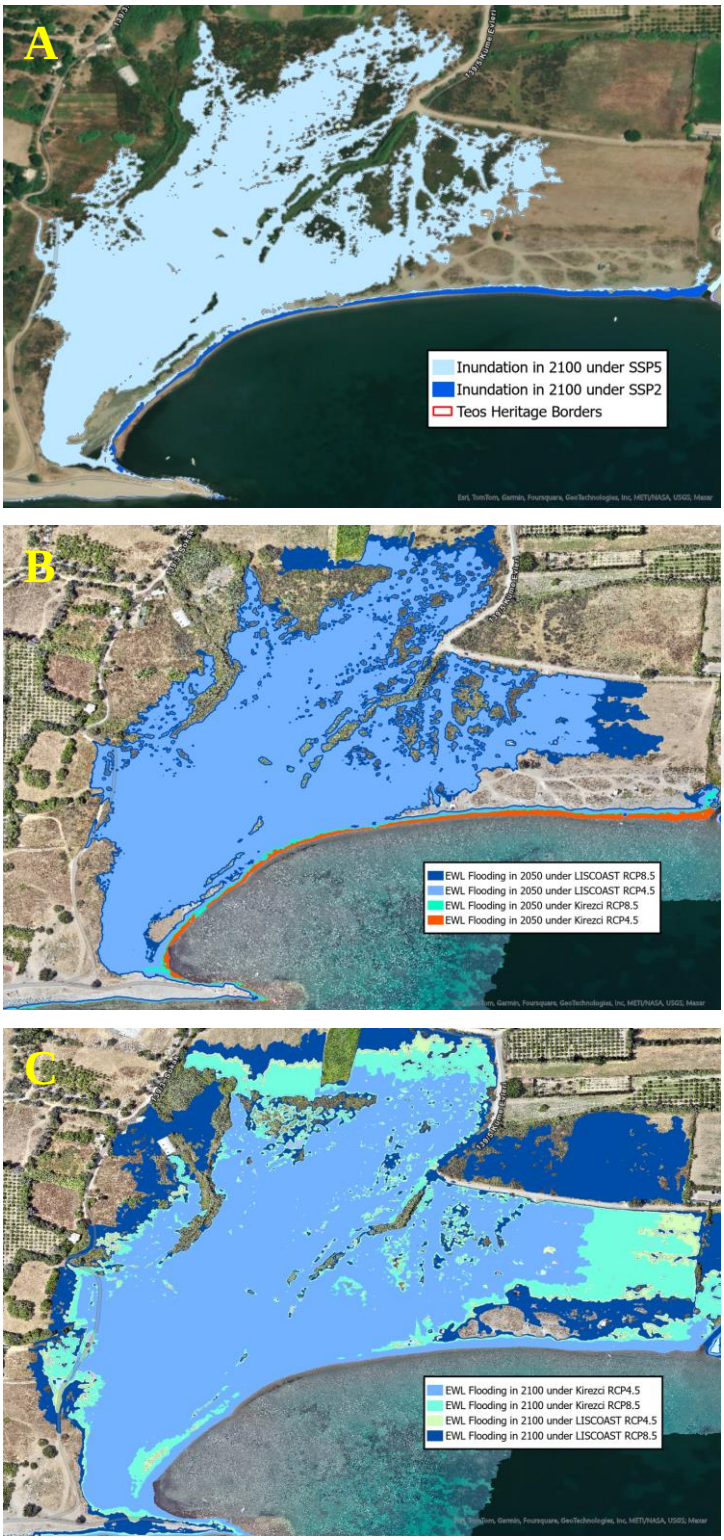



Figure 4.30 Teos sBTM Inundation and Flood Maps using UAV DTM (A: Inundation in 2100, B: Storm Surge Flooding in 2050, C: Storm Surge Flooding in 2100)

#### 4.4.4.2 eBTM

##### 4.4.4.2.1 GLO-30

The eBTM method for Teos showed good agreement with the sBTM method which was not the case for other sites. However, the differences between the cases are not consistent.

Table 4.19 Inundated and Flooded eBTM Areas of the Ancient City of Teos using GLO-30 (m2)

| | ***SSP2*** | ***SSP5*** | |
|---|---|---|---|
| Area Inundated by 2100 | *229006.08* ***(7.92%)*** | *243282.92* ***(8.41%)*** | |
| | ***LISCOAST*** | ***Kirezci*** | |
| *Area Flooded under EWL for 2050* | *255436.58* ***(8.83%)*** | *227515.02* ***(7.87%)*** | ***RCP4.5*** |
| | *332657.09* ***(11.5%)*** | *232010.25* ***(8.02%)*** | ***RCP8.5*** |
| *Area Flooded under EWL for 2100* | *367712.95* ***(12.7%)*** | *265922.71* ***(9.2%)*** | ***RCP4.5*** |
| | *441502.1* ***(15.3%)*** | *356143.67* ***(12.3%)*** | ***RCP8.5*** |

For the inundated areas in 2100, the results are almost the same with sBTM being slightly larger under SSP5. For the flooded areas in 2050, eBTM gave smaller areas for all the cases except for LISCOAST RCP8.5, where it is larger by approximately 2%. For the flooding in 2100, eBTM gave bigger results except for Kirezci RCP4.5. In terms of inundation and flood roots, sBTM and eBTM results gave agreeing results (Figure 4.31).

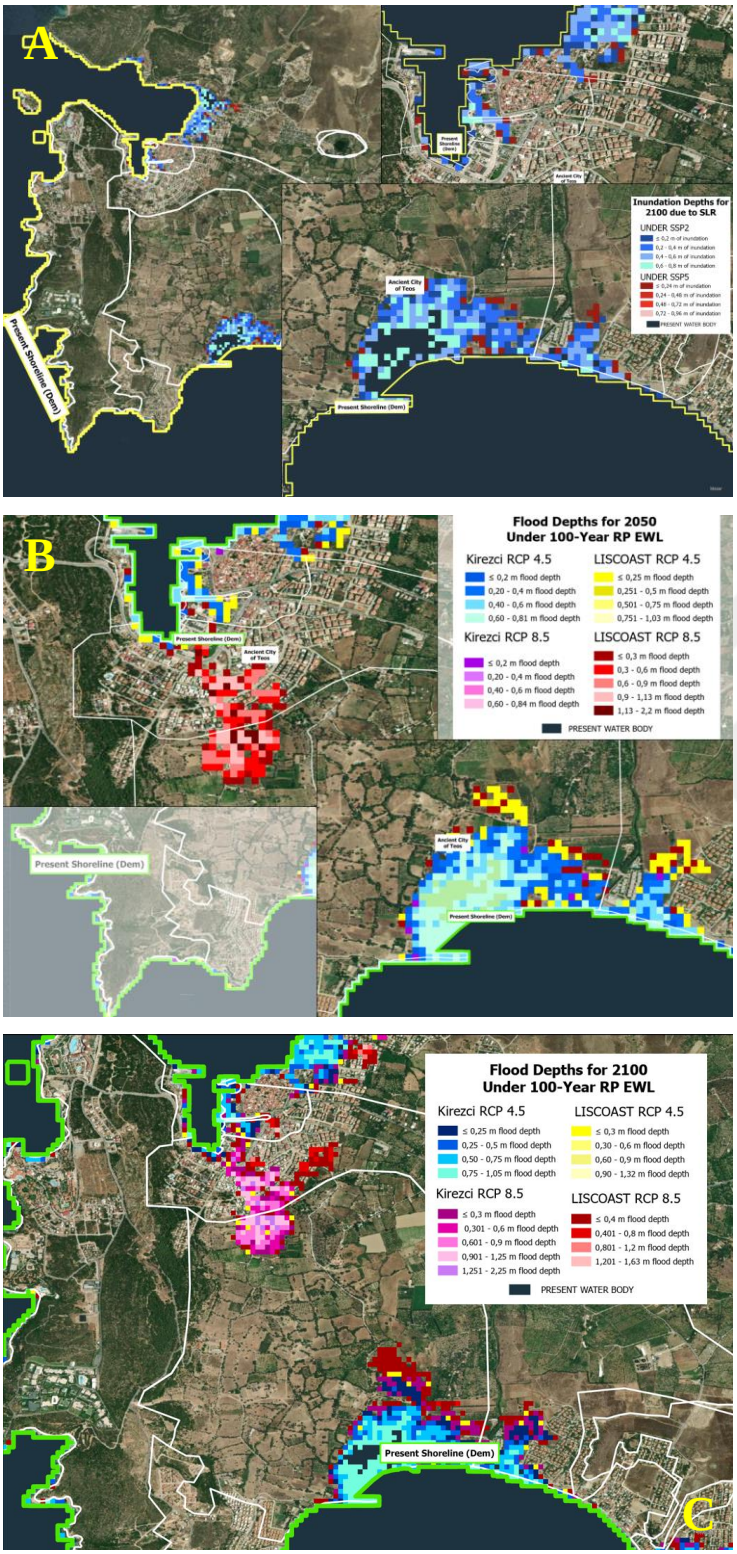



Figure 4.31Teos eBTM Inundation and Flood Maps using GLO-30 (A: Inundation in 2100, B: Storm Surge Flooding in 2050, C: Storm Surge Flooding in 2100)

#### 4.4.4.2.2 SYM-5

The eBTM application using SYM-5 elevation model resulted in very similar inundation areas. For SSP2, eBTM predicts a 300 $m^2$ larger area whereas for SSP5, the results are almost the same with a 40 $m^2$ difference. In case of extreme weather conditions in 2050, eBTM with SYM-5 also gives very limited flooding for Kirezci predictions (Table 4.20). For all the other scenarios, the difference with the sBTM method is less than 1%. When the results are compared with the eBTM method applied with GLO-30, the flooded areas are half as much in this resolution.

Table 4.20 Inundated and Flooded eBTM Areas of the Ancient City of Teos using SYM-5 ($m^2$)

| | ***SSP2*** | ***SSP5*** | |
|---|---|---|---|
| Area Inundated by 2100 | *9857.25* ***(0.34%)*** | *37688.23* ***(1.3%)*** | |
| | ***LISCOAST*** | ***Kirezci*** | |
| *Area Flooded under EWL for 2050* | *132832.18* ***(4.6%)*** | *10954* ***(0.38%)*** | ***RCP4.5*** |
| | *144895.6* ***(5%)*** | *11466.47* ***(0.4%)*** | ***RCP8.5*** |
| *Area Flooded under EWL for 2100* | *169019.33* ***(5.85%)*** | *137155.2* ***(4.74%)*** | ***RCP4.5*** |
| | *191326.26* ***(6.62%)*** | *164038.9* ***(5.67%)*** | ***RCP8.5*** |

Figure 4.32, Figure 4.33 and Figure 4.34 displays that the flood routes are correctly captured in this resolution. However as stated before, the model shoreline causes a slight difference behind the ancient breakwater. It is also seen in the figures that the ancient breakwater is partially flooded in 2050 and totally flooded in 2100.

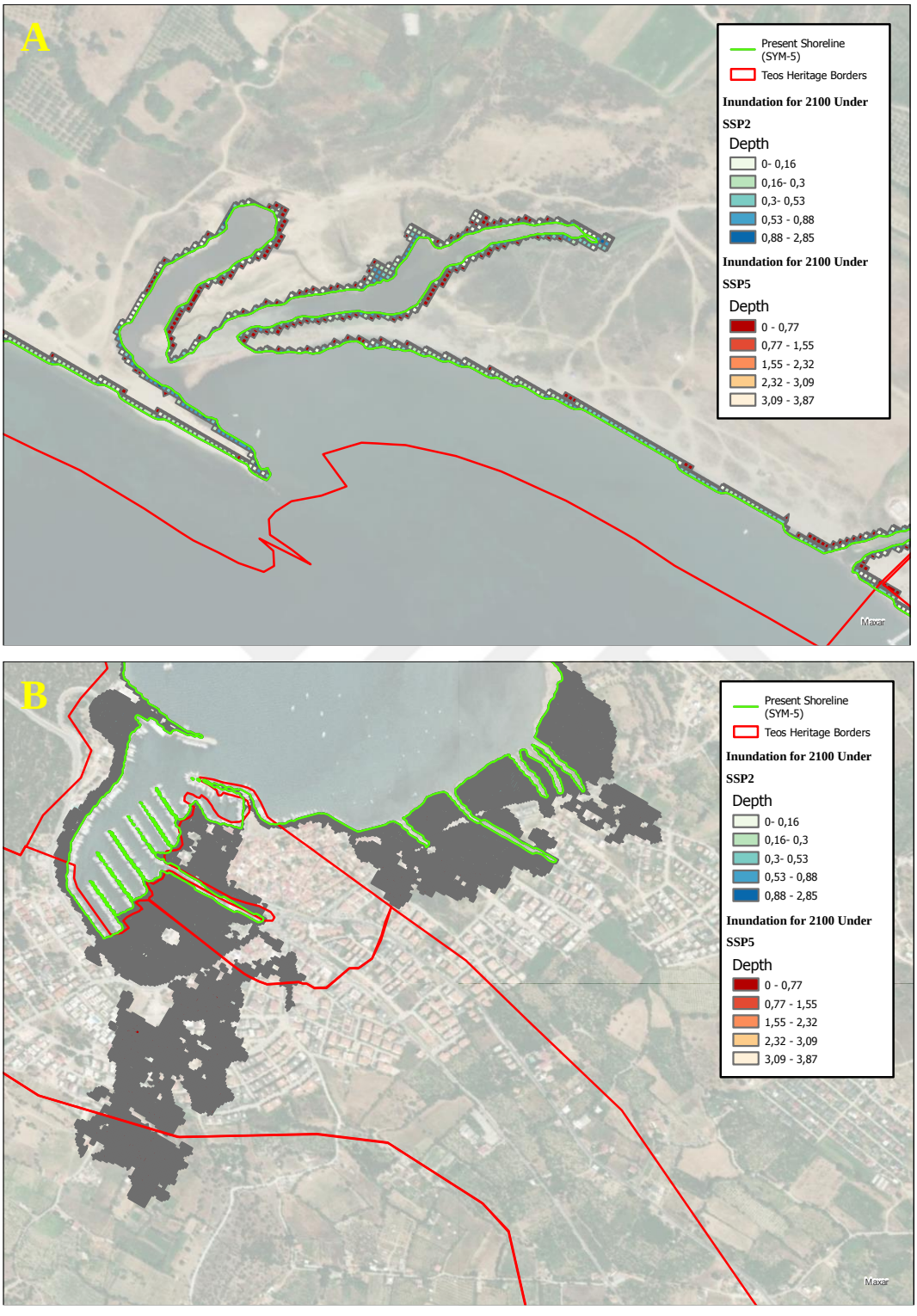



Figure 4.32 Teos eBTM Inundation Maps for 2100 using SYM-5 (A: Flooding from the Teos Marina (Ancient North Harbour), B: Flooding at the South Ancient Harbour)

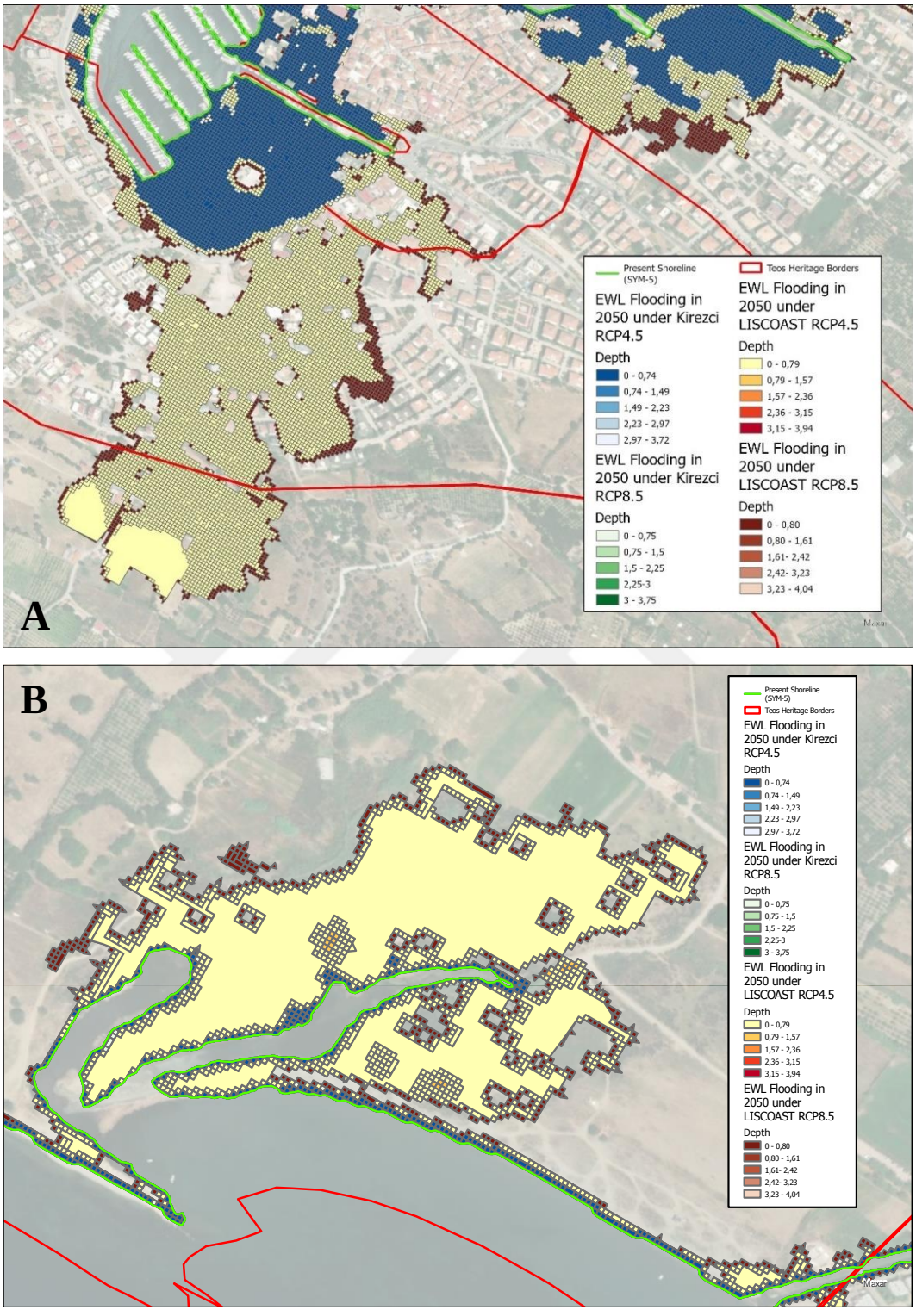



Figure 4.33 Teos eBTM Flooding Maps for 2050 using SYM-5 (A: Flooding from the Teos Marina (Ancient North Harbour), B: Flooding at the South Ancient Harbour)

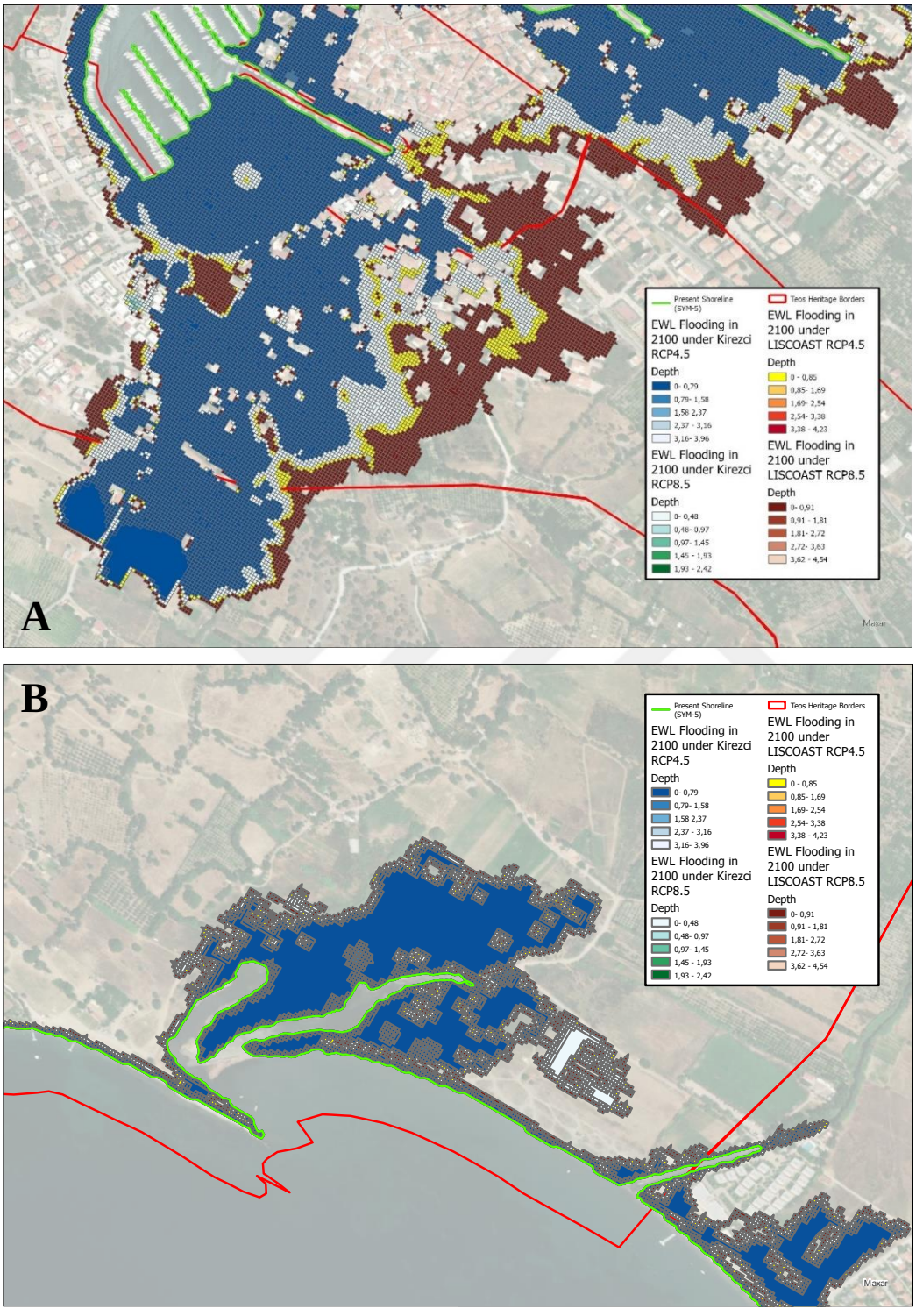



Figure 4.34 Teos eBTM Flooding Maps for 2100 using SYM-5 (A: Flooding from the Teos Marina (Ancient North Harbour), B: Flooding at the South Ancient Harbour)

#### 4.4.4.2.3 UAV

- **Digital Surface Model (DSM)**

When the resolution is further decreased and a 1 m resolution DSM is used, there is a decrease in the flooded areas, except for the inundation under SSP5. The model proves the limited inundation under SSP2 and flooding under Kirezci predictions for 2050, but the area under water is one-third of the one of SYM-5. In the other scenarios, the results are rather similar with differences of less than 1%. When compared to the sBTM method applied with the same DEM, the results are in really good agreement with only differences not exceeding 0.32%.

Table 4.21 Inundated and Flooded eBTM Areas of the Ancient City of Teos using UAV-DSM ($m^2$)

| | ***SSP2*** | ***SSP5*** | |
|---|---|---|---|
| Area Inundated by 2100 | *3109.3* ***(0.1%)*** | *81101.62* ***(2.8%)*** | |
| | ***LISCOAST*** | ***Kirezci*** | |
| *Area Flooded under EWL for 2050* | *94596* ***(3.27%)*** | *3229.79* ***(0.11%)*** | ***RCP4.5*** |
| | *105765.99* ***(3.66%)*** | *3729.41* ***(0.13%)*** | ***RCP8.5*** |
| *Area Flooded under EWL for 2100* | *145761.18* ***(5%)*** | *98281.36* ***(3.4%)*** | ***RCP4.5*** |
| | *198875.88* ***(6.88%)*** | *133983.41* ***(4.63%)*** | ***RCP8.5*** |

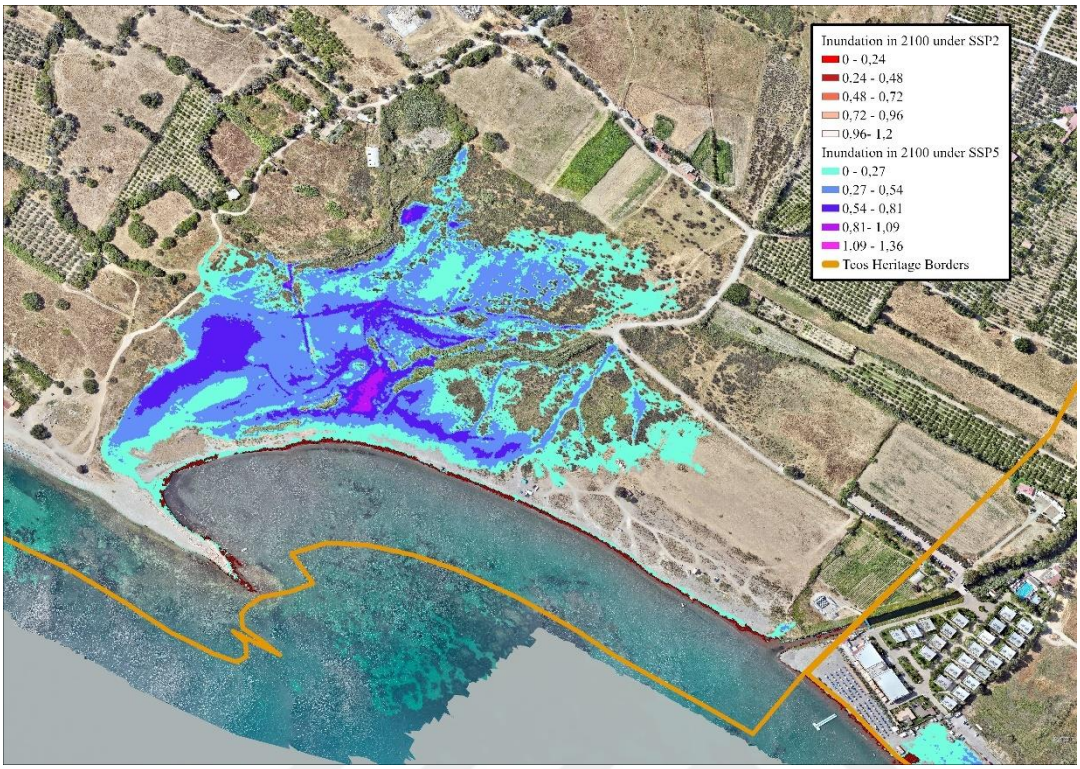



Figure 4.35 Teos eBTM Inundation Map for 2100 using UAV-DSM

In Figure 4.35, it is visible how small the inundation is under the SSP2 scenario. The figure differs from that of SYM-5 because of the shoreline difference. Under SSP5, the inundated area shows a drastic increase and further moves inland. The small pathways water will follow are clearer in this model, which might play a role in the conservation actions. In Figure 4.36, the EWL prediction datasets for 2050 are presented separately. There is a large difference between the two figures (Figure 4.36 A-B) although the predictions are for the same year. Like in the sBTM method, the flooding west to the ancient breakwater is not observable here. However, in Figure 4.37, under LISCOAST RCP8.5 conditions, the flooding connects to the sea from the west of the ancient breakwater.

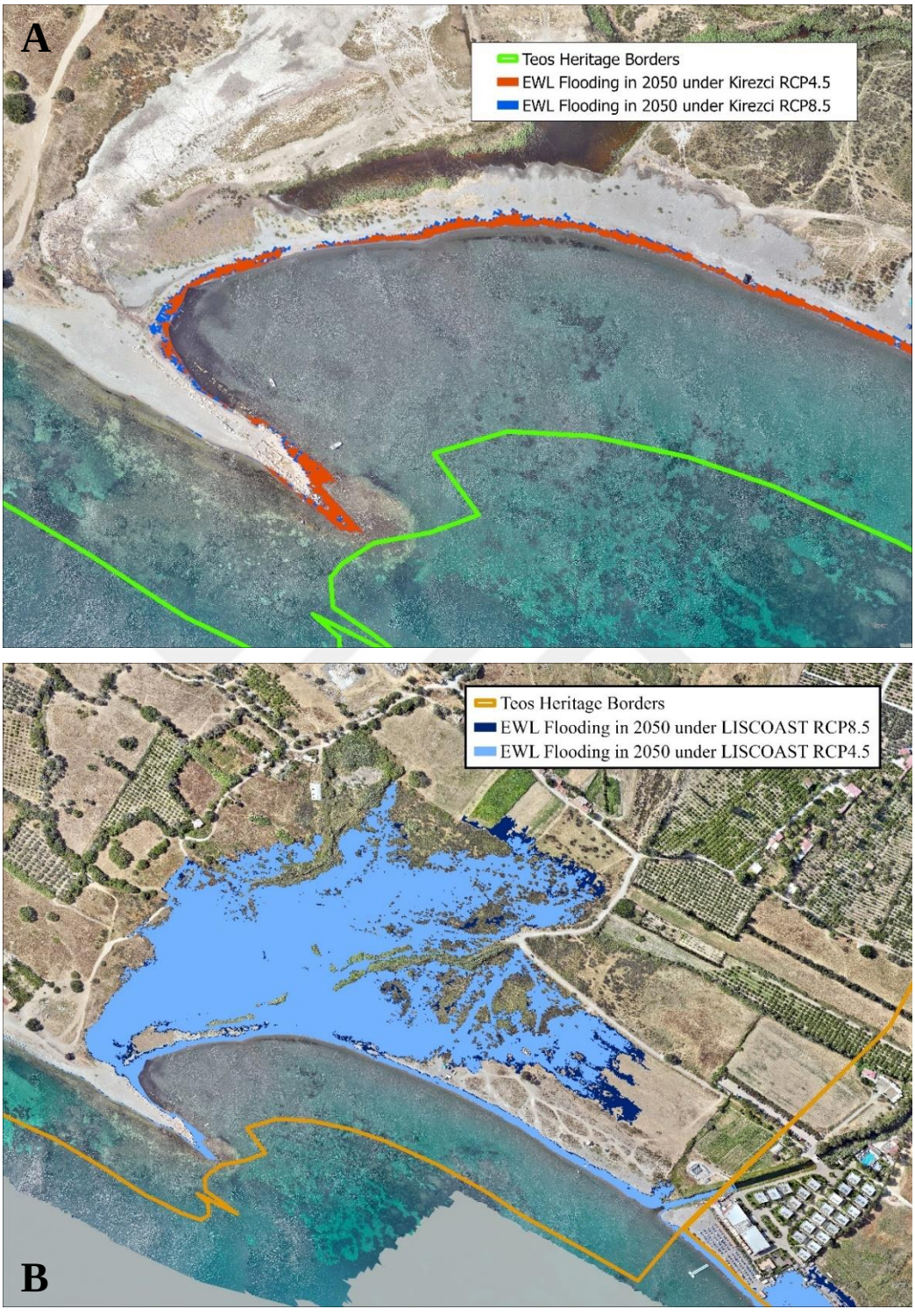



Figure 4.36 Teos eBTM Inundation Maps for 2050 using UAV-DSM (A: Kirezci Predictions, B: LISCOAST Predictions)

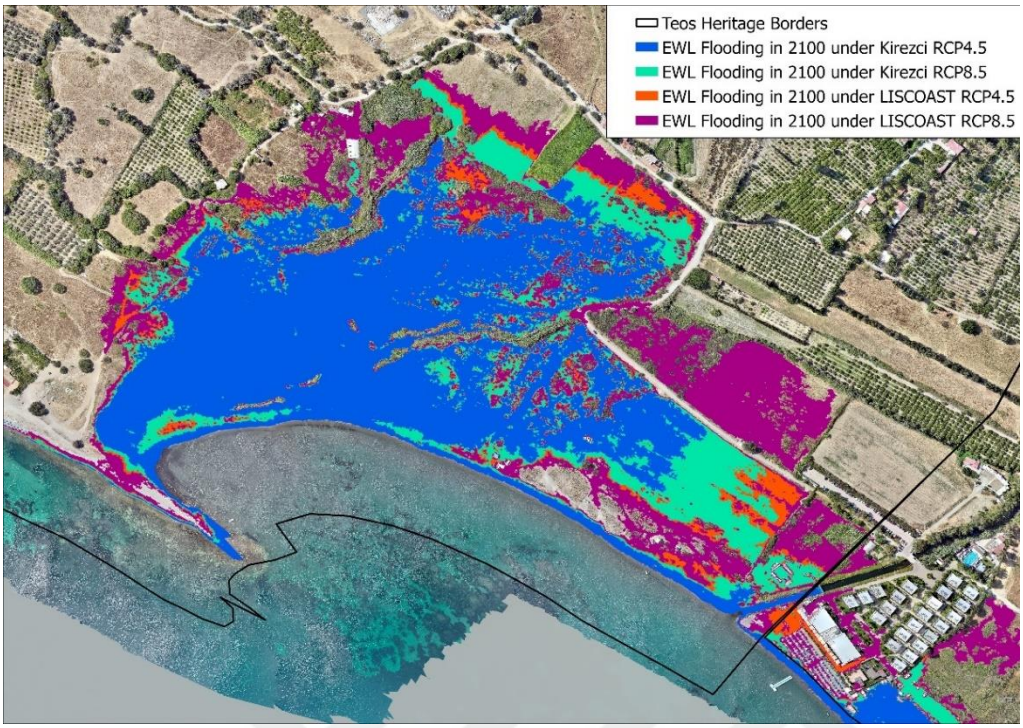



Figure 4.37 Teos eBTM Flooding Map for 2100 using UAV-DSM

❖ **Digital Terrain Model (DTM)**

Table 4.22 shows that the flood areas have slightly increased, which is expected. This slight increase is valid for all the cases of both inundation and EWL flooding. In Figure 4.36, Figure 4.37, and Figure 4.38, this slight difference is not visible.

Table 4.22 Inundated and Flooded eBTM Areas of the Ancient City of Teos using UAV-DTM ($m^2$)

| | ***SSP2*** | ***SSP5*** | |
|---|---|---|---|
| Area Inundated by 2100 | *3341.31* ***(0.12%)*** | *87445.66* ***(3.02%)*** | |
| | ***LISCOAST*** | ***Kirezci*** | |
| *Area Flooded under EWL for 2050* | *100128.47* ***(3.46%)*** | *3457.68* ***(0.12%)*** | ***RCP4.5*** |
| | *118085.43* ***(4.08%)*** | *4060.19* ***(0.14%)*** | ***RCP8.5*** |
| *Area Flooded under EWL for 2100* | *150466.61* ***(5.2%)*** | *103362.5* ***(3.58%)*** | ***RCP4.5*** |
| | *204534.68* ***(7.07%)*** | *138923.1* ***(4.8%)*** | ***RCP8.5*** |

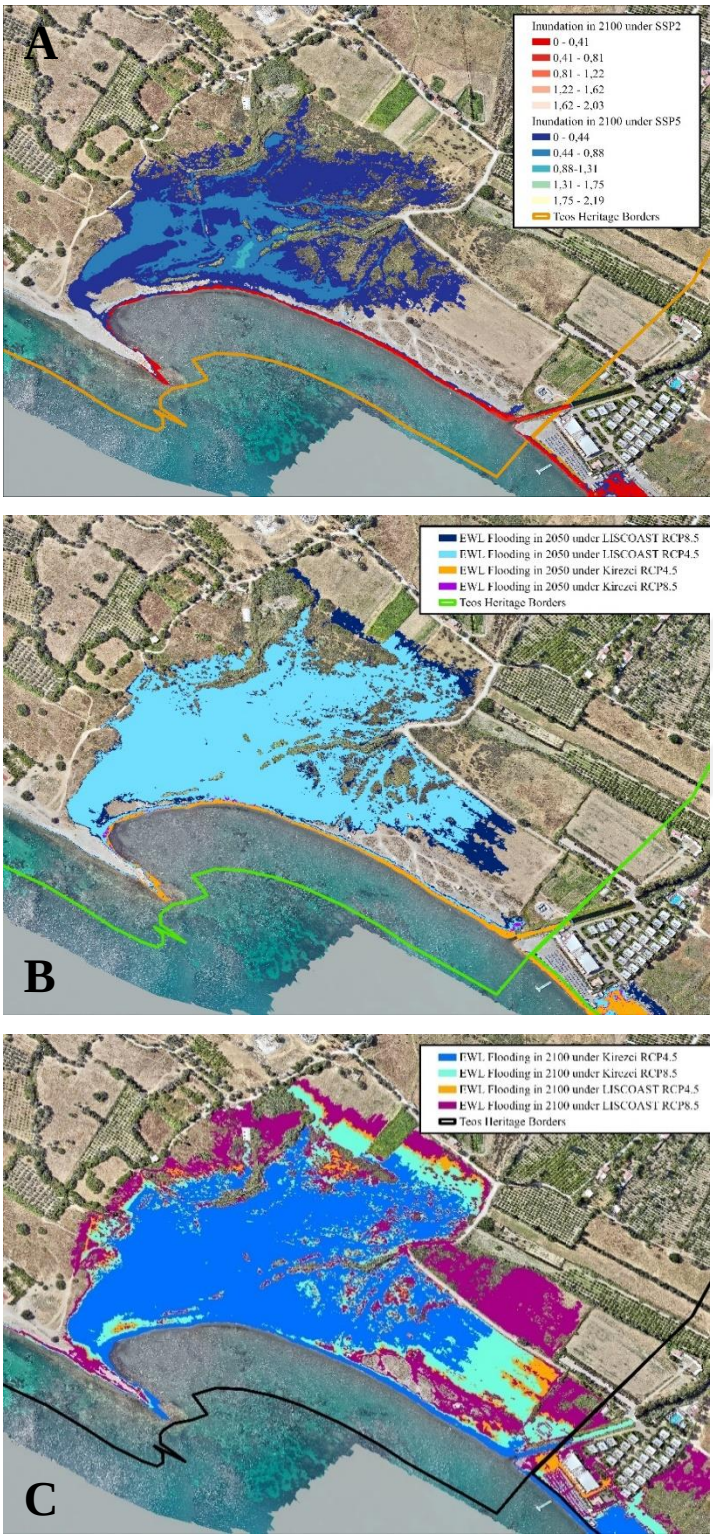



Figure 4.38 Teos eBTM Inundation and Flood Maps using UAV DTM (A: Inundation in 2100, B: Storm Surge Flooding in 2050, C: Storm Surge Flooding in 2100)

#### 4.4.4.3 Delft3D

As explained in the Methodology chapter, a historical storm and synthetic storm are modeled using Delft3D, aiming for the observation of the effects of a frequent storm that has a 5-year RP, both today and in 2100; and also, the results of an extreme event with 100-year RP in 2100.

The modeling of the storm that happened on January 6$^{th}$ 2012 resulted in the flood map shown in light blue in Figure 4.39. The flooded area under this storm is 7741.8 m$^2$. It is seen that the flooding happens mainly at the inner edges of the stream and slightly around the remains of the ancient breakwater. Since this is a frequent storm for the area, its effect under the future shoreline the SLR will form was modeled as well and given as the areas in dark blue.

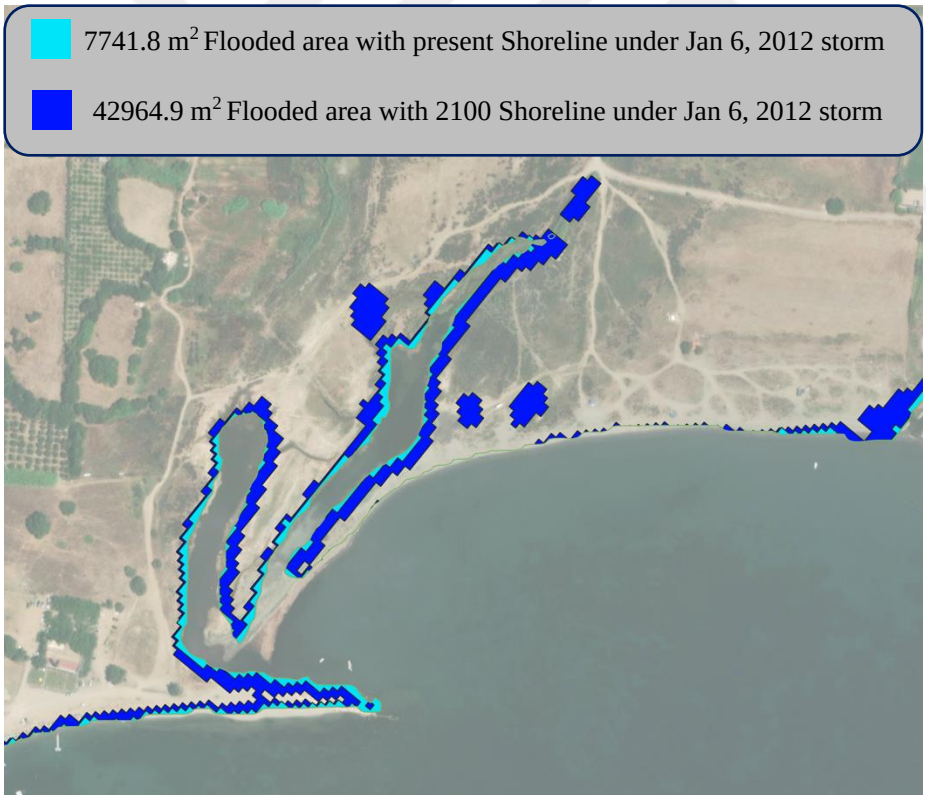



Figure 4.39 The Flood Map of January 6th, 2012 Storm with present Shoreline and 2100 shoreline under SSP5 SLR Projections (Light Blue: Under present shoreline, Dark Blue: Under 2100 shoreline)

The dark blue flood area shows that the remains of the ancient breakwater are almost completely flooded, and the water can pass over the breakwater. Water intrusion at the eastern border of the heritage site is observed and further intrusion from the waterway of the stream is shown. The flooded area is 42964.9 $m^2$ and it is almost 6 times the present flooded area.

Delft3D run of the 100-year RP storm event with SLR scenario of SSP5 projection resulted in the flood map shown in Figure 4.40. The flood route seems to be consistent with the GIS maps. West of the ancient breakwater is experiencing very little flooding, and the main inundation happens around the stream bed behind the ancient breakwater. The flooded area is 111016.35 $m^2$.

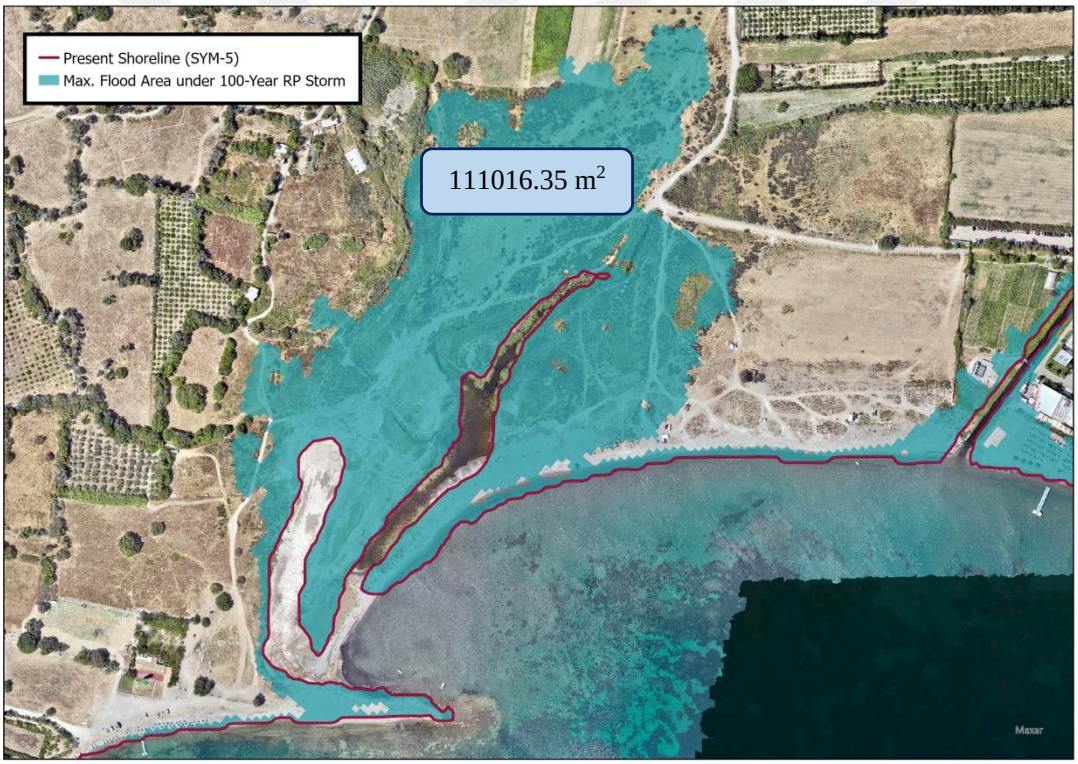



Figure 4.40 The Flood Map given by Delft3D Run for 100 RP synthetic storm with SLR scenario

# CHAPTER 5

# DISCUSSION

## 5.1 Aleksandria Troas

Analyzing the inundation and flood maps of Alexandria Troas and the areal information, it is seen that there is not much variation for sBTM and eBTM methods, both using the same DEM data. Especially in the SSP5 scenario, after the loss of the dune system behind the ancient breakwater and after the sea water merges with the lake, the amount of inundated area does not show large fluctuations. Even between the best-case scenario of 2050, Kirezci RCP4.5, and the worst-case scenario of 2100, LISCOAST RCP8.5, there is only a 0.5% (m2) difference. This means that after overwashing the dune system, the geomorphologic structure of Aleksandria Troas becomes relatively less vulnerable to sea level rise. In particular, the rapid cliff-like rise just behind the long sandy beach south of the city prevents further flooding of the area. The ancient breakwater, the only remnant on the coastal area, is inundated even with sea level rise under the SSP2 scenario. The pink lake, on the other hand, will definitely see interaction with seawater in the future, if not due to inundation, then certainly due to storm-induced flooding and the water quality of the lake will be lost. One main assumption for these discussions is that sedimentation in the region will remain as it is today. When the eBTM and sBTM methods are compared, it is observed that eBTM gives slightly larger values, but there is a good agreement between them. (Williams & Lück-Vogel, 2020) observed that the sBTM method overestimates the eBTM method, but in this study, where the raster resolution was very low, the eBTM method was found to give larger values. This slight overestimation may be due to the cellular calculation, which is the working principle of the eBTM method. Considering that the resolution of the DEM data used in this area is 30 m, such an overestimation is natural. Because if the raster height value is

below the EWL estimate value, the flood area increases by 900$m^2$ since a single value is assigned for an area of 900 $m^2$. The fact that the height values are so close as in the sBTM method can also be explained by the fact that the roughness value used is 1, which is recommended for smooth areas because the coastal area is a sandy beach.

## 5.2 Anemurium

The flood maps of Anemurium reveal that the flooding gets limited along the shoreline at Anemurium. This is due to the fast-inclining nature of the area and the berms formed at the beach. This can be seen from how close the SSP2 and SSP5 shorelines are to each other. However, the length of Anemurium's shoreline causes the inundation area to be large even though landward intrusion is limited. In addition, the flood area located to the east of the city occurs in a sandy area formed by a discharge pipe that was constructed and served as a groin, and in a small stream path slightly to the west of it, according to information obtained from the excavation director at the Anemuirum. However, since the shoreline provided by the GLO-30 DEM dataset does not cover this sandy area, the flood in this area has been overlooked. The most significant issue encountered in the flood maps created with the GLO-30 dataset has been the inaccuracy of the shoreline provided by this dataset. However, since it is believed that the dataset is internally consistent, it is thought that the deviation in the flood area information would be within reasonable degrees. The mentioned issues have been eliminated through UAV surveys conducted in the field. By obtaining a realistic shoreline, more accurate and precise flood maps have been produced. In the sBTM method, the UAV dataset yields flood area results that are half of those obtained from the GLO-30 dataset. The main reason for this is that the UAV survey does not cover the entire coastal area of the site. Due to technical reasons, the survey was conducted up to the groin-like structure. The ruins on the coast of Anemurium interact directly with seawater under the SSP2 scenario in 2100,

but this occurs earlier during extreme weather events in 2050. The flood map shows the remains that would need specific care.

Performing eBTM using GLO-30 for Anemurium resulted in larger flood area results than sBTM which is expected due to the resolution of the dataset.

## 5.3 Soli-Pompeipolis

In Soli-Pompeipolis, the inundation was most effective on the western side of the beach of the heritage site. Under both SSP2 and SSP5 scenarios, it is seen that the western breakwater is submerged, and the beach left is inundated. The accurate shoreline was a problem also for Soli-Pompeipolis. GLO-30 was not successful at capturing the abrupt shoreline changes that are present at Soli shores. On the east of the area, the flooding is very limited, which is due to the steep nature of the eastern beach. Between the eastern beach and the eastern breakwater, there is a pavement that is built later on for a parking lot and this lot causes a step in the elevation. According to results with GLO-30, the elevation does not change very much after the so-called beaches are flooded, and the shorelines predicted are very close to each other for every scenario. Only in the LISCOAST RCP8.5 scenario, there is a slight movement towards the parking lot's center. Knowing the layout of the ancient breakwater, it is evident that the area behind the parking lot used to be the inside of the harbor. As an area that is filled later on, this slight movement towards the center might be explained by the ancient layout of the location. When the resolution is increased to 1 m with the UAV-generated DSM model, a much more accurate result is obtained. First of all, the extent of flooded areas has decreased. This is probably due to the correction of the shoreline. The shoreline of GLO-30 is so deviated that it is a little bit further onto the sea area, which increases the area between the shoreline and the contour lines. Other than that, since the UAV-generated model is a surface model, the flood maps don't include surface elements, like the building on the western beach, which decreases the flood area. The UAV-DSM gives larger area only for a single case, which is the most critical case of LISCOAST RCP8.5. This is

clearly because of the layout again. It is seen in the flood map that water is able to pass to where once the inside of the harbor and fill that area. This behavior of this area was also validated by the excavation team of Soli-Pompeipolis. During field trips, questions regarding the storm and flood regimes of the area was investigated with the workers who remain on the site in winter months. They stated that the area which was flooded under LISCOAST RCP8.5 gets flooded during storms and forms this pool. They were not sure whether it was rain or the sea that filled the area, however, the flood maps show that the result is likely to happen because of the flooding from the sea in the future. The main assumption is again the shoreline will remain the same but increasing erosion of rising sea might make it easier for water to intrude to inside of the old harbour.

In terms of eBTM applications, the flooded areas increased with GLO-30, but a great agreement with sBTM results were obtained using UAV DSM. The overestimation with GLO-30 was observed for other areas as well and was related to the resolution of the elevation raster. eBTM and sBTM with this resolution were very similar and the intrusion to the old harbour area was successfully captured by the eBTM as well.

### 5.4 Teos

Teos is a much more complex heritage site than the others because of both the size of the area, the nature and geomorphology and the elevation models used in this study. First, this low laying area is full of neighboring heritage sites of different conservation level and type. The focus was on the first-degree conservation site of directly ancient city of Teos. Per my observations during the DSM generation, the nature of the area was different because it was founded on a land much lower than Anemurium and Aleksandria and wasn’t in contact with the city elements like Soli. Also, the geomorphology of the area had different dynamics which was visible from the dried out wetland near the shore and also from the interviews done with the archaeologists. The stream creating the wetland was completely dry and the shoreline was continuous during the generation, however, 5 m SYM shows that this is not

always the case. Another different challenge was that the city was open to inundation and flooding from two separate locations, one from the south and one from the north. An additional elevation model was available for Teos, which was obtained from the scope of another study and an addition was made with a terrain model generated by the UAV application.

The sBTM applications revealed once more that the GLO-30 dataset, when compared to SYM-5 and UAV-DSM models, overestimated the flood area. In every scenario of EWL and SLR, the water was able to flood the area behind the ancient breakwater in the south according to GLO-30. However, with SYM-5, SLR predictions for 2100 was not enough to inundate the area. Only inundation was observed around the shorelines and slightly on the ancient breakwater. This might be a result of the stream that flows into the sea right behind the breakwater. This location is a dynamic location where shoreline changes depending on the season and the month. During the site visit in July 2024, it was observed that the stream was completely dry, and the shoreline was continuous behind the breakwater, and this is also the case for GLO-30. However, SYM-5 was probably formed on a day when the flow of the stream was strong, and the mouth was completely open. This shows the changing nature of the location, and this dynamic might also be affecting the elevations along the stream and the shoreline, which prevented the inundation in SYM-5 case. Furthermore, UAV showed an in-between behavior. It showed inundation under SSP5 but almost no inundation under SSP2, which might indicate that the geomorphology was once again different than the other elevation models used in the study. The major limitation about Teos is the limited area of UAV-generated DEM. Since the area is too big and the location is prone to strong winds daily, the fieldwork got interrupted many times and certain challenges were faced regarding the UAV. The sBTM results showing a decreasing trend from GLO-30 to SYM-5 and then an increasing trend from SYM-5 to UAV DSM is explained with an outcome of the changing geomorphology of the region as well as possible uncertainty based on the data resolution. Considering SYM-5 has inundation through north and barely reaching the levels of inundation in the south harbor given by UAV

DSM shows that the difference is bigger, whereas UAV-DSM considering areas that is considered as a water body by SYM-5 as land is adding to this difference. It should also be noted that the north of the city is on the shore of a very sheltered bay, which means the bathtub model might not resemble the real life for this case as during a extreme weather, the wind, atmospheric pressure and surges have directions. In other words, even if a storm with 100-year RP is experienced by this site, it might not cause the same water level rise in the north and in the south.

- **DSM vs. DTM**

Finally, a comparison between the DSM and DTM models was available for this site. The DTM was generated from the DSM by using a tool to clean the surface items. The flooded areas increased when used a DTM, expectedly. Since the area is cleaned from trees, umbrellas, people and cars, areas that would normally be floodplains but seem to be safe from flooding due to the elevation of these items have been cleared. However, the difference is small as the focus is only on the ancient city part and these artificial elevations and items are limited here. Also, there are certain errors recognized in the DTM stemming from the algorithm that cleans the surface items.

## 5.5 sBTM vs eBTM

It was possible to compare these methods under different resolutions. When these methods are used with a low resolution DEMs, it is seen that eBTM gives larger flood areas. This can be linked to the cell system of eBTM method, because with GLO-30, a pixel accounts for the elevation of a 900 $m^2$ area. Accepting full flooding throughout the whole cell might be resulting this extra prediction. Furthermore, the since a historical storm is not modeled with this method, the methods can only be compared to each other. To find out which method gives the more realistic results require the data of a historical flooding event. However, since this is a consistent result for all four sites, it can be assumed that eBTM is the one overestimating. For 5 m resolution, this overestimation is again present however not as much as in 30 m

resolution. on the other hand, for 1 m resolution of DEM, sBTM starts to give larger flood areas. This is parallel with the results of the study of the creators of the eBTM method. Williams & Lück-Vogel, (2020), in a s study where they compared eBTM and sBTM methods using a 1 m resolution DSM elevation model, worked on a real flood case and validated with real data that sBTM method overestimates in this resolution. Showing agreement with the results of Williams & Lück-Vogel, (2020), 1 m resolution where sBTM tends to overestimate are the most realistic cases.

## 5.6 Bathtub Models vs Delft3D

For the Ancient City of Teos, the flooding in case of a 5-year RP and 100-year RP storms in 2100 was modeled with Delft3D. The resultant flood map with the 5-year RP storm shows that the ancient breakwater gets partially flooded in the present day and almost completely in 2100. Per the conversations with the excavation team in the site visit, this partial flooding is validated by them as there are witnesses who stated that the remains at the breakwater gets attacked by the waves and they even pass over it. With this information, complete submergence of the breakwater under a frequent storm in 2100 is expected. However, the flooded area becomes 111016.35 $m^2$ under an extreme event in 2100, which is smaller than both eBTM and sBTM maps using the same elevation model. This means that the static bathtub models tend to overestimate the flood areas. This outcome is also supported by Seenath et al. (2016) and Kumbier et al. (2019) who both stated that bathtub models amplify the flood plains. The reason behind this is the simple nature of bathtub modeling where the surface friction, hydraulic connectivity, wave-wave interactions are ignored and the difference between a long-term inundation and a rapid flood is not considered.

## 5.7 CVI

The CVI analysis resulted in all the study sites having moderate vulnerability against both inundation and flooding due to storm surges. The flood mapping concluded that

in the worst-case scenario, the land losses of these sites are, on average, around 10%. Considering this, moderate vulnerability given by CVI-SLR is a reasonable result. Moreover, in the range of moderate vulnerability, the most vulnerable one is Teos, which agrees with flood mapping results. As for the storm surge flooding Soli-Pompeipolis is the most vulnerable one. It is seen that the physical parameters of the sites that are inserted in the model don't vary that much. The difference in the vulnerabilities stem from the human influence parameters mainly. Even though CVI-SLR method doesn't provide spatial and depth information of inundation or flooding, it predicts the vulnerability in a fast and efficient way. This makes it preferable if the aim is a quick ranking and prioritizing of vulnerable sites.

## 5.8 Limitations

- Built-in Errors of DEMs

Digital Elevation Models (DEMs) form the basis of flood mapping and modeling, but their origin data and processing methods might give rise to inherent errors. The errors include improper dealize of natural forms like small depressions, steep slopes or artificial work that reflects the misrepresentation of hydrological process. E.g. smoothing during DEM generation could hide important features, such as coastal structures, levees or drainage network, directly influencing the flood extents. Errors in horizontal and vertical accuracy can also magnify inaccuracies in modeling water flow and flood extent.

- Unavailable Detailed DEM

For ¾ of the study sites, it was possible to capture a detailed DEM by UAV application. However, it was not possible to obtain the whole shoreline for Anemurium and Teos and a trip to Aleksandria Troas was not possible. This limited the generation of detailed maps for all of the sites.

- Resolution and Resolution-Sourced Assumptions

The resolution of a DEM is an important factor influencing the accuracy of flood modeling. High-resolution DEMs describe terrain information in high detail, but demand high computational cost, while low-resolution DEMs can be oversmooth the DEM, resulting in generalized or inaccurate predicted flood extent. Any assumptions made in order to adapt or interpolate between the different resolutions are another source of error, particularly when trying to merge datasets collected at different institutions. This acknowledges a compromise between computational tractability and the ability of the flood plain to represent spatial detail.

- Constant Shoreline Assumption

Flood modelling also typically assumes a static shoreline, which isn't realistic. Shorelines are not static; they are shaped by tides and wave action, as well as by storm surges that can vary widely from event to event over time. Thus, the exact shoreline position of the time for which the flood analysis is being done is crucial to know the real extent of the flooded area. In long term predictions like this study, the flooded areas might become a part of the sea due to erosiın. In such a case, the flooded area might be misleading.

- Ignoring Land Subsidence

Land subsidence from natural geological processes or human activities, such as groundwater extraction, also significantly drives flood and inundation vulnerability. Failure to account for this causes models to understate or overstate flood risk in sinking and elevating areas, respectively. In the long run land subsidence has the potential to worsen flood extents and intensities, so ignoring it is a very important omission that hampers the accurate formulation of long-term flood (coastal) impacts.

- Mistakes and Constraints in Extreme Water Level (EWL) Productions

Extreme Water Levels (EWL) have generally been generated by utilizing historical data, statistical models or hydrodynamic simulations which tend to introduce uncertainty. EWL predictions may contain sources of error arising from either a lack of historical records, an inadequacy in capturing evolving climatic conditions, or

oversimplification in the models of storm surge or wave-wave interactions. Its second part is propagated through calculation of flood models thereby compromising the quality of predictions regarding inundation extent and risk assessments.

# CHAPTER 6

# CONCLUSION

In this study, the inundation and flood vulnerability of four different heritage sites on the coasts of Türkiye has been analyzed using bathtub, hydrodynamic, and index-based methods. The different flood extents and maps these methods provide have been presented as the main results and the reasons behind them are investigated. Furthermore, using elevation models with different resolutions, the sensitivity of the methods has been investigated. The results are presented as inundated areas and flooded areas, where being inundated means the land is permanently underwater because of the sea level rise, and being flooded means a temporary wetting and submergence of land during a storm with 100-year RP. In the coming 4 pages, the inundated and flooded areas for the selected scenarios are given in $m^2$ and as the percentages of the heritage area in tables from Table 6.1 to Table 6.4.

Table 6.1 The Inundated and Flooded areas of Aleksandria Troas for different scenarios, databases, and years (Areas in m² and as percentages of the heritage site)

| | Flooding for 2100 | | | | Flooding for 2050 | | | | Inundation for 2100 | |
|---|---|---|---|---|---|---|---|---|---|---|
| **Dataset** | **LISCOAST** | | **Kirezci** | | **LISCOAST** | | **Kirezci** | | **IPCC AR6** | |
| **Scenario** | **RCP8.5** | **RCP4.5** | **RCP8.5** | **RCP4.5** | **RCP8.5** | **RCP4.5** | **RCP8.5** | **RCP4.5** | **SSP5** | **SSP2** |
| **sBTM** | 129232 m² **1.9%** | 115653 m² **1.7%** | 109232 m² **1.61%** | 100906 m² **1.48%** | 108784 m² **1.6%** | 102795 m² **1.51%** | 89312 m² **1.31%** | 87460 m² **1.29%** | 86205 m² **1.26%** | 53741 m² **0.79%** |
| **eBTM** | 145947 m² **2.15%** | 130736 m² **1.92%** | 127624 m² **1.88%** | 119023 m² **1.75%** | 127682 m² **1.88%** | 122420 m² **1.8%** | 111464 m² **1.64%** | 110322 m² **1.62%** | 112704 m² **1.66%** | 78007 m² **1.15%** |

Table 6.2 Inundated and Flooded areas of Soli Pompeipolis for different scenarios, databases, and years
(Areas in $m^2$ and as percentages of the heritage site)

| | | Flooding for 2100 | | | | Flooding for 2050 | | | | Inundation for 2100 | |
|---|---|---|---|---|---|---|---|---|---|---|---|
| | **Dataset** | **LISCOAST** | | **Kirezci** | | **LISCOAST** | | **Kirezci** | | **IPCC** | |
| | **Scenario** | **RCP8.5** | **RCP4.5** | **RCP8.5** | **RCP4.5** | **RCP8.5** | **RCP4.5** | **RCP8.5** | **RCP4.5** | **SSP5** | **SSP2** |
| **sBTM** | **GLO-30 30 m** | 50062 $m^2$ **9.2%** | 43229 $m^2$ **7.95%** | 43458 $m^2$ **8%** | 39216 $m^2$ **7.21%** | 39452 $m^2$ **7.25%** | 37299 $m^2$ **6.86%** | 34669 $m^2$ **6.37%** | 33778 $m^2$ **6.21%** | 36664 $m^2$ **6.74%** | 31129 $m^2$ **5.72%** |
| | **UAV-DSM 1 m** | 59984 $m^2$ **11.02%** | 31707 $m^2$ **5.83%** | 31843 $m^2$ **5.85%** | 27258 $m^2$ **5.01%** | 27446 $m^2$ **5.04%** | 25239 $m^2$ **4.64%** | 23000 $m^2$ **4.23%** | 22914 $m^2$ **4.21%** | 24289 $m^2$ **4.46%** | 18477 $m^2$ **3.4%** |
| **eBTM** | **GLO-30 30 m** | 54183 $m^2$ **9.96%** | 48820 $m^2$ **8.97%** | 48823 $m^2$ **8.97%** | 40055 $m^2$ **7.36%** | 40053 $m^2$ **7.36%** | 39288 $m^2$ **7.22%** | 36254 $m^2$ **6.66%** | 34700 $m^2$ **6.38%** | 38477 $m^2$ **7.07%** | 32400 $m^2$ **5.95%** |
| | **UAV-DSM 1 m** | 59794 $m^2$ **11%** | 31717 $m^2$ **5.83%** | 31844 $m^2$ **5.85%** | 27250 $m^2$ **5.01%** | 27411 $m^2$ **5.04%** | 25231 $m^2$ **4.64%** | 22797 $m^2$ **4.19%** | 21843 $m^2$ **4.01%** | 24472 $m^2$ **4.5%** | 18408 $m^2$ **3.38%** |

Table 6.3 Inundated and Flooded areas of Anemurium for different scenarios, databases and years
(Areas in m² and as percentages of the heritage site)

| | | **Flooding for 2100** | | | | **Flooding for 2050** | | | | **Inundation for 2100** | |
|---|---|---|---|---|---|---|---|---|---|---|---|
| | **Dataset** | **LISCOAST** | | **Kirezci** | | **LISCOAST** | | **Kirezci** | | **IPCC** | |
| | **Scenario** | **RCP8.5** | **RCP4.5** | **RCP8.5** | **RCP4.5** | **RCP8.5** | **RCP4.5** | **RCP8.5** | **RCP4.5** | **SSP5** | **SSP2** |
| **sBTM** | **GLO-30 30 m** | 95581 m² **4.66%** | 82113 m² **4%** | 88794 m² **4.33%** | 78069 m² **3.8%** | 72897 m² **3.55%** | 70389 m² **3.43%** | 68716 m² **3.35%** | 67475 m² **3.29%** | 63672 m² **3.1%** | 53229 m² **2.59%** |
| | **UAV-DSM 1 m** | 46227 m² **2.25%** | 36760 m² **1.79%** | 40497 m² **1.97%** | 34274 m² **1.67%** | 31397 m² **1.53%** | 29275 m² **1.43%** | 28502 m² **1.39%** | 27793 m² **1.35%** | 25842 m² **1.26%** | 18597 m² **0.91%** |
| **eBTM** | **GLO-30 30 m** | 106109 m² **5.17%** | 98233 m² **5.85%** | 100287 m² **4.89%** | 93603 m² **4.79%** | 88725 m² **4.32%** | 85639 m² **4.17%** | 84951 m² **4.14%** | 84951 m² **4.14%** | 82618 m² **4.03%** | 77586 m² **3.78%** |
| | **UAV-DSM 1 m** | 43058 m² **2.1%** | 34935 m² **1.7%** | 38331 m² **1.87%** | 32881 m² **1.6%** | 30127 m² **1.47%** | 28994 m² **1.41%** | 28286 m² **1.38%** | 27585 m² **1.34%** | 25685 m² **1.25%** | 18866 m² **0.92%** |

Table 6.4 Inundated and Flooded areas of Teos for different scenarios, databases and years

| | | | Flooding for 2100 | | | | Flooding for 2050 | | | | Inundation for 2100 | |
|---|---|---|---|---|---|---|---|---|---|---|---|---|
| | Dataset | | LISCOAST | | Kirezci | | LISCOAST | | Kirezci | | IPCC | |
| | Scenario | | RCP8.5 | RCP4.5 | RCP8.5 | RCP4.5 | RCP8.5 | RCP4.5 | RCP8.5 | RCP4.5 | SSP5 | SSP2 |
| sBTM | GLO-30 30 m | | 373956 m² **12.93%** | 312302 m² **10.8%** | 302003 m² **10.44%** | 267940 m² **9.27%** | 282407 m² **9.77%** | 265356 m² **9.18%** | 233537 m² **8.08%** | 230146 m² **7.96%** | 247069 m² **8.54%** | 228972 m² **7.92%** |
| | SYM-5 5 m | | 187282 m² 0.**48%** | 166324 m² **5.75%** | 160739 m² **5.56%** | 131454 m² **4.55%** | 144185 m² **4.99%** | 127595 m² **4.41%** | 10478 m² **0.36%** | 9771 m² **0.34%** | 37641 m² **1.3%** | 9565 m² **0.33%** |
| | 1 m UAV | DSM | 202903 m² **7.02%** | 152374 m² **5.27%** | 140817 m² **4.87%** | 107258 m² **3.72%** | 107499 m² **3.72%** | 94713 m² **3.28%** | 3931 m² 0.**14%** | 3361 m² **0.12%** | 80633 m² **2.79%** | 3219 m² **0.11%** |
| | | DTM | 205128 m² **7.09%** | 155702 m² **5.38%** | 141086 m² **4.87%** | 110731 m² **4.05%** | 108843 m² **3.76%** | 92735 m² **3.2%** | 3934 m² **0.14%** | 3441 m² 0.**12%** | 86691 m² **3%** | 3442 m² **0.11%** |
| eBTM | GLO-30 30 m | | 441502 m² **15.3%** | 367713 m² **12.7%** | 356144 m² **12.3%** | 265923 m² **9.2%** | 332657 m² **11.5%** | 255437 m² **8.83%** | 232010 m² **8.02%** | 227515 m² **7.87%** | 243283 m² **8.41%** | 229006 m² **7.92%** |
| | SYM-5 5 m | | 191326 m² **6.62%** | 169019 m² **5.85%** | 164039 m² **5.67%** | 137155 m² **4.74%** | 144896 m² **5%** | 132832 m² **4.6%** | 111466 m² **0.4%** | 10954 m² **0.38%** | 37688 m² **1.3%** | 9857 m² **0.34%** |
| | 1 m UAV | DSM | 198876 m² **6.88%** | 145761 m² **5%** | 133983 m² **4.64%** | 98281 m² **3.4%** | 105766 m² **3.66%** | 94596 m² **3.27%** | 3729 m² **0.13%** | 3230 m² 0.**11%** | 81102 m² **2.8%** | 3109 m² **0.1%** |
| | | DTM | 204535 m² **7.07%** | 150467 m² **5.2%** | 138923 m² **4.8%** | 103363 m² **3.58%** | 118085 m² **4.08%** | 100128 m² **3.46%** | 4060 m² **0.14%** | 3458 m² **0.12%** | 87446 m² **3.02%** | 3341 m² **0.12%** |

- By 2100, flooded areas increase across all scenarios, with LISCOAST producing larger estimates than Kirezci, and GLO-30 consistently yielding higher values than UAV DSM.
- Across all resolutions and methods, GLO-30 provides the highest estimates, while UAV-DSM yields the lowest, reflecting the influence of resolution in flood risk assessment. LISCOAST consistently predicts larger flooded areas than Kirezci, while eBTM generally produces higher estimates than sBTM. These findings underline the critical role of resolution, methodology, and model in assessing inundation and flooding risks for the ancient city of Teos
- Teos and Soli-Pompeipolis are the most vulnerable sites against flooding and surge flooding, respectively according to CVI-SLR.
- eBTM and sBTM methods consistency is dependent on the resolution of the elevation model. In lower resolutions, eBTM gives remarkably larger flood areas than sBTM, whereas with high resolutions, sBTM starts to overestimate. The method selection should be made depending on the DEM resolution.
- Using whether a DSM or a DTM for a flood modeling is a matter of tradeoff. If the water-surface elements interaction is of importance and aimed to be modeled then DSM should be used, however, the area will have point clouds that present unrealistic non-flooded areas like cars, umbrellas, and trees. If a DTM is used, then the element interaction is lost and the water paths might be distorted as an element that will direct the water won't be available.
- Bathtub models tend to overestimate the floodplain compared to hydrodynamic models as they ignore coastal dynamics. However, if the interest is in multiple locations, bathtub models give good results in a shorter time, with the need of less preparation whereas hydrodynamic models require both longer preprocessing, longer runtime and longer postprocessing.
- The CVI-SLR method is a handy tool to compare and rank multiple areas at once in terms of vulnerability in a rapid way with minimal preparation.

However, it does not offer any numerical information about the flooded or inundated area extents.

As expected in long-term flood studies, elevation data is the key data. Vertical ground motions should be included in the studies and reference elevation should be found. If a single area is to be studied, it would be most logical to use the hydrodynamic method to analyze the flood generation and propagation along the land in detail. However, if a fast analysis is needed or the flood situation of multiple areas is to be evaluated, bathtub models can be used. In fact, using eBTM will be much more feasible and accurate both in terms of including roughness and providing hydraulic connectivity. If the aim is to compare and prioritize more than one area rather than finding out how many flood areas there are, index-based models can be used

**Recommendations for Future Work**

One of the biggest limitations of this study is the avoidance of vertical land movement. Inclusion of such data would give more accurate and realistic results in the future. The characteristics and pace of climate change is constantly changing, and the projections might differ. It is an expected change that the return period calculation might change in the future and the 100-year RP storms might not be valid and require re-calculation in the future. Moreover, as these sites go under excavation work, the DEM to be used in the flood analysis must be updated. For the vulnerability calculations, the method used can predict the vulnerability, however, a more comprehensive vulnerability model would be more appropriate as these sites might require additional parameters to account for vulnerability. Furthermore, a detailed analysis after a storm the area has experienced might reveal additional parameters or might present ways to validate the study. This was not possible for this study but is highly recommended for future work.

## REFERENCES


Aisjah, A., Arifin, S., & Danistha, W. (2016). Sverdruv Munk Bretschneider Modification (SMB) for Significant Wave Height Prediction in Java Sea. *British Journal of Applied Science & Technology*, *16*(2), 1–8. https://doi.org/10.9734/BJAST/2016/19669

Anzidei, M., Doumaz, F., Vecchio, A., Vecchio, A., Vecchio, A., Serpelloni, E., Pizzimenti, L., Civico, R., Greco, M., Martino, G., Enei, F., Flavio Enei, & Flavio Enei. (2020). Sea Level Rise Scenario for 2100 A.D. in the Heritage Site of Pyrgi (Santa Severa, Italy). *Journal of Marine Science and Engineering*, *8*(2), 64. https://doi.org/10.3390/jmse8020064

Barnard, P. L., Erikson, L. H., Foxgrover, A. C., Hart, J. A. F., Limber, P., O'Neill, A. C., Van Ormondt, M., Vitousek, S., Wood, N., Hayden, M. K., & Jones, J. M. (2019). Dynamic flood modeling essential to assess the coastal impacts of climate change. *Scientific Reports*, *9*(1), 4309. https://doi.org/10.1038/s41598-019-40742-z

Bates, P. D., Dawson, R. J., Hall, J. W., Horritt, M. S., Nicholls, R. J., Wicks, J., & Mohamed Ahmed Ali Mohamed Hassan. (2005). Simplified two-dimensional numerical modelling of coastal flooding and example applications. *Coastal Engineering*, *52*(9), 793–810. https://doi.org/10.1016/j.coastaleng.2005.06.001

C3S. (2018). *ERA5 hourly data on single levels from 1940 to present* [Dataset]. Copernicus Climate Change Service (C3S) Climate Data Store (CDS). https://doi.org/10.24381/CDS.ADBB2D47

Calvin, K., Dasgupta, D., Krinner, G., Mukherji, A., Thorne, P. W., Trisos, C., Romero, J., Aldunce, P., Barrett, K., Blanco, G., Cheung, W. W. L., Connors, S., Denton, F., Diongue-Niang, A., Dodman, D., Garschagen, M., Geden, O., Hayward, B., Jones, C., … Péan, C. (2023). *IPCC, 2023: Climate Change 2023: Synthesis Report. Contribution of Working Groups I, II and III to the Sixth Assessment Report of the Intergovernmental Panel on Climate Change [Core Writing Team, H. Lee and*

*J. Romero (eds.)]. IPCC, Geneva, Switzerland.* (First). Intergovernmental Panel on Climate Change (IPCC). https://doi.org/10.59327/IPCC/AR6-9789291691647

Carneiro-Barros, J. E., Plomaritis, T. A., Fazeres-Ferradosa, T., Rosa-Santos, P., & Taveira-Pinto, F. (2023). Coastal Flood Mapping with Two Approaches Based on Observations at Furadouro, Northern Portugal. *Remote Sensing*, *15*(21), 5215. https://doi.org/10.3390/rs15215215

Copernicus Climate Change Service. (2022). *Global sea level change time series from 1950 to 2050 derived from reanalysis and high resolution CMIP6 climate projections* [Dataset]. ECMWF. https://doi.org/10.24381/CDS.A6D42D60

Dogan, G. G., Yalciner, A. C., Yuksel, Y., Ulutaş, E., Polat, O., Güler, I., Şahin, C., Tarih, A., & Kânoğlu, U. (2021). The 30 October 2020 Aegean Sea Tsunami: Post-Event Field Survey Along Turkish Coast. *Pure and Applied Geophysics*, *178*(3), 785–812. https://doi.org/10.1007/s00024-021-02693-3

Duo, E., Sanuy, M., Jiménez, J. A., & Ciavola, P. (2020). How good are symmetric triangular synthetic storms to represent real events for coastal hazard modelling. *Coastal Engineering*, *159*, 103728. https://doi.org/10.1016/j.coastaleng.2020.103728

European Environment Agency. (2020). *Coastal Zones Land Cover/Land Use 2018 (vector), Europe, 6-yearly, Feb. 2021* (Version 01.00) [Geopackage]. European Environment Agency. https://doi.org/10.2909/205E2DB2-4E35-4B1B-BF84-271C4A82248C

European Space Agency & Airbus. (2022). *Copernicus DEM* [Dataset]. https://doi.org/10.5270/ESA-c5d3d65

Flick, R. E., Chadwick, D. B., Briscoe, J., & Harper, K. C. (2012). "Flooding" versus "inundation". *Eos, Transactions American Geophysical Union*, *93*(38), 365–366. https://doi.org/10.1029/2012EO380009

Garner, A. J., Weiss, J. L., Parris, A., Kopp, R. E., Horton, R. M., Overpeck, J. T., & Horton, B. P. (2018). Evolution of 21st Century Sea Level Rise Projections. *Earth's Future*, *6*(11), 1603–1615. https://doi.org/10.1029/2018EF000991

Google Earth. (2024) Satellite Images. Retrieved in June, 2024 from Google Earth Pro

Gornitz, V. (1991). Global coastal hazards from future sea level rise. *Palaeogeography, Palaeoclimatology, Palaeoecology*, *89*(4), 379–398. https://doi.org/10.1016/0031-0182(91)90173-O

Gornitz, V., Lebedeff, S., & Hansen, J. (1982). Global Sea Level Trend in the Past Century. *Science*, *215*(4540), 1611–1614. https://doi.org/10.1126/science.215.4540.1611

Hinkel, J., & Klein, R. (2006). *Integrating knowledge for assessing coastal vulnerability to climate change* (pp. 61–77).

Jafarzadegan, K., Muñoz, D. F., Moftakhari, H., Gutenson, J. L., Savant, G., & Moradkhani, H. (2022). Real-time coastal flood hazard assessment using DEM-based hydrogeomorphic classifiers. *Natural Hazards and Earth System Sciences*, *22*(4), 1419–1435. https://doi.org/10.5194/nhess-22-1419-2022

Jisan, M. A., Bao, S., & Pietrafesa, L. J. (2018). Ensemble projection of the sea level rise impact on storm surge and inundation at the coast of Bangladesh. *Natural Hazards and Earth System Sciences*, *18*(1), 351–364. https://doi.org/10.5194/nhess-18-351-2018

Kasmalkar, I., Wagenaar, D., Bill-Weilandt, A., Choong, J., Manimaran, S., Lim, T. N., Rabonza, M., & Lallemant, D. (2024). Flow-tub model: A modified bathtub flood model with hydraulic connectivity and path-based attenuation. *MethodsX*, *12*, 102524. https://doi.org/10.1016/j.mex.2023.102524

Kirezci, E., Young, I. R., Ranasinghe, R., Muis, S., Nicholls, R. J., Lincke, D., & Hinkel, J. (2020). Projections of global-scale extreme sea levels and resulting

episodic coastal flooding over the 21st Century. *Scientific Reports*, *10*(1), 11629. https://doi.org/10.1038/s41598-020-67736-6

Kösem, İ., Özyurt Tarakcıoğlu, G., Ergin, A., Uysal, A. Ç., İnce, A., Yalçıner, A. C., Erciyas, D. B., Varınlıoğlu, G., Süzen, M. L., & Çalışkan, U. (2023). *Türkiye Kıyı Alanlarında Bulunan Doğal ve Arkeolojik Sit Alanlarında İklim Değişikliği ve Kıyı Erozyonu*. 10. Kıyı Mühendisliği Sempozyumu.

Kumbier, K., Carvalho, R. C., Vafeidis, A. T., & Woodroffe, C. D. (2019). Comparing static and dynamic flood models in estuarine environments: A case study from south-east Australia. *Marine and Freshwater Research*, *70*(6), 781. https://doi.org/10.1071/MF18239

Lauren Lyn Williams. (2019). *Coastal Inundation (Enhanced Bathtub Model (eBTM))* [Dataset]. Department of Environment, Forestry and Fisheries. https://doi.org/10.15493/DEFF.10000002

Leon, J. X., Heuvelink, G. B. M., & Phinn, S. R. (2014). Incorporating DEM Uncertainty in Coastal Inundation Mapping. *PLoS ONE*, *9*(9), e108727. https://doi.org/10.1371/journal.pone.0108727

Lewis, M., Horsburgh, K., Bates, P., & Smith, R. (2011). Quantifying the Uncertainty in Future Coastal Flood Risk Estimates for the U.K. *Journal of Coastal Research*, *276*, 870–881. https://doi.org/10.2112/JCOASTRES-D-10-00147.1

Muñoz, D. F., Moftakhari, H., & Moradkhani, H. (2020). Compound Effects of Flood Drivers and Wetland Elevation Correction on Coastal Flood Hazard Assessment. *Water Resources Research*, *56*(7), e2020WR027544. https://doi.org/10.1029/2020WR027544

Özyurt, G. (2007). *Vulnerability of coastal areas to sea level rise: A case study on Goksu Delta* [M.Sc., Middle East Technical University]. https://catalog.library.metu.edu.tr/search~S4?/XG{u00FC}lizar&searchscope=4&SORT=DZ/XG{u00FC}lizar&searchscope=4&SORT=DZ&extended=0&SUBKEY

=Gülizar/1%2C33%2C33%2CB/frameset&FF=XG{u00FC}lizar&searchscope=4&SORT=DZ&25%2C25%2C

Perez-Alvaro, E. (2016). Climate change and underwater cultural heritage: Impacts and challenges. *Journal of Cultural Heritage*, *21*, 842–848. https://doi.org/10.1016/j.culher.2016.03.006

Poulter, B., & Halpin, P. N. (2008). Raster modelling of coastal flooding from sea-level rise. *International Journal of Geographical Information Science*, *22*(2), 167–182. https://doi.org/10.1080/13658810701371858

Pugh, D. T. (1996). *Tides, surges and mean sea-level (reprinted with corrections)*.

Ravanelli, R., Crespi, M., Nigro, L., Spagnoli, F., Anzidei, M., Riguzzi, F., Vecchio, A., Vecchio, A., Antonio Vecchio, & Vecchio, A. (2019). Sea level rise scenario for 2100 AD for the archaeological site of Motya. *Rendiconti Lincei-Scienze Fisiche E Naturali*, *30*(4), 747–757. https://doi.org/10.1007/s12210-019-00835-3

Reimann, L., Vafeidis, A. T., Brown, S., Hinkel, J., & Tol, R. S. J. (2018). Mediterranean UNESCO World Heritage at risk from coastal flooding and erosion due to sea-level rise. *Nature Communications*, *9*(1), 4161–4161. https://doi.org/10.1038/s41467-018-06645-9

Russell, J. (1976). EXCAVATIONS AT ANEMURIUM ESKİ ANAMUR 1974. *Türk Arkeoloji Dergisi*, *39*, 96–101.

Seenath, A., Wilson, M., & Miller, K. (2016). Hydrodynamic versus GIS modelling for coastal flood vulnerability assessment: Which is better for guiding coastal management? *Ocean & Coastal Management*, *120*, 99–109. https://doi.org/10.1016/j.ocecoaman.2015.11.019

Tebaldi, C., Ranasinghe, R., Vousdoukas, M., Rasmussen, D. J., Vega-Westhoff, B., Kirezci, E., Kopp, R. E., Sriver, R., & Mentaschi, L. (2021). Extreme sea levels at different global warming levels. *Nature Climate Change*, *11*(9), 746–751. https://doi.org/10.1038/s41558-021-01127-1

Vousdoukas, M., Clarke, J., Ranasinghe, R., Reimann, L., Khalaf, N., Duong, T., Ouweneel, B., Sabour, S., Iles, C., Trisos, C., Feyen, L., & Simpson, N. (2021). *African Heritage Sites threatened by coastal flooding and erosion as sea-level rise accelerates*. https://doi.org/10.21203/rs.3.rs-758903/v1

Vousdoukas, M. I., Clarke, J., Ranasinghe, R., Reimann, L., Khalaf, N., Trang Minh Duong, Birgitt Ouweneel, Sabour, S., Iles, C., Trisos, C. H., Feyen, L., Mentaschi, L., & Simpson, N. P. (2022). African heritage sites threatened as sea-level rise accelerates. *Nature Climate Change*. https://doi.org/10.1038/s41558-022-01280-1

Vousdoukas, M. I., Mentaschi, L., Voukouvalas, E., Verlaan, M., Jevrejeva, S., Jackson, L. P., & Feyen, L. (2018). Global probabilistic projections of extreme sea levels show intensification of coastal flood hazard. *Nature Communications*, *9*(1), 2360. https://doi.org/10.1038/s41467-018-04692-w

Wahl, T., Haigh, I. D., Nicholls, R. J., Arns, A., Dangendorf, S., Hinkel, J., & Slangen, A. B. A. (2017). Understanding extreme sea levels for broad-scale coastal impact and adaptation analysis. *Nature Communications*, *8*(1), 16075. https://doi.org/10.1038/ncomms16075

Williams, L. L., & Lück-Vogel, M. (2020). Comparative assessment of the GIS based bathtub model and an enhanced bathtub model for coastal inundation. *Journal of Coastal Conservation*, *24*(2), 23. https://doi.org/10.1007/s11852-020-00735-x

Yin, J., Lin, N., & Yu, D. (2016). Coupled modeling of storm surge and coastal inundation: A case study in N ew Y ork C ity during H urricane S andy. *Water Resources Research*, *52*(11), 8685–8699. https://doi.org/10.1002/2016WR019102